

# Morpho-kinematic properties of Wolf-Rayet planetary nebulae

A. Danehkar <sup>1</sup>

<sup>1</sup> Department of Astronomy, University of Michigan, 1085 S. University Ave, Ann Arbor, MI 48109, USA

Received July 9, 2021

## Abstract

The majority of planetary nebulae (PNe) show axisymmetric morphologies, whose causes are not well understood. In this work, we present spatially resolved kinematic observations of 14 Galactic PNe surrounding Wolf-Rayet ([WR]) and weak emission-line stars (*wels*) based on the H $\alpha$  and [N II] emission taken with the Wide Field Spectrograph on the ANU 2.3-m telescope. Velocity-resolved channel maps and position–velocity diagrams, together with archival *Hubble Space Telescope* (*HST*) and ground-based images, are employed to construct three-dimensional morpho-kinematic models of 12 objects using the program SHAPE. Our results indicate that these 12 PNe have elliptical morphologies with either open or closed outer ends. Kinematic maps also illustrate on-sky orientations of elliptically symmetric morphologies of the interior shells in NGC 6578 and NGC 6629, and the compact ( $\leq 6$  arcsec) PNe Pe 1-1, M 3-15, M 1-25, Hen 2-142, and NGC 6567, in agreement with the high-resolution *HST* images containing morphological details. Point-symmetric knots in Hb 4 exhibit deceleration with distance from the nebular center that could be due to shock collisions with the ambient medium. Velocity dispersion maps of Pe 1-1 disclose point-symmetric knots similar to those in Hb 4. Collimated outflows are also visible in the position–velocity diagrams of M 3-30, M 1-32, M 3-15, and K 2-16, which are reconstructed by tenuous prolate ellipsoids extending upwardly from thick toroidal shells in our models.

*Unified Astronomy Thesaurus concepts:* Planetary nebulae (1249); Interstellar medium (847); Stellar jets (1607); Stellar kinematics (1608); Wolf-Rayet stars(1806)

*Supporting material:* figure sets

## 1. Introduction

Planetary nebulae (PNe) are bright hydrogen-rich envelopes expelled formerly by evolved stars with low-to-intermediate progenitor masses (1–8  $M_{\odot}$ ) in the asymptotic giant branch (AGB) phase. These envelopes are fully ionized by strong ultraviolet (UV) radiations from their hot degenerate nuclei in the post-AGB stage. Photoionization produces visible nebulae and also contributed to some thermal effects. Stellar winds from central stars of planetary nebulae (CSPNe) departing from the AGB phase introduce some hydrodynamic effects to these ionized envelopes that successively change their gaseous distributions. Line emission produced by the ionized envelope allows us to observe its morphological structure. Kinematic observations of PNe not only reveal their morphologies, but also give insights into the mass-loss processes in the AGB phase and during their transition from the AGB to PN, as well as PN evolution in the post-AGB phase (see e.g. Balick 1987; Corradi & Schwarz 1995; Balick & Frank 2002; Schönberner et al. 2005a,b, 2010; Kwok 2010).

Observations of PNe have mostly displayed elliptical and bipolar axisymmetric morphologies (see e.g. Balick 1987; Balick et al. 1987; Schwarz et al. 1992; Sahai et al. 2011; Weidmann et al. 2016), which have posed a major challenge to theories describing their formation (see review by Balick & Frank 2002). Single star evolution can produce

spherical nebular shells, but may also make elliptical shells due to the interaction with the interstellar medium (ISM). However, it has considerable difficulties in generating highly axisymmetric morphologies. The interacting stellar winds (ISW) theory (Kwok et al. 1978) implies that a slow ( $\sim 10 \text{ km s}^{-1}$ ), dense wind from the AGB phase that is pushed away by a fast ( $\sim 1000 \text{ km s}^{-1}$ ) tenuous stellar wind in the PN phase makes a compressed dense shell. The ISW model extended by Kahn & West (1985) known as the generalized interacting stellar winds (GISW) theory can also produce a highly axisymmetric gas distribution. Nevertheless, the GISW model cannot completely describe all types of observed elliptical and bipolar morphologies (Balick & Frank 2002). Moreover, the GISW model needs a density contrast to produce an aspherical morphology. Recently, many complex axisymmetric morphologies have been found by high-resolution imaging observations (Sahai et al. 2011) that cannot adequately be described by the GISW theory.

It has been suggested that axisymmetric morphologies are produced by some tidal interactions with a binary companion (Soker & Harpaz 1992; Soker & Livio 1994; Soker 2006; Nordhaus & Blackman 2006; Nordhaus et al. 2007). This binary companion could be a white dwarf or a planet that accretes material from an AGB star. Paczynski (1976) first proposed the role of binary companions in shaping PNe through a common-envelope (CE) phase. Moreover, a mixture of strong toroidal magnetic fields and rotating stellar winds from a single star has been suggested for an equatorial density enhancement and jet-like outflows (García-Segura 1997; García-Segura et al. 1999; García-Segura & López

2000; Frank & Blackman 2004). Nevertheless, Soker (2006) argued that the magnetic fields measured in PNe cannot have a central role in shaping PNe, and a single star cannot supply the energy and angular momentum for complex axisymmetric morphologies. Currently, there is a strong argument that most axisymmetric morphologies of PNe have been shaped through a binary channel (Miszalski et al. 2009a,b; De Marco 2009; Nordhaus et al. 2010). Recently, Miszalski et al. (2009b) found that nearly 30 percent, perhaps as high as 60 percent, of bipolar PNe contain post-CE binaries, suggesting the CE phase preferentially shapes axisymmetric PNe. Transformation of the orbital angular momentum of the binary system to the CE unbind it and shape a axisymmetric nebula, whose symmetric axis is perpendicular to the orbital plane of the binary system. Recently, high resolution kinematic analyses of some PNe around post-CE CSPN have been shown to have alignments between their nebular symmetric axes and binary orbital axes (see e.g. Mitchell et al. 2007; Jones et al. 2010, 2012; Tyndall et al. 2012; Huckvale et al. 2013).

The small-scale *low-ionization structures* (LISs) inside or outside the main shells have been identified in nearly 10% of Galactic PNe (Corradi et al. 1996; Gonçalves et al. 2001, 2009), which are more visible in low-excited emission such as [N II] and [S II] than in high-excited emission. Gonçalves et al. (2001) classified them as knots, jets and jetlike systems. *Knots*, either in pairs or isolated, are defined as those LISs with an aspect length-to-width ratio close to 1, while those with an aspect ratio much larger than 1 are classified as filaments. *Jets* are defined as highly collimated filaments that symmetrically appear as pairs on the both sides of the central star and move with velocities much larger than the expansion velocity of the main shell. Those filaments with no evidence of velocities higher than the expansion velocity of the main body are called *jetlike*. However, projection effects make it extremely difficult to distinguish easily between jets and jetlike systems. Highly collimated high-velocity jets or high-velocity pairs of knots constitute around half of LISs, which are named *fast, low-ionization emission regions* (FLIERS; Balick et al. 1993, 1994). FLIERS have radial velocities of 25–200 km s<sup>-1</sup> with respect to the main bodies (Balick et al. 1994). The formation of FLIERS, and their associated density and velocity contrast with the main shells are not yet well understood. It has been hypothesized that FLIERS are produced by axisymmetric superwind mass-loss through a CE channel, tidal interaction with a low-mass companion, and angular momentum deposition of the binary system (Soker 1990; Soker & Harpaz 1992).

Most CSPNe have hydrogen-rich stellar atmospheres, but a substantial fraction ( $\lesssim 25\%$ ) of them have been found to have *hydrogen-deficient* fast expanding atmospheres characterized by high mass-loss rates (Tylenda et al. 1993; Leuenhagen et al. 1996; Leuenhagen & Hamann 1998; Acker & Neiner 2003). Their surface abundances exhibit helium, carbon, oxygen and neon that are products of the helium-burning phase and a post-helium flash (Werner & Herwig 2006). Most of these CSPNe are classified as the carbon sequence of Wolf-Rayet ([WR]) stars, resembling those of massive Wolf-Rayet (WR) stars (van der Hucht et al. 1981; van der Hucht 2001), where the square bracket distinguishes them from massive counterparts. About half of them have stellar temperatures of 80–150 kK,

and are identified as the early-type ([WCE]), including the spectral classes [WO1]–[WC5] (Koesterke & Hamann 1997; Peña et al. 1998). Others having stellar temperatures between 20–80 kK are called the late-type ([WCL]), including [WC6–11] (Leuenhagen et al. 1996; Leuenhagen & Hamann 1998). A few CSPNe show narrower and weaker emission lines (C IV 5805 Å and C III 5695 Å), which are not identical to those [WR], so called weak emission-line stars (*wels*; Tylenda et al. 1993). These *wels* CSPNe are surprisingly higher towards the Galactic bulge and closer to the center of the Galaxy, and apparently originated from different stellar populations than [WR] stars (Górny et al. 2004, 2009).

This work is aimed at the morpho-kinematic properties of PNe surrounding [WR] and *wels* nuclei by means of optical integral field unit (IFU) spectroscopy. This paper is structured as follows. Section 2 describes our observational and data reduction. In Section 3, we present the IFU kinematic results. The morpho-kinematic modeling and their results are presented in Section 4, followed by our conclusion in Section 5.

## 2. Observations

IFU observations of the PNe studied in this work were collected with the Wide Field Spectrograph (WiFeS; Dopita et al. 2007, 2010) at the Siding Spring Observatory in April 2010 under program number 1100147 (PI: Q. A. Parker). WiFeS is an image-slicing IFU designed for the ANU 2.3-m telescope that feeds a double-beam spectrograph. It samples 0.5 arcsec along each of twenty five 38 arcsec  $\times$  1 arcsec slitlets, resulting in a field-of-view of 25  $\times$  38 arcsec<sup>2</sup> with a spatial resolution element of 1  $\times$  0.5 arcsec<sup>2</sup>. The spectroscopic output is projected onto a CCD detector of 4096  $\times$  4096 pixels. Each slitlet is mapped onto 2 pixels on the CCD detector that leads to a reconstructed point spread function (PSF) with a full width at half-maximum (FWHM) of  $\sim 2$  arcsec. The spectrograph uses volume phase holographic gratings to provide a spectral resolution of  $R \sim 7000$  or 3000, corresponding to a velocity resolution of either  $\sim 21$  or  $\sim 60$  km s<sup>-1</sup>, respectively.

Our targets were observed with the spectral resolution of  $R \sim 7000$  covering the wavelength range of 4415–7070 Å. As each spectrum is 4096 pixels long in the CCD detector, it provides a linear wavelength dispersion per pixel of 0.36 Å in the blue arm and 0.45 Å in the red arm of the  $R \sim 7000$  grating. The WiFeS spatial resolution with the reconstructed PSF FWHM of 2 arcsec enables us to identify morphologies of PNe with angular diameters larger than 6 arcsec. This spatial resolution is not ideal for resolving compact ( $\leq 6$  arcsec) PNe, but it can determine on-sky orientations of morphologies from their extended faint lobes or exterior halos (see Danehkar & Parker 2015). All targets were acquired in the classical data accumulation mode. Biases, flat-field frames, twilight sky flats, arc lamp exposures, wire frames, and standard stars were also collected for the bias reduction, flat-fielding, wavelength and spatial calibrations, and flux calibration.

Table 1 presents a journal of the WiFeS observations. The usual PN names, PNG numbers, coordinates (RA and Dec.), stellar types of the CSPN from Acker et al. (1992), as classified by Crowther et al. (1998) and Acker & Neiner (2003), are given in Columns 1–4, respectively. The effective temperature ( $T_{\text{eff}}$ ), stellar luminosity ( $L$ ), and stellar wind terminal velocity

**Table 1.** Journal of the planetary nebulae observed with the ANU 2.3-m Telescope, including their stellar characteristics.

Name	PNG	RA & Dec./J2000	CSPN (A92)	$T_{\text{eff}} - \log(L)$ (kK) – ( $L_{\odot}$ )	$V_{\infty}$ (km/s)	$\log \dot{M}^a$ ( $M_{\odot}/\text{yr}$ )	$M_{\star}^b$ ( $M_{\odot}$ )	Exp. (sec)	Obs. Date
PB 6	278.8+04.9	10 13 15.9 – 50 19 59.1	[WO 1]	103 – 3.57 (K91)	2496 (A03)	–7.15	0.60	1200	2010 Apr 20
M 3-30	017.9–04.8	18 41 14.9 – 15 33 43.6	[WO 1]	49 – 3.3 <sup>b</sup> (A03)	2059 (A03)	–7.50	0.56	1200	2010 Apr 21
Hb 4	003.1+02.9	17 41 52.7 – 24 42 08.0	[WO 3]	85 – 3.6 (A03,A02)	2059 (A03)	–7.11	0.60	300,1200	2010 Apr 21
IC 1297	358.3–21.6	19 17 23.5 – 39 36 46.4	[WO 3]	91 – 3.7 <sup>b</sup> (A03)	2933 (A03)	–6.98	0.62	60,1200	2010 Apr 21
Pe 1-1	285.4+01.5	10 38 27.6 – 56 47 06.5	[WO 4]	85 – 3.3 (A02)	2870 (A03)	–7.50	0.55	60,1200	2010 Apr 21
M 1-32	011.9+04.2	17 56 20.1 – 16 29 04.6	[WO 4] <sub>pec</sub>	56 <sup>c</sup> – 3.5 <sup>d</sup>	4867 (A03)	–7.24	0.60	1200	2010 Apr 20
M 3-15	006.8+04.1	17 45 31.7 – 20 58 01.6	[WC 4]	55 – 3.6 (A03,A02)	1872 (A03)	–7.11	0.59	60,1200	2010 Apr 20
M 1-25	004.9+04.9	17 38 30.3 – 22 08 38.8	[WC 5-6]	56 – 3.8 (A03,A02)	1747 (A03)	–6.85	0.62	60,1200	2010 Apr 20
Hen 2-142	327.1–02.2	15 59 57.6 – 55 55 32.9	[WC 9]	35 – 3.7 (A03,G07)	884 (A03)	–6.98	0.60	60,1200	2010 Apr 20
K 2-16	352.9+11.4	16 44 49.1 – 28 04 04.7	[WC 11]	19 – 3.3 (A03,A02)	260 (A03)	–7.50	0.52	1200	2010 Apr 20
NGC 6578	010.8–01.8	18 16 16.5 – 20 27 02.7	<i>wels</i> (T93)	63 – < 4.03 (S89)	1498 (T93)	< –6.55	< 0.68	60,1200	2010 Apr 22
NGC 6567	011.7–00.6	18 13 45.2 – 19 04 34.2	<i>wels</i> (T93)	47 – 3.62 (G97)	1747 (T93)	–7.08	0.60	60,1200	2010 Apr 22
NGC 6629	009.4–05.0	18 25 42.5 – 23 12 10.2	<i>wels</i> (T93)	35 – 3.53 (G97)	1747 (T93)	–7.20	0.56	60,1200	2010 Apr 22
Sa 3-107	358.0–04.6	17 59 55.0 – 32 59 11.8	<i>wels</i> (D11)	89 <sup>c</sup> – < 4.77 <sup>d</sup>	874 (D11)	< –5.60	< 0.85	1200	2010 Apr 22

<sup>a</sup> The mass-loss rates calculated using the formula given by Nugis & Lamers (2000).

<sup>b</sup> Evolutionary tracks of helium-burning model by Blöcker (1995).

<sup>c</sup> Calculated from the nebular excitation class using the correlation by Dopita & Meatheringham (1991).

<sup>d</sup> Stellar luminosity from the standard bolometric correction method.

**Note.** References are as follows: A92 – Acker et al. (1992); A02 – Acker et al. (2002); A03 – Acker & Neiner (2003); D11 – Depew et al. (2011); G97 – Górny et al. (1997); G07 – Gesicki & Zijlstra (2007); K91 – Kaler et al. (1991); S89 – Shaw & Kaler (1989); T93 – Tylenda et al. (1993).

( $V_{\infty}$ ), together with their references, are given in Columns 5–6, respectively. The mass-loss rates ( $\dot{M}$ ) in Column 7 were calculated using the formula given by Nugis & Lamers (2000), stellar luminosities, and typical [WR] chemical composition of  $Y = 0.43$  and  $Z = 0.56$ . Column 8 lists the stellar mass ( $M_{\star}$ ) determined from the helium-burning evolutionary models by Blöcker (1995). The exposure times used for the observations and the observing date are given in Columns 9 and 10, respectively.

Our sample includes 10 well-known PNe with [WR] central stars chosen from the literature (Crowther et al. 1998; Acker & Neiner 2003; Weidmann et al. 2008). These [WR] PNe with a wide range from early- to late-type allow us to identify morphologies in different evolutionary stages of PNe with various stellar classes of [WR] and *wels*. Previously, two PNe with [WC 10], whose morpho-kinematic structures were studied by Danehkar & Parker (2015), are very compact, since they are too young in comparison to [WCE] PNe. The CSPN M 1-32 was classified by Acker & Neiner (2003) as the *peculiar* [WO 4] based on the wide FWHM of C IV-5801/12 doublet corresponding to a terminal velocity of  $V_{\infty} \simeq 4900 \text{ km s}^{-1}$  that is higher than  $V_{\infty} \simeq 2000\text{--}3000 \text{ km s}^{-1}$  typically seen in usual [WR] CSPNe. The PN Th 2-A whose morpho-kinematic structure was studied by Danehkar (2015) is another object with [WO 3]<sub>pec</sub> classified by Weidmann et al. (2008). Our sample also contains 4 well-known PNe with *wels* selected from the literature (Tylenda et al. 1991, 1993; Górny et al. 1997, 2004). M 2-42 is another PN with *wels*, whose morpho-kinematic model was reconstructed based on IFU observations (Danehkar et al. 2016). Stellar

luminosities listed in Table 1 are mostly from the literature. For M 3-30 and IC 1297, we derived the stellar luminosity from the evolutionary tracks for helium-burning models by Blöcker (1995) and the relation between terminal velocity ( $V_{\infty}$ ), effective temperature ( $T_{\text{eff}}$ ) and stellar mass ( $M_{\star}$ ) given by Pauldrach et al. (1988). We also estimated the stellar luminosities according to the standard bolometric correction method for M 1-32 using  $V = 17 \text{ mag}$  (Peña et al. 2001),  $D = 4796 \text{ pc}$  (Stanghellini & Haywood 2010) and  $c(\text{H}\beta) = 1.35$  (Danehkar 2021); and Sa 3-107 using  $D = 6 \text{ kpc}$ ,  $V = 16.4 \text{ mag}$  (Lasker et al. 2008), and  $c(\text{H}\beta) = 1.62$  (Danehkar 2021).

Data reduction was performed using the IRAF pipeline *wifes*.<sup>1</sup> We performed the flat-fielding using the frames taken with exposures of a quartz iodine lamp. A medium-average combined bias was subtracted from the calibration frames. We performed the wavelength calibration using Cu–Ar arc exposures taken at the beginning of the night. The spatial calibration was done by using wire frames obtained by diffuse illumination of the coronagraphic aperture with a QI lamp. Cosmic rays and bad pixels were removed from the rawdata before the sky subtraction. We employed the IRAF task *lacos\_im* (LA-Cosmic package; van Dokkum 2001) to remove cosmic rays from the rawdata, while bad pixels and any remaining cosmic rays were manually removed with the IRAF/STSDAS task *imedit* before the sky subtraction. We chose a suitable sky window from the

<sup>1</sup> IRAF is distributed by NOAO, which is operated by AURA, Inc., under contract to the National Science Foundation.

**Table 2.** Systemic velocities in the LSR frame and mean expansion (HWHM) velocities measured from the volume-integrated line profiles.

Name	$v_{\text{sys}}(\text{H}\alpha)$	$v_{\text{sys}}(\text{km/s})$	$V_{\text{HWHM}}(\text{km/s})$				$v_{\text{exp}}$ (km/s)
	(km/s)	(D98)	H $\alpha$	[N II]	[S II]	Mean	
PB 6	52.1	$45.9 \pm 1.3$	35.5	32.5	30.6	$32.9 \pm 2.4$	$38 \pm 4$ (G09)
M 3-30	79.2	$67.3 \pm 14.0$	31.6	41.9	35.0	$36.2 \pm 5.1$	$37.31 \pm 5$ (M06)
Hb 4 (shell)	-45.9	$-48.5 \pm 1.5$	23.2	24.0	22.4	$23.2 \pm 0.8$	21.5 (L97)
IC 1297	12.6	$16.6 \pm 1.5$	31.8	31.7	30.1	$31.2 \pm 0.8$	$32.7 \pm 1.7$ (A76)
Pe 1-1	7.1	$8.0 \pm 0.5$	21.7	24.3	24.3	$23.4 \pm 1.3$	24 (G96)
M 1-32	-73.8	$-76.8 \pm 7.6$	33.7	32.0	27.9	$31.2 \pm 2.9$	14: (P01)
M 3-15	111.3	$109.7 \pm 0.7$	23.7	22.3	17.8	$21.2 \pm 3.0$	18.2 (R09)
M 1-25	25.8	$26.3 \pm 2.0$	27.4	28.3	24.2	$26.6 \pm 2.0$	23 (M06)
Hen 2-142	-92.5	$-94.5 \pm 0.3$	22.1	21.6	17.5	$20.4 \pm 2.3$	20(A02,G07)
K 2-16	23.4	$14.9 \pm 12.0$	31.0	34.1	28.5	$31.2 \pm 2.8$	34 (A02)
NGC 6578	19.3	$17.1 \pm 1.8$	18.7	23.5	23.6	$21.9 \pm 3.0$	$17.2 \pm 1.4$ (M06)
NGC 6567	136.7	$132.4 \pm 0.7$	24.2	38.9	37.5	$33.5 \pm 8.0$	19 (W89)
NGC 6629	25.0	$26.5 \pm 1.3$	16.5	20.8	23.7	$20.3 \pm 3.6$	$16.3 \pm 2.5$ (M06)
Sa 3-107	-132.9	-	17.0	16.9	14.5	$16.1 \pm 1.6$	-

**Note.** References are as follows: A76 – Acker (1976); A02 – Acker et al. (2002); D98 – Durand et al. (1998); G96 – Gesicki & Acker (1996); G07 – Gesicki & Zijlstra (2007); G09 – García-Rojas et al. (2009); L97 – López et al. (1997); M06 – Medina et al. (2006); P01 – Peña et al. (2001); R09 – Richer et al. (2009); W89 – Weinberger (1989).

science data for the sky subtraction purpose. We calibrated the science data to absolute flux units using observations of the spectrophotometric standard star EG 274 and LTT 3864. The flux-calibrated data were corrected for the atmospheric extinction. A linear interpolation technique was employed to minimize sampling noise made by the image-slicing IFU sampling technique.

The high-resolution *Hubble Space Telescope* (*HST*) images of the PNe were obtained from the Mikulski Archive for Space Telescopes, and the 3.5-m ESO New Technology Telescope (NTT) images from Schwarz et al. (1992), presented in Appendix A, which were used to constrain our morpho-kinematic models. The IRAF task `lacos.im` was employed to remove cosmic rays from the *HST* images.

### 3. Results

#### 3.1. Mean Expansion and Systemic Velocities

Table 2 lists the kinematic features measured from volume-integrated emission line profiles in the spectroscopic observations of our sample. Column 2 presents the systemic velocity ( $v_{\text{sys}}$ ) in the frame of the local standard of rest (LSR) based on the H $\alpha$  emission that approximately representing the systemic velocity of the whole nebula, along with the previously value from Durand et al. (1998) in Column 3. We transferred the radial velocity to the LSR frame using the IRAF/ASTUTIL task `rvcorrect`. The mean expansion velocities ( $v_{\text{HWHM}}$ ) associated with the half width at half maximum (HWHM) of H $\alpha$   $\lambda$ 6563, [N II]  $\lambda$ 6548,6584 and [S II]  $\lambda$ 6716,6731, and their average velocity are presented in columns 4–7, respectively. The HWHM expansion velocities,  $V_{\text{HWHM}} = \sqrt{8 \ln(2)} \sigma_{\text{true}}/2$ , were corrected for the instrumental width and the thermal broadening as follows:  $\sigma_{\text{true}} = \sqrt{\sigma_{\text{obs}}^2 - \sigma_{\text{ins}}^2 - \sigma_{\text{th}}^2 - \sigma_{\text{fs}}^2}$ , where the instrumental width  $\sigma_{\text{ins}}$  is measured from the [O I]  $\lambda$ 5577 and  $\lambda$ 6300 night

sky lines having a typical value of  $\approx 18 \text{ km s}^{-1}$  for the WiFeS ( $R \sim 7000$ ), the thermal broadening  $\sigma_{\text{th}}$  is estimated from the Boltzmann’s equation  $\sigma_{\text{th}} = \sqrt{8.3 T_e [\text{kK}]/Z} [\text{km s}^{-1}]$  ( $Z$  is the atomic weight of the atom or ion), and the fine structure broadening  $\sigma_{\text{fs}}$  is typically  $\approx 3 \text{ km s}^{-1}$  for H $\alpha$  (Clegg et al. 1999). For comparison, Column 8 lists the expansion velocity, together with its reference, from the literature.

The radiation-hydrodynamics models by Schönberner et al. (2010) demonstrated that the HWHM velocities of volume-integrated line profiles always underestimate the true expansion velocity, so the HWHM method is suitable for slowly expanding objects, but cannot provide true expansion velocities of large extended PNe. For the Magellanic Cloud PNe, Dopita et al. (1985, 1988) assumed that  $v_{\text{exp}} = 1.82 V_{\text{HWHM}}$ , nearly twice the more widespread use of the HWHM velocity. This is associated with the maximum gas velocity behind the outer shock, and it may not be related to the mean expansion velocity of the nebular shell. Here, we assume  $v_{\text{exp}} = V_{\text{HWHM}}$  that may correspond to the mean expansion of a spherical gaseous shell. However, velocity-resolved channel maps in Section 4 imply that the HWHM velocities of volume-integrated line profiles do not correctly describe the mean expansion velocity of the nebular shell due to aspherical morphologies and collimated bipolar outflows extending upwardly from dense shells.

#### 3.2. Spatially-resolved Kinematic Maps

Figure 1 presents spatially resolved maps of the flux intensity, continuum, radial velocity, and velocity dispersion of the H $\alpha$  and [N II] line emission derived from the WiFeS observations of all the objects in our sample. This information are obtained by fitting Gaussian functions to spaxels of the IFU datacube using the IDL library MPFIT (Markwardt 2009) developed for the nonlinear least-squares minimization fitting.

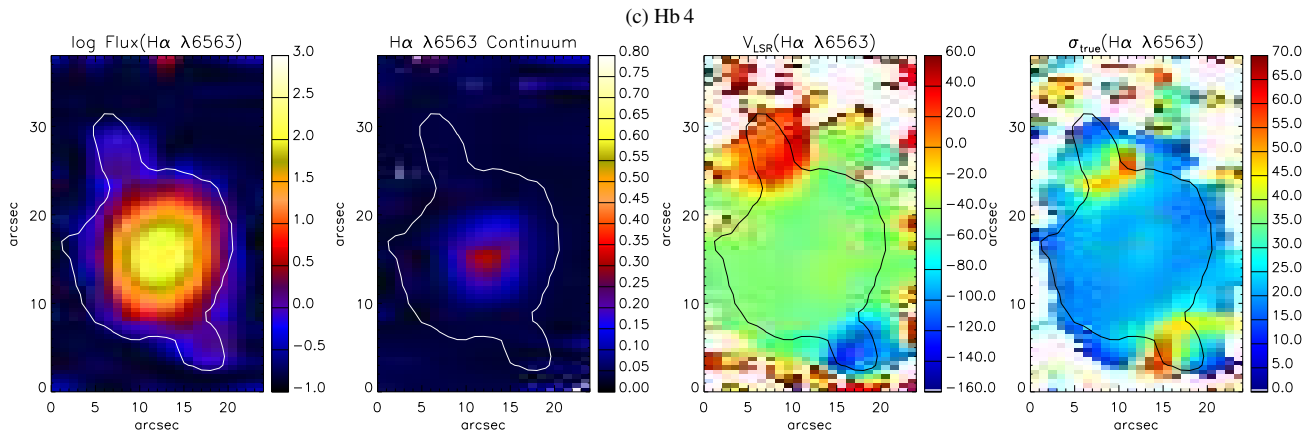


**Figure 1.** From left to right, the spatial distribution maps of logarithmic flux intensity, continuum, LSR velocity, and velocity dispersion of the H $\alpha$   $\lambda$ 6563 and [N II]  $\lambda$ 6584 emission lines for: (a) PB 6, (b) M 3-30, (c) Hb 4, (d) IC 1297, (e) Pe 1-1, (f) M 1-32, (g) M 3-15, (h) M 1-25, (i) Hen 2-142, (j) K 2-16, (k) NGC 6578, (l) NGC 6567, (m) NGC 6629, and (n) Sa 3-107. Fluxes are in logarithm of  $10^{-15}$   $\text{erg s}^{-1} \text{cm}^{-2} \text{spaxel}^{-1}$  unit, continua in  $10^{-15}$   $\text{erg s}^{-1} \text{cm}^{-2} \text{\AA}^{-1} \text{spaxel}^{-1}$ , and LSR velocities and velocity dispersion in  $\text{km s}^{-1}$ . The white/black contour in each panel shows the narrow-band H $\alpha$  emission in arbitrary unit retrieved from the SHS. North is up and east is toward the left-hand side. The complete figure set (28 images) is available in the online journal.

**Fig. Set 1.** From left to right, the spatial distribution maps of logarithmic flux intensity, continuum, LSR velocity, and velocity dispersion of the H $\alpha$   $\lambda$ 6563 (top panels) and [N II]  $\lambda$ 6584 (bottom panels) emission lines for: (a) PB 6, (b) M 3-30, (c) Hb 4, (d) IC 1297, (e) Pe 1-1, (f) M 1-32, (g) M 3-15, (h) M 1-25, (i) Hen 2-142, (j) K 2-16, (k) NGC 6578, (l) NGC 6567, (m) NGC 6629, and (n) Sa 3-107. Fluxes are in logarithm of  $10^{-15}$   $\text{erg s}^{-1} \text{cm}^{-2} \text{spaxel}^{-1}$  unit, continua in  $10^{-15}$   $\text{erg s}^{-1} \text{cm}^{-2} \text{\AA}^{-1} \text{spaxel}^{-1}$ , and LSR velocities and velocity dispersion in  $\text{km s}^{-1}$ . The white/black contour in each panel shows the narrow-band H $\alpha$  emission in arbitrary unit retrieved from the SHS. North is up and east is toward the left-hand side.

The emission line profile is resolved if its emission line width is wider than the instrumental width ( $\sigma_{\text{ins}}$ , see § 3.1). Contour lines in each figure depict the distribution of the H $\alpha$  emission from the SuperCOSMOS H $\alpha$  Sky Survey (SHS; Parker et al. 2005) that may help us identify the nebular H $\alpha$  borders.

Figure 2 shows velocity-resolved channel maps of the H $\alpha$  and [N II] flux intensity on a logarithmic scale observed in a sequence of 12 or 18 velocity channels with a velocity resolution of  $\sim 21 \text{ km s}^{-1}$  relative to the LSR systemic velocity. The stellar continuum map derived for each line profile is subtracted from the associated flux intensity maps. Figure 3 also presents position–velocity (P–V) diagram arrays of the H $\alpha$  and [N II] line emission of each object extracted from the IFU datacube for two slits passing through the central star that are oriented with the position angles (PA) along and vertical to the symmetric axis of the best-fitting morpho-kinematic model (as determined § 4). The velocity axes on the P–V arrays is relative to the systemic velocity in the LSR frame. The stellar continuum of each line profile was also subtracted from the associated P–V diagrams. The velocity channel maps along with the P–V diagrams are employed to constrain our morpho-kinematic models in § 4.

Our IFU velocity maps of PB 6 taken with a long exposure time (1200 sec) reveal that two groups of ionized gas are moving in opposite directions on the both sides of the central star. Its *HST* image (see Figure 8) depicts a complex morphology with many multi-scale filamentary structures and several knots, which are analogous to the morphology of NGC 5189, similarly around a [WO I] star (Crowther et al. 1998). This object could contain low-ionization envelopes similar to those identified in NGC 5189 (Danekhar et al. 2018). However, the short exposure time (22 sec) and the

MIRVIS long-pass filter (4950–9450  $\text{\AA}$ ) of the *HST* image were inadequate for a detailed morphological analysis of PB 6.

The kinematics maps of M 3-30 likely suggest a pair of bipolar inner knots embedded in the elliptical shell. Previously, Stanghellini et al. (1993) also classified this object as a elliptical morphology with inner knots. However, our morpho-kinematic model (see § 4) constrained by the velocity channel maps and P–V diagrams indicate that they are associated with the outer ends of tenuous collimated bipolar outflows extending from the dense toroidal shell. Its toroidal morphology is also visible in the narrow-band H $\alpha$ + [N II] image taken with the 3.5 m ESO NTT (see Figure 8).

The IFU velocity maps of HB 4 illustrate a pair of point-symmetric knots or collimated jets detached from the main shell having a torus morphology based on the *HST* imaging observations (see Figure 8). These point-symmetric structures have extremely low brightness, but with high velocity dispersion. Taking the inclination angle of  $i = 40^\circ$  found by the kinematic model (in § 4), the maximum values of the point-symmetric knots reach  $170 \pm 10 \text{ km s}^{-1}$  with respect to the central star, which agrees with the long-slit kinematic analysis (López et al. 1997). These point-symmetric structures were previously identified in the H $\alpha$ + [N II]/[O III] image (Corradi et al. 1996).

The IFU observations of IC 1297 likely imply an elliptical morphology, which is also supported by the H $\alpha$ + [N II] image (Schwarz et al. 1992). However, Zuckerman & Aller (1986) described it as a broken ring, and Stanghellini et al. (1993) classified it under the irregular nebulae. Moreover, Corradi et al. (1996) suggested the presence of 1 isolated knot, which was later rejected by Gonçalves et al. (2001), and turned out to be a field star.

(c) Hb 4

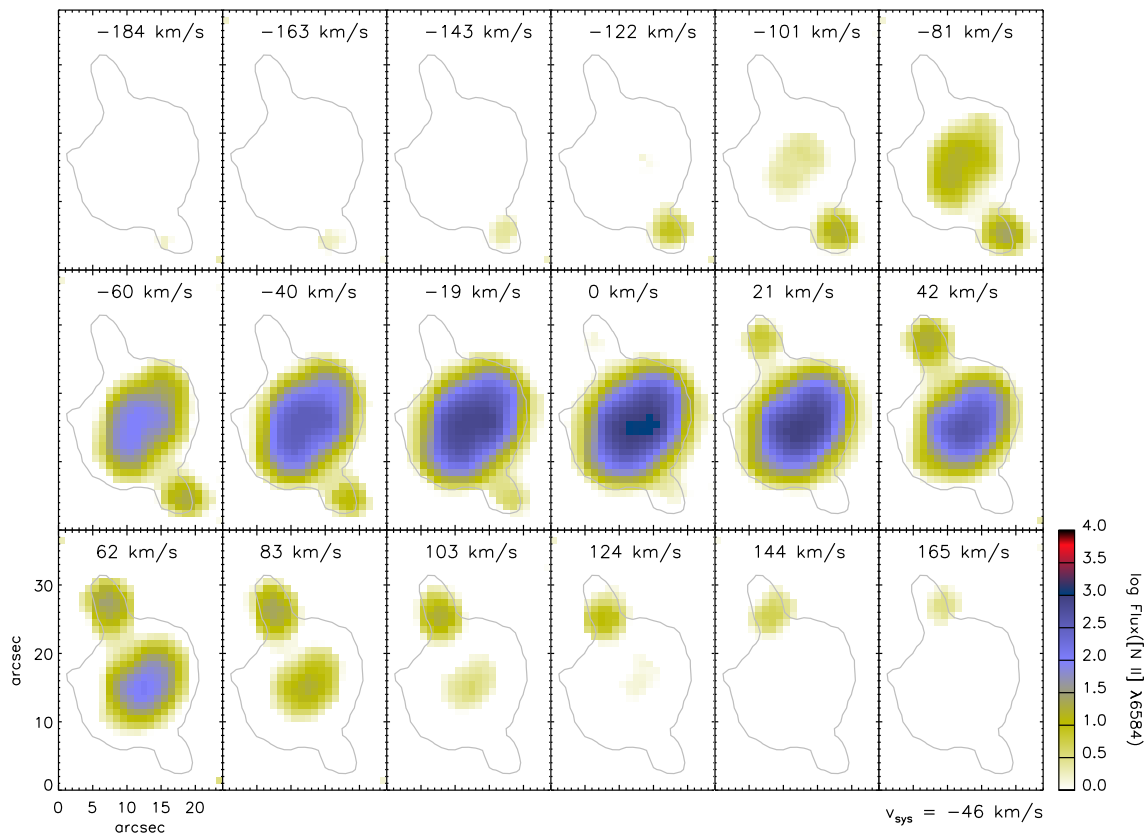


**Figure 2.** Velocity slices along the  $H\alpha$   $\lambda 6563$  and  $[N II]$   $\lambda 6584$  emission-line profiles for: (a) PB 6, (b) M 3-30, (c) Hb 4, (d) IC 1297, (e) Pe 1-1, (f) M 1-32, (g) M 3-15, (h) M 1-25, (i) Hen 2-142, (j) K 2-16, (k) NGC 6578, (l) NGC 6567, (m) NGC 6629, and (n) Sa 3-107. Each slice has a  $\sim 21 \text{ km s}^{-1}$  width, whose central velocity is given in  $\text{km s}^{-1}$  unit at the top of the panel. The LSR systemic velocity ( $v_{\text{sys}}$ ) of each object is given in  $\text{km s}^{-1}$  unit in the right bottom corner. The flux color is in logarithm of  $10^{-15} \text{ erg s}^{-1} \text{ cm}^{-2} \text{ spaxel}^{-1}$  unit. The contour in each panel shows the narrow-band  $H\alpha$  emission in arbitrary unit retrieved from the SHS. North is up and east is toward the left-hand side. The complete figure set (28 images) is available in the online journal.

**Fig. Set 2.** Velocity slices along the  $H\alpha$   $\lambda 6563$  and  $[N II]$   $\lambda 6584$  emission-line profiles for: (a) PB 6, (b) M 3-30, (c) Hb 4, (d) IC 1297, (e) Pe 1-1, (f) M 1-32, (g) M 3-15, (h) M 1-25, (i) Hen 2-142, (j) K 2-16, (k) NGC 6578, (l) NGC 6567, (m) NGC 6629, and (n) Sa 3-107. Each slice has a  $\sim 21 \text{ km s}^{-1}$  width, whose central velocity is given in  $\text{km s}^{-1}$  unit at the top of the panel. The LSR systemic velocity ( $v_{\text{sys}}$ ) of each object is given in  $\text{km s}^{-1}$  unit in the right bottom corner. The flux color is in logarithm of  $10^{-15} \text{ erg s}^{-1} \text{ cm}^{-2} \text{ spaxel}^{-1}$  unit. The contour in each panel shows the narrow-band  $H\alpha$  emission in arbitrary unit retrieved from the SHS. North is up and east is toward the left-hand side.

The velocity dispersion maps of Pe 1-1 depict two regions with high values of  $\sigma_{\text{true}} = 35 \pm 10 \text{ km s}^{-1}$  on both sides, which are analogous to those in HB 4. Its *HST* image in Figure 8 shows a barrel morphology having two collimated outflows in the regions with high velocity dispersion in the IFU maps. The on-sky orientation of the bipolar outflows determined from the IFU velocity maps is fully consistent with those in the high-resolution *HST* image.

It can be seen that the IFU velocity and dispersion maps of M 1-32 are akin to what found for Th 2-A being viewed almost pole-on (Danehkar 2015). Similarly, the P-V diagrams (see Figure 3) imply that this object has also collimated bipolar outflows with very low inclination ( $i = 5^\circ$ ; in § 4) relative to the line of sight. Previously, Peña et al. (2001) detected line profile wings extending upto  $\pm 100 \text{ km s}^{-1}$  that implies a high-velocity bipolar or multipolar ejection. The narrow-band  $H\alpha + [N II]$  image (see Figure 8) also shows a compact torus morphology.

The spatial resolution of the WiFeS observations is inadequate to display morphological features of the compact ( $\leq 6 \text{ arcsec}$ ) PNe M 3-15, M 1-25, Hen 2-142, and NGC 6567, and the interior shells in NGC 6578 and NGC 6629. From the *HST* observations in Figure 8, we can see elliptical morphologies for M 1-25, Hen 2-142, NGC 6578, NGC 6567, and NGC 6629, and a ring-like morphology for M 3-15. The orientations of their axisymmetric morphologies on the sky plane determined from spatially resolved kinematic observations are in full agreement with those spatial distributions with detailed morphological features seen in the high-angular resolution *HST* images in Figure 8. The *HST* images of NGC 6578 and NGC 6629 also indicate that their compact elliptical shells are surrounded by thin exterior halos.

The velocity IFU maps of K 2-16 also imply an elliptical nebula with tenuous collimated outflows. The narrow  $H\alpha + [N II]$  image of K 2-16 (Schwarz et al. 1992) shows a faint, circular nebula with a diameter of  $23''$ . Previously, Kohoutek (1977) suggested that it could be a large and old PN.

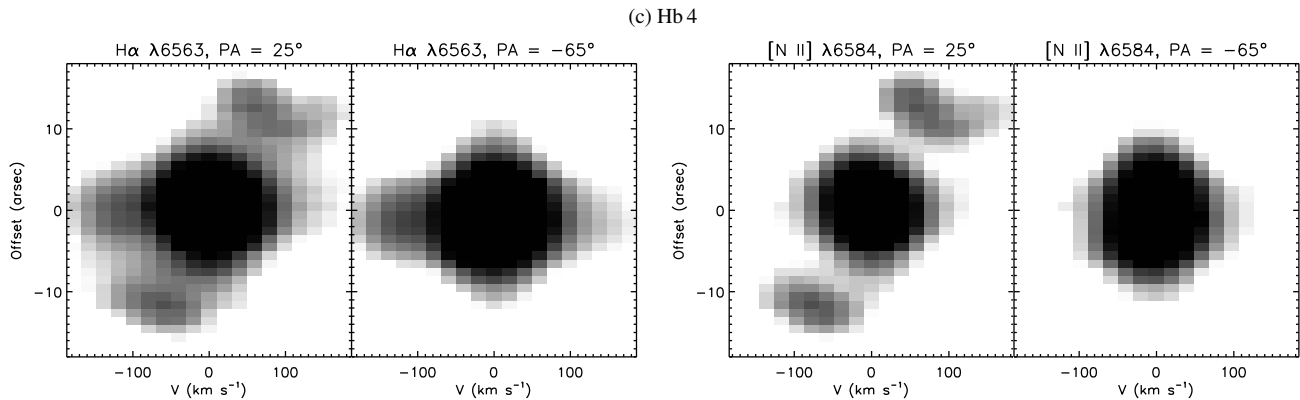


**Figure 3.** P–V arrays in the  $\text{H}\alpha$   $\lambda 6563$  and  $[\text{N II}]$   $\lambda 6584$  emissions for: (a) PB 6, (b) M 3-30, (c) Hb 4, (d) IC 1297, (e) Pe 1-1, (f) M 1-32, (g) M 3-15, (h) M 1-25, (i) Hen 2-142, (j) K 2-16, (k) NGC 6578, (l) NGC 6567, (m) NGC 6629, and (n) Sa 3-107. Slits oriented with the position angles (PA) along and vertical to the symmetric axis through the central star, respectively. The velocity is with respect to the systemic velocity of the object, given in  $\text{km s}^{-1}$  unit. The angular offset at 0 arcsec is the nebular center. The complete figure set (14 images) is available in the online journal.

**Fig. Set 3.** P–V arrays in the  $\text{H}\alpha$   $\lambda 6563$  and  $[\text{N II}]$   $\lambda 6584$  emissions for: (a) PB 6, (b) M 3-30, (c) Hb 4, (d) IC 1297, (e) Pe 1-1, (f) M 1-32, (g) M 3-15, (h) M 1-25, (i) Hen 2-142, (j) K 2-16, (k) NGC 6578, (l) NGC 6567, (m) NGC 6629, and (n) Sa 3-107. Slits oriented with the position angles (PA) along and vertical to the symmetric axis through the central star, respectively. The velocity is with respect to the systemic velocity of the object, given in  $\text{km s}^{-1}$  unit. The angular offset at 0 arcsec is the nebular center.

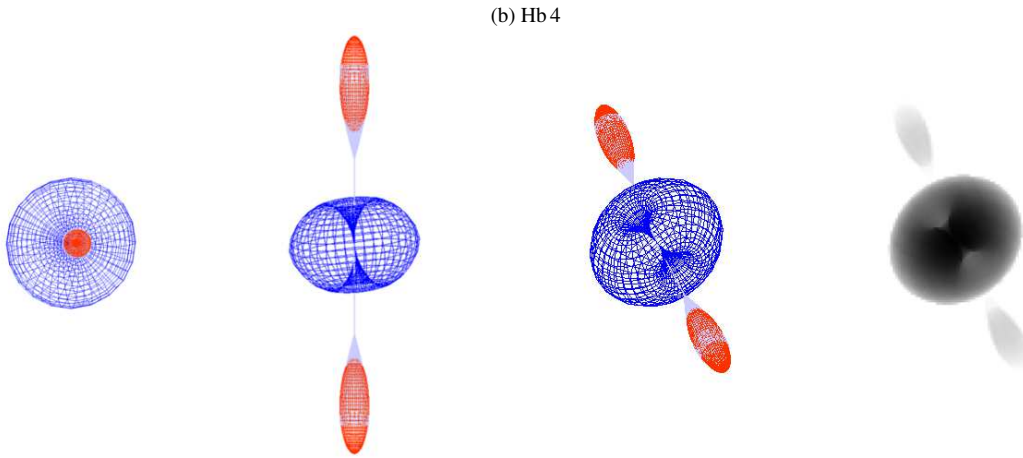
The velocity maps of Sa 3-107 likely suggest an axisymmetric morphology, though the detailed structures of this compact object cannot be resolved by the WiFeS. Previously, WiFeS observations of the compact PN PB 8 around a [WN/WC]-hybrid star hinted at an aspherical morphology but without any precise details (Danehkar 2018). It was shown that tenuous lobes extending from a compact nebula spatially resolved through IFU spectroscopy help us determine the on-sky orientation of its axisymmetric morphology (see Danehkar & Parker 2015). Thus, our WiFeS observations of Sa 3-107 could expose the orientation of its elliptical or bipolar morphology on the sky plane.

#### 4. Morpho-kinematic modeling

To construct three-dimensional morphological models based on velocity-resolved channel maps and P–V diagrams, we have used the interactive kinematic modeling program SHAPE v5.0 (Steffen & López 2006; Steffen et al. 2011) that applies molded polygon meshes to 3-D geometrical models of gaseous nebulae. It constructs a morphological model on a grid of volumetric cells and employs a ray-casting process to transfer radiation fields to these cells. The program produces several outputs that can directly be compared with kinematic observations, namely P–V diagram and velocity channel maps. P–V diagrams have been used for long-slit observations of many PNe (e.g. García-Díaz et al. 2009; Jones et al. 2010; López et al. 2012; Clark et al. 2013), whereas velocity channel maps have recently been employed to interpret kinematic IFU maps of some objects (Danehkar 2015; Danehkar et al. 2016). It also produces 2-D rendered images of ionized nebulae that can be matched with high-resolution images. This program has been used to build 3-D morpho-kinematic models of many PNe, for example NGC 6337 (García-Díaz et al. 2009), Abell 41 (Jones et al. 2010), Hb 5 (López et al. 2012), HaTr 4 (Tyndall et al. 2012), NGC 7026 (Clark et al. 2013), Abell 65 (Huckvale et al. 2013), Th 2-A (Danehkar 2015), M2-42 (Danehkar et al. 2016), and Abell 14 (Akraş et al. 2016).

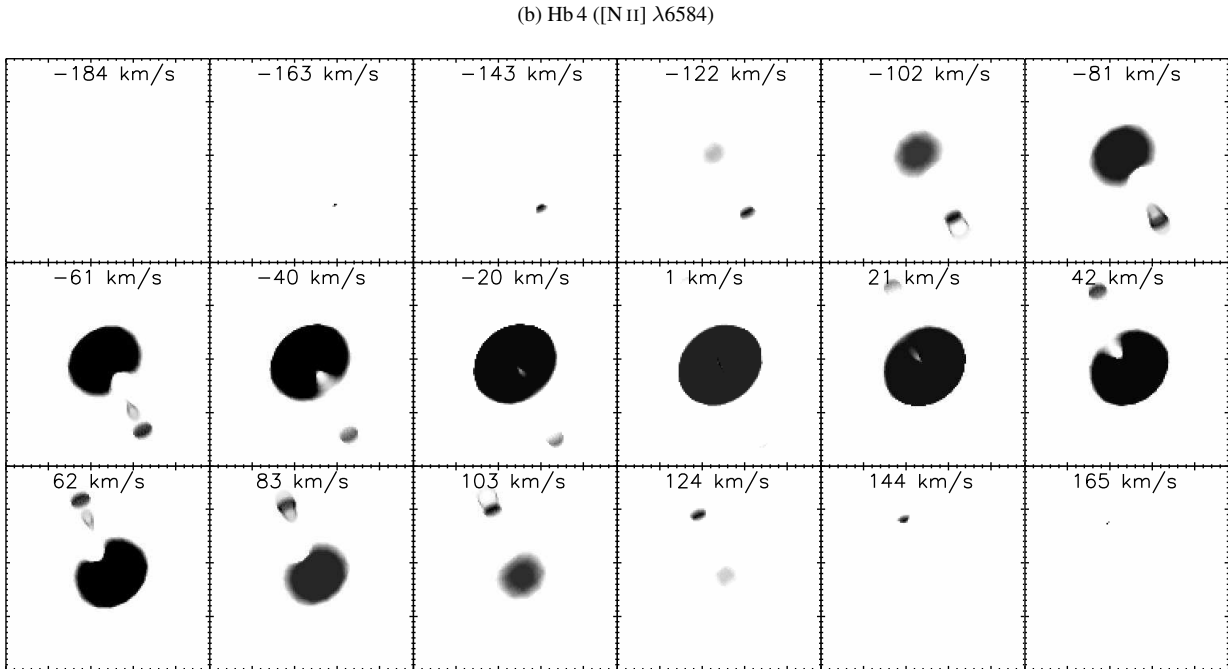
For this work, the velocity field is defined by a homologous flow (Steffen et al. 2009) that increases linearly with distance from the nebular center. However, to reproduce point-symmetric knots in the P–V diagrams of Hb 4, a decelerating velocity linearly decreasing with distance from the nebular center is used. To model each object, we carefully choose a 3-D geometry model and adjust various geometric parameters, along with inclination and origination angles, in order to reproduce those kinematic features seen in the P–V diagram and velocity channel maps of each object, while 2-D rendered images are expected to resemble the associated archival image. The inclination ( $i$ ) relative to the line of sight, the position angle (PA) of the on-sky orientation, and geometric parameters are modified in an iterative process until the model velocity maps and P–V diagram closely resemble the kinematic observations. We were able to construct 3-D morpho-kinematic models of the 12 PNe. For the compact PN Sa 3-107, we do not have any available high-resolution images. The *HST*/MIRVIS image of PB 6 taken with a short exposure of 22 sec and long-pass band (4950–9450 Å) is not suitable for morpho-kinematic modeling, but it suggests a complex morphology with multi-scale features similar to NGC 5189 (Danehkar et al. 2018). Figure 4 shows the final SHAPE mesh models of the 12 objects viewed from two different inclination angles ( $i = 0^\circ$  and  $90^\circ$ ), together with the best-fitting inclination ( $i$ ) and orientation (PA; see Table 3) before rendering, and the rendered result, respectively.

Figure 5 presents the synthetic velocity-resolved channel maps created by the best-fitting kinematic models aimed at reproducing the velocity channel maps of the  $\text{H}\alpha$  or  $[\text{N II}]$  emission (see Figure 2). The synthetic P–V diagrams made by the best-fitting models are also shown in Figure 6 that intend matching the P–V arrays of either  $\text{H}\alpha$  or  $[\text{N II}]$  emission (see Figure 3) extracted from the IFU datacube for two slits oriented with the PA along and vertical to the symmetric axis through the center of each object.



**Figure 4.** SHAPE mesh models for: (a) M 3-30, (b) Hb 4, (c) IC 1297, (d) Pe 1-1, (e) M 1-32, (f) M 3-15, (g) M 1-25, (h) Hen 2-142, (i) K 2-16, (j) NGC 6578, (k) NGC 6567, and (l) NGC 6629, before rendering at two different inclination angles ( $i = 0^\circ$  and  $90^\circ$ ), the best-fitting inclination and orientation, and the rendered image, respectively. The best-fitting parameters are listed in Table 3. The complete figure set (12 images) is available in the online journal.

**Fig. Set 4.** SHAPE mesh model for: (a) M 3-30, (b) Hb 4, (c) IC 1297, (d) Pe 1-1, (e) M 1-32, (f) M 3-15, (g) M 1-25, (h) Hen 2-142, (i) K 2-16, (j) NGC 6578, (k) NGC 6567, and (l) NGC 6629 before rendering at two different inclination angles ( $i = 0^\circ$  and  $90^\circ$ ), the best-fitting inclination and orientation, and the rendered image, respectively. The best-fitting parameters are listed in Table 3.



**Figure 5.** Synthetic velocity-resolved channel maps for: (a) M 3-30, (b) Hb 4, (c) IC 1297, (d) Pe 1-1, (e) M 1-32, (f) M 3-15, (g) M 1-25, (h) Hen 2-142, (i) K 2-16, (j) NGC 6578, (k) NGC 6567, and (l) NGC 6629, produced by the best-fitting morpho-kinematic models for velocity slices along the  $H\alpha$   $\lambda 6563$  or [N II]  $\lambda 6584$  emission (listed in round brackets following the PN name), with the parameters given in Table 3. The complete figure set (12 images) is available in the online journal.

**Fig. Set 5.** Synthetic velocity-resolved channel maps for: (a) M 3-30, (b) Hb 4, (c) IC 1297, (d) Pe 1-1, (e) M 1-32, (f) M 3-15, (g) M 1-25, (h) Hen 2-142, (i) K 2-16, (j) NGC 6578, (k) NGC 6567, and (l) NGC 6629, produced by the best-fitting morpho-kinematic models for velocity slices along the  $H\alpha$   $\lambda 6563$  or [N II]  $\lambda 6584$  emission (listed in round brackets following the PN name), with the parameters given in Table 3.

Table 3 lists the key parameters of the best-fitting morpho-kinematic models. Columns 4–6 present the position angle (PA) of the nebular symmetric axis projected onto the sky plane measured from the north toward the east in the equatorial coordinate system, the Galactic position angle (GPA) measured from the North Galactic Pole toward the Galactic east, and the inclination ( $i$ ) of the symmetric axis of the kinematic model with respect to the line of sight, respectively. Columns 7 and 8 give the mean expansion velocity of the main shell ( $v_{\text{exp}}$ ) adopted according to the integrated flux HWHM measurements, and the outflow velocity of collimated outflows with respect to the systemic velocity ( $v_{\text{out}}$ ) estimated from either P–V diagrams or velocity-resolved channel maps. The SHAPE morpho-kinematic models of the 12 PNe before rendering together with the rendered results are summarized in Figure 7 at their best-fitting inclinations and orientations.

The primary and secondary morphological features determined from our morpho-kinematic models are also summarized in Columns 9 and 10 in Table 3, respectively. The classification codes are according to Sahai et al. (2011) that include four primary classes: bipolar ( $B$ ), elliptical ( $E$ ), multipolar ( $M$ ), and irregular ( $I$ ). The  $B$  class is defined as objects with two primary, diametrically opposed lobes, centered on its expected location. The  $E$  class represents objects that are elliptical along a specific axis. The  $M$  class defines objects showing more than one primary lobe pairs whose axes are not aligned such as NGC 5189 (see Danehkar et al. 2018). The  $I$  class is defined by objects do not display any geometrical symmetry. The structure may be open or closed at their outer ends, denoted by ‘ $o$ ’ or ‘ $c$ ’, respectively. The secondary descriptors describe other morphological features: the point symmetry denoted by  $ps$ , two or more pairs of diametrically opposed lobes by  $ps(m)$ , diametrically opposed ansae by  $ps(an)$ , overall shape of the lobes by  $ps(s)$ , rings projected on lobes denoted by  $rg$ , and the central region with a toroidal structure by ‘ $r$ ’.

The SHAPE model of M 3-30 was constructed using a thick toroidal shell together with a thin prolate ellipsoid describing collimated outflows. The rendered representation is akin to the narrow band  $H\alpha$ + $[N\text{ II}]$  image from Schwarz et al. (1992). The dense toroidal shell of M 3-30 seen in the  $H\alpha$ + $[N\text{ II}]$  emission is similar to the PN Abell 48 (Danehkar et al. 2014), while M 3-30 also contains collimated outflows. The maximum velocity of the collimated outflows in the P–V diagram of the  $H\alpha$  emission corresponds to the outflow velocity of  $v_{\text{out}} \approx \pm 80 \text{ km s}^{-1}$  relative to  $v_{\text{sys}} = 79 \text{ km s}^{-1}$  at the inclination of  $30^\circ$  found by our model. The expansion velocity of the shell is about  $v_{\text{exp}} = 36 \pm 10 \text{ km s}^{-1}$  similar to  $v_{\text{HWHM}} = 36 \pm 5 \text{ km s}^{-1}$  derived the volume-integrated line profiles.

The *HST* observation of Hb 4 in Figure 8 indicates that the main shell has a deformed ring-like structure probably due to the interaction with the ISM. Moreover, The *HST* observation shows that the point-symmetric knots or filaments are not vertically aligned, which again hints at the ISM interaction. Accordingly, we used a SHAPE model that consists of an equatorial dense torus and two point-symmetric knots. The P–V diagrams imply the expansion velocity of the shell reaching  $v_{\text{exp}} = 60 \pm 20 \text{ km s}^{-1}$  at the inclination of  $40^\circ$  found by the morpho-kinematic model, while the mean HWHM expansion velocity of  $v_{\text{HWHM}} = 23 \pm 1 \text{ km s}^{-1}$  is estimated

from the line profiles integrated over an aperture covering the main shell. The deprojected velocity of the bipolar collimated outflows are found to be in the range of  $v_{\text{out}} = \pm 15\text{--}170 \text{ km s}^{-1}$  at  $i = 40^\circ \pm 3^\circ$ . The P–V diagrams disclose the deceleration of the point-symmetric knots, which were also recently identified by Derlopa et al. (2019). This deceleration is not a typical Hubble-type flow (Steffen et al. 2009) of PNe linearly increasing with distance. This kind of decelerating bow shocks has been found in a Herbig-Haro (HH) object HH34 (Devine et al. 1997) and a post-AGB water-fountain star IRAS 18113–2503 (Orosz et al. 2019), which could be due to shock collisions and interactions with ambient media. Point-symmetric knots and LISs in other PNe also demonstrate some signs of shock excitation (Akras & Gonçalves 2016) and molecular  $H_2$  emission (Akras et al. 2017, 2020) because of the interaction with the ISM or their exterior nebula halos. To model decelerating shock fronts of the bipolar collimated outflows, we employed two semi-ellipsoids whose velocities linearly decrease with distance from the nebular center, while their rears still have a Hubble-type homologous flow. This allowed us to reproduce velocity channel maps. The velocity dispersion maps also depict higher values at the locations of these knots, which again imply shock collisions with the surrounding medium.

The morpho-kinematic model of IC 1297 was made using a dense ellipsoid being wider and shorter toward the southwest, likely due to the interaction with ISM similar to M 2-42 (Danehkar et al. 2016). The velocity dispersion maps show higher values in the south part of the nebula. Although the  $H\alpha$  velocity map in Figure 1 is similar to that of M 3-30, but the P–V diagram and velocity channel maps do not suggest the same morpho-kinematic model. The narrow band  $H\alpha$ + $[N\text{ II}]$  image by Schwarz et al. (1992) suggests an elliptical morphology with the same on-sky orientations seen in the WiFeS observations. Polar expansion velocities are estimated to be  $v_{\text{out}} = \pm 100 \pm 10 \text{ km s}^{-1}$  based on the P–V diagrams, while a mean waist expansion velocity of  $v_{\text{exp}} = 31 \pm 1 \text{ km s}^{-1}$  is found by the HWHM results.

The *HST* image of Pe 1-1 (see Figure 8) allowed us to construct a morpho-kinematic model for this object. Moreover, the IFU velocity dispersion maps shown in Figure 1 imply the presence of two point-symmetric knots on both sides of the nebula similar to point-symmetric knots visible in the dispersion maps of Hb 4. High values of the velocity dispersion could be due to the interaction with the ambient medium. We therefore employed a prolate ellipsoidal structure, including two point-symmetric structures protruded from both sides of the ellipsoid.

To model M 1-32, we exploited an equatorial dense torus resembling its  $H\alpha$ + $[N\text{ II}]$  image (see Figure 8), and a thin prolate ellipsoid reproducing collimated bipolar outflows reaching  $v_{\text{out}} = \pm 170 \pm 20 \text{ km s}^{-1}$  relative to the central star in the P–V arrays (see Figure 3). The velocity dispersion maps depict high values at the central region that is similar to that in Th 2-A, similarly viewed almost pole-on (Danehkar 2015). High-velocity collimated bipolar outflows with a very low inclination ( $i = 5^\circ$ ) make those high values in the dispersion maps. Previously, Akras & López (2012) estimated  $v_{\text{out}} = \pm 200 \text{ km s}^{-1}$  at  $i = 5^\circ$ . The HWHM measurements of the

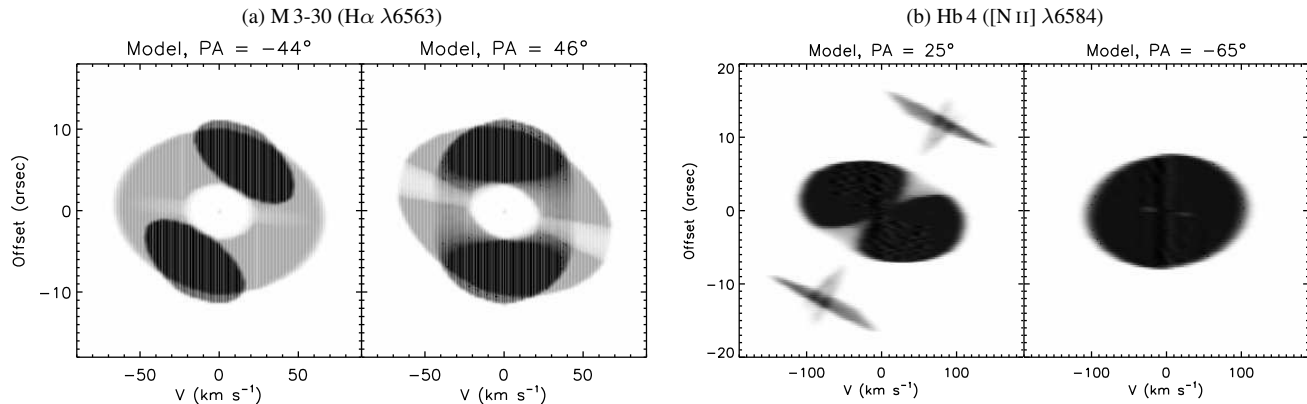


**Figure 6.** Synthetic P–V diagrams for (a) M3-30, (b) Hb4, (c) IC 1297, (d) Pe 1-1, (e) M1-32, (f) M3-15, (g) M1-25, (h) Hen 2-142, (i) K2-16, (j) NGC 6578, (k) NGC 6567, and (l) NGC 6629, produced by slits oriented with the position angles (PA) along and vertical to the symmetric axis through the nebular center for the best-fitting morpho-kinematic models reproducing the P–V arrays in the H $\alpha$   $\lambda$ 6563 or [N II]  $\lambda$ 6584 emission (listed in round brackets following the PN name), with the parameters given in Table 3. The complete figure set (12 images) is available in the online journal.

**Fig. Set 6.** Synthetic P–V diagrams for (a) M3-30, (b) Hb4, (c) IC 1297, (d) Pe 1-1, (e) M1-32, (f) M3-15, (g) M1-25, (h) Hen 2-142, (i) K2-16, (j) NGC 6578, (k) NGC 6567, and (l) NGC 6629, produced by the best-fitting morpho-kinematic models for velocity slices along the H $\alpha$   $\lambda$ 6563 or [N II]  $\lambda$ 6584 emission (listed in round brackets following the PN name), with the parameters given in Table 3.

**Table 3.** Key parameters of the best-fitting morpho-kinematic models and morphological classification.

Name	CSPN	PNG	PA ( $^{\circ}$ )	GPA ( $^{\circ}$ )	$i$ ( $^{\circ}$ )	$v_{\text{exp}}$ (km/s)	$v_{\text{out}}$ (km/s)	Morphology <sup>b</sup>	
								P	S
PB 6	[WO 1]	278.8+04.9	80.0 $\pm$ 7.0	45.3 $\pm$ 7.0	–	33.0 $\pm$ 70.0		<i>MI?</i>	<i>ps(m)?</i>
M3-30	[WO 1]	017.9–04.8	–44.0 $\pm$ 4.0	19.2 $\pm$ 4.0	30.0 $\pm$ 5.0	36.0 $\pm$ 80.0		<i>E,o</i>	<i>rg,ps(s)</i>
Hb 4	[WO 3]	003.1+02.9	25.0 $\pm$ 3.0	83.3 $\pm$ 3.0	–40.0 $\pm$ 3.0	23.0 $\pm$ 15.0 $\cdots$ 170.0		<i>E,o</i>	<i>rg,ps(an)</i>
IC 1297	[WO 3]	358.3–21.6	32.0 $\pm$ 5.0	104.0 $\pm$ 5.0	–155.0 $\pm$ 6.0	31.0 $\pm$ 100.0 $\pm$ 10.0		<i>E,c</i>	
Pe 1-1	[WO 4]	285.4+01.5	–75.0 $\pm$ 4.0	–104.2 $\pm$ 4.0	75.0 $\pm$ 4.0	23.0 $\pm$ 60.0 $\cdots$ 100.0		<i>E,o/c</i>	<i>ps(m,an)</i>
M1-32	[WO 4] <sub>pec</sub>	011.9+04.2	–40.0 $\pm$ 6.0	20.1 $\pm$ 6.0	5.0 $\pm$ 3.0	31.0 $\pm$ 170.0 $\pm$ 20.0		<i>E,o</i>	<i>rg,ps(s)</i>
M3-15	[WC 4]	006.8+04.1	40.0 $\pm$ 4.0	98.8 $\pm$ 4.0	5.0 $\pm$ 4.0	21.0 $\pm$ 80.0 $\pm$ 20.0		<i>E,o</i>	<i>rg,ps(s)</i>
M1-25	[WC 5-6]	004.9+04.9	30.0 $\pm$ 5.0	88.0 $\pm$ 5.0	80.0 $\pm$ 3.0	27.0 $\gtrsim$ $\pm$ 100.0		<i>E,c</i>	
Hen 2-142	[WC 9]	327.1–02.2	–45.0 $\pm$ 3.0	–4.3 $\pm$ 3.0	–60.0 $\pm$ 3.0	20.0 $\gtrsim$ $\pm$ 100.0		<i>E,c</i>	
K2-16	[WC 11]	352.9+11.4	80.0 $\pm$ 6.0	130.6 $\pm$ 6.0	–30.0 $\pm$ 5.0	31.0 $\pm$ 70.0 $\pm$ 10.0		<i>E,o</i>	<i>rg,ps(s)</i>
NGC 6578	<i>wels</i>	010.8–01.8	–48.0 $\pm$ 6.0	13.6 $\pm$ 6.0	–45.0 $\pm$ 5.0	22.0 $\approx$ $\pm$ 80.0		<i>E,c</i>	
NGC 6567	<i>wels</i>	011.7–00.6	–40.0 $\pm$ 3.0	21.4 $\pm$ 3.0	46.0 $\pm$ 3.0	34.0 $\approx$ $\pm$ 110.0		<i>E,c</i>	
NGC 6629	<i>wels</i>	009.4–05.0	–40.0 $\pm$ 3.0	22.6 $\pm$ 3.0	60.0 $\pm$ 4.0	20.0 $\approx$ $\pm$ 100.0		<i>E,c</i>	
Sa 3-107	<i>wels</i>	358.0–04.6	40.0 $\pm$ 8.0	100.5 $\pm$ 8.0	–	16.0 $\gtrsim$ $\pm$ 60.0		<i>B/E?</i>	

**Note.** Morphological classification codes in Columns 9–10 are based on Sahai et al. (2011). The symbol ‘?’ means that further observation is required to confirm the structure. The deprojected outflow velocities ( $v_{\text{out}}$ ) of collimated outflows or polar expansions are respect to the systemic velocities (see Table 2). The mean expansion velocities ( $v_{\text{exp}}$ ) are from the HWHM measurements of the integrated line profiles.

integrated line profiles also yield a mean expansion velocity of  $31 \pm 3 \text{ km s}^{-1}$ .

The SHAPE model of M3-15 was made with an equatorial dense torus based on the *HST* observation (see Figure 8), and a thin prolate ellipsoid associated with collimated bipolar outflows with  $v_{\text{out}} = \pm 80 \pm 20 \text{ km s}^{-1}$  relative to the nebular center according to the P–V diagrams (see Figure 3). This model is similar to that adopted by Akras & López (2012), leading to outflow velocities of  $\pm 100 \text{ km s}^{-1}$  based on long-slit observations. Our inclination of  $5^{\circ}$  with respect to the line of sight is also in full agreement with Akras &

López (2012). The *HST* image clearly illustrates how this PN is oriented on the sky plane, in agreement with our IFU velocity maps in Figure 1. The *HST* image of this PN looks very similar to the PN Vy 1-2 with [WR] or *wels* has a similar morphology seen almost pole-on with an inclination angle of  $10^{\circ}$  (Akras et al. 2015).

The SHAPE wire-frame model of K2-16 has a elliptical structure extending from a denser torus. This model reproduces the P–V diagrams in the H $\alpha$  emission (see Figure 3). Taking the inclination of  $30^{\circ}$  found by the best-fit model, we derived a maximum polar expansion velocity of  $v_{\text{out}} = \pm 70 \pm$

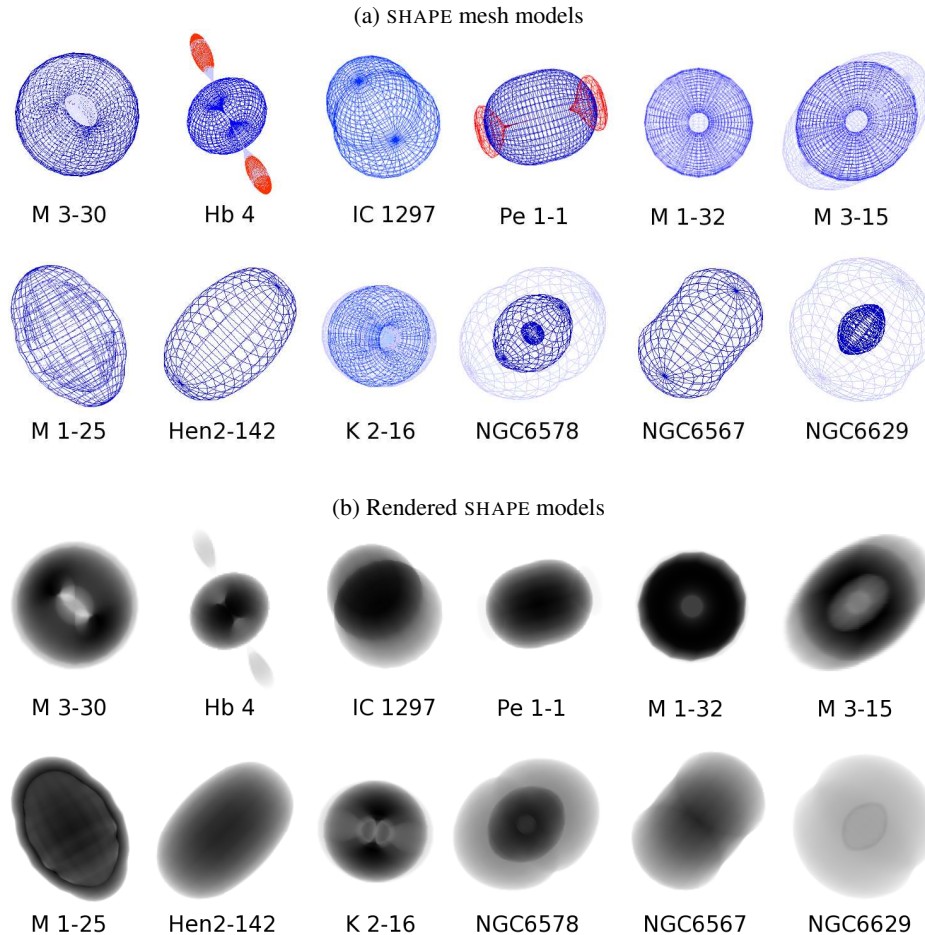


**Figure 7.** SHAPE morpho-kinematic models of the PNe: M 3-30, Hb 4, IC 1297, Th 2-A, Pe 1-1, M,1-32, M 3-15 (first row), M 1-25, Hen 2-142, K 2-16, MGC 6578, M 2-42, NGC 6567 and NGC 6629 (second row), (a) before and (b) after rendering at the best-fitting inclinations and orientations.

$10 \text{ km s}^{-1}$ . The HWHM velocities also implies a mean expansion velocity of  $v_{\text{exp}} = \pm 31 \pm 3 \text{ km s}^{-1}$ .

The high-resolution *HST* images of M 1-25, Hen 2-142, NGC 6578, NGC 6567 and NGC 6629 are employed to develop their elliptically symmetric morphological models. Although the spatial resolution of our IFU observations did not provide much details on their elliptical morphologies, the IFU velocity maps display their on-sky orientations in agreement with the *HST* images. Our morpho-kinematic models were built with modified prolate ellipsoids in a way that their final rendered images resemble their inherent shapes seen in the *HST* images. We also included tenuous exterior halos in NGC 6578 and NGC 6629, which are visible in the *HST* observations. The best-fitting orientations and inclinations of these models were constrained by the P–V diagrams (see Figure 6) and velocity channel maps (see Figure 5).

## 5. Conclusion

We have studied morpho-kinematic features of a sample of 14 Galactic PNe surrounding [WR]-type and *wels* nuclei, using spatially resolved kinematic maps and position–velocity diagrams derived from IFU observations. The kinematic data, together with archival images (see Figure 8), have been used to carry out morpho-kinematic modeling of the 12 PNe. Our results imply that these 12 objects have elliptical axisymmetric morphologies with either open or closed outer

ends. Collimated outflows are found to be present in the PNe Hb 4, Pe 1-1, M 3-30, M 1-32, M 3-15, and K 2-16, while point-symmetric knots or collimated outflows are detached in Hb 4. Axisymmetric morphologies and collimated outflows have been detected in other PNe around [WR] stars (Akras & López 2012). Some elliptical PNe having FLIERs were found to have “diffuse X-ray” sources (Kastner et al. 2012). Other aspherical PNe around [WR] stars were reported to contain diffuse X-ray sources and hot bubbles, such as NGC 40 (Montez et al. 2005) and NGC 5315 (Kastner et al. 2008). Diffuse X-ray emission could be associated with collimated jets and wind-wind shocks (Kastner et al. 2012), whereas hard X-ray emission may be related to the mass accretion into a binary companion.

The PNe in our sample have elliptically symmetric morphologies, apart from PB 6 and Sa 3-107, that could imply a possible link between the nebulae and their WR-type nuclei. PB 6 around a [WO 1] star likely has a complex morphology containing multi-scale structures similar to NGC 5189 with a [WO 1] star (Danekhar et al. 2018). Although we do not have any imaging observations of Sa 3-107, its IFU velocity maps suggest an axisymmetric morphology. The theoretical evolutionary models by Schönberner et al. (2005a,b) predicted that the expansion velocity increases as the nebula evolves and the central star becomes hotter. However, we cannot see any link between the nebular kinematics and stellar characteristics

listed in Table 1. Some PNe with hot stars such as Pe 1-1 and Hb 4 have low mean expansion (HWHM) velocities, whereas some PNe around cool stars such as K 2-16 show high mean expansion velocities. This tendency does not seem to be explained by single star evolution, since the nebular mean expansion velocities are not linked to their stellar parameters. Moreover, collimated bipolar outflows were found in some objects, Hb 4, M 3-30, M 1-32, and M 3-15, reaching outflow velocities in the range  $60\text{--}200\text{ km s}^{-1}$  with respect to their central stars, which cannot completely be produced by the GISW model.

The spatial and spectral resolutions of our IFU observations correctly describe the on-sky orientations of the elliptical morphologies of the interior shells in the PNe NGC 6578 and NGC 6629, as well as the compact ( $\leq 6$  arcsec) PNe Pe 1-1, M 3-15, M 1-25, Hen 2-142, and NGC 6567, as verified by the *HST* imaging observations. Although the WiFeS cannot resolve morphological details of compact objects with angular diameters less than 6 arcsec, it allows us to easily determine on-sky orientations of overall morphologies, as previously shown by Danehkar & Parker (2015). This study demonstrates that spatial and spectral resolution of the WiFeS are appropriate to conduct a large IFU survey of many objects, where precise morphological details are not necessary.

Future high-resolution imaging and kinematic observations of other PNe around [WR] and *wels* nuclei will definitely shed light on the mechanism that shapes axisymmetric morphologies in these objects. In-deep spectroscopic and lightcurve observations of their central stars will help us gain a better understanding of them. The presence of binary companions should be investigated that can be responsible for axisymmetric morphologies. Nevertheless, an aspherical morphology can also be formed by a planet that it is extremely difficult to detect. Further studies of [WR] CSPNe will unravel the puzzle of the mechanism that produces elliptical and bipolar morphologies in PNe.

This work is partially based on the dissertation by the author (Danehkar 2014), supported by an international Macquarie University Research Excellence Scholarship (iMQRES) and a Sigma Xi Grants-in-Aid of Research (GIAR). The author would like to thank Quentin A. Parker for supporting the 2010 ANU observations, Milorad Stupar for his guidance on IRAF data reduction, Wolfgang Steffen for helpful discussions and guidance on SHAPE, Nico Koning for upgrading SHAPE and support, David J. Frew for helping with the observing proposal, Kyle DePew for carrying out the ANU observations in 2010, and the ANU telescope time allocation committee and the staff at the ANU Siding Spring Observatory for their support. Based on observations made with the NASA/ESA *Hubble Space Telescope*, obtained from the Data Archive at the Space Telescope Science Institute, which is operated by the Association of Universities for Research in Astronomy, Inc., under NASA contract NAS 5-26555.

*Software:* IDL Astronomy User's Library (Landsman 1993), IDL Coyote Library (Fanning 2011).

*Facilities:* ATT (WiFeS), *HST*

## Appendix

### A. Archival *HST* and Ground-based Images

Figure 8 shows high-angular resolution *HST* images of PB 6, Hb 4, Pe 1-1, M 3-15, M 1-25, Hen 2-142, NGC 6578, NGC 6567 and NGC 6629 retrieved from the *HST* archive, and  $\text{H}\alpha$ + $[\text{N II}]$  images of M 3-30, IC 1297, M 1-32 and K 2-16 taken with the 3.5-m ESO NTT from Schwarz et al. (1992). Table 4 lists the *HST* images, together with their program IDs, instruments, filters/gratings, wavelength bands, spatial resolutions, and exposure times.

### B. Supplementary Data

The following figure sets are available for the electronic edition of this article:

**Fig. Set 1.** The spatial distribution maps of logarithmic flux intensity, continuum, LSR velocity, and velocity dispersion of the  $\text{H}\alpha$   $\lambda 6563$  and  $[\text{N II}]$   $\lambda 6584$  emission lines for: (a) PB 6, (b) M 3-30, (c) Hb 4, (d) IC 1297, (e) Pe 1-1, (f) M 1-32, (g) M 3-15, (h) M 1-25, (i) Hen 2-142, (j) K 2-16, (k) NGC 6578, (l) NGC 6567, (m) NGC 6629, and (n) Sa 3-107.

**Fig. Set 2.** Velocity slices along the  $\text{H}\alpha$   $\lambda 6563$  and  $[\text{N II}]$   $\lambda 6584$  emission-line profiles for: (a) PB 6, (b) M 3-30, (c) Hb 4, (d) IC 1297, (e) Pe 1-1, (f) M 1-32, (g) M 3-15, (h) M 1-25, (i) Hen 2-142, (j) K 2-16, (k) NGC 6578, (l) NGC 6567, (m) NGC 6629, and (n) Sa 3-107.

**Fig. Set 3.** P–V arrays in the  $\text{H}\alpha$   $\lambda 6563$  and  $[\text{N II}]$   $\lambda 6584$  emissions for: (a) PB 6, (b) M 3-30, (c) Hb 4, (d) IC 1297, (e) Pe 1-1, (f) M 1-32, (g) M 3-15, (h) M 1-25, (i) Hen 2-142, (j) K 2-16, (k) NGC 6578, (l) NGC 6567, (m) NGC 6629, and (n) Sa 3-107.

**Fig. Set 4.** SHAPE mesh models for: (a) M 3-30, (b) Hb 4, (c) IC 1297, (d) Pe 1-1, (e) M 1-32, (f) M 3-15, (g) M 1-25, (h) Hen 2-142, (i) K 2-16, (j) NGC 6578, (k) NGC 6567, and (l) NGC 6629.

**Fig. Set 5.** Synthetic velocity-resolved channel maps for: (a) M 3-30, (b) Hb 4, (c) IC 1297, (d) Pe 1-1, (e) M 1-32, (f) M 3-15, (g) M 1-25, (h) Hen 2-142, (i) K 2-16, (j) NGC 6578, (k) NGC 6567, and (l) NGC 6629.

**Fig. Set 6.** Synthetic P–V diagrams for (a) M 3-30, (b) Hb 4, (c) IC 1297, (d) Pe 1-1, (e) M 1-32, (f) M 3-15, (g) M 1-25, (h) Hen 2-142, (i) K 2-16, (j) NGC 6578, (k) NGC 6567, and (l) NGC 6629.

### ORCID iDs

A. Danehkar  <https://orcid.org/0000-0003-4552-5997>

### References

- Acker, A. 1976, Publication de l'Observatoire de Strasbourg, 4, 1  
 Acker, A., Gesicki, K., Grosdidier, Y., & Durand, S. 2002, *A&A*, 384, 620  
 Acker, A., Marcout, J., Ochsenbein, F., et al. 1992, The Strasbourg-ESO Catalogue of Galactic Planetary Nebulae. Parts I, II.  
 Acker, A. & Neiner, C. 2003, *A&A*, 403, 659  
 Akras, S., Boumis, P., Meaburn, J., et al. 2015, *MNRAS*, 452, 2911  
 Akras, S., Clyne, N., Boumis, P., et al. 2016, *MNRAS*, 457, 3409  
 Akras, S. & Gonçalves, D. R. 2016, *MNRAS*, 455, 930  
 Akras, S., Gonçalves, D. R., & Ramos-Larios, G. 2017, *MNRAS*, 465, 1289  
 Akras, S., Gonçalves, D. R., Ramos-Larios, G., & Aleman, I. 2020, *MNRAS*, 493, 3800  
 Akras, S. & López, J. A. 2012, *MNRAS*, 425, 2197  
 Balick, B. 1987, *AJ*, 94, 671  
 Balick, B. & Frank, A. 2002, *ARA&A*, 40, 439

**Table 4.** Journal of archival *HST* images of the planetary nebulae in our sample.

Name	Instrument	Aperture	Filters/ Gratings	Wavelength range (Å)	Plate scale (arcsec/pix)	Exp. (sec)	Program ID	PI
PB 6	STIS	F28X50LP	MIRVIS	4950–9450	0.050	22	12600	R. Dufour
Hb 4	WFPC2	PC	F658N	6570–6598	0.045	600	6347	K. Borkowski
Pe 1-1	WFC3	UVIS	F502N	4963–5059	0.039	600	11657	L. Stanghellini
M 3-15	WFPC2	PC	F656N	6552–6570	0.045	200	9356	A. Zijlstra
M 1-25	WFPC2	PC	F658N	6570–6598	0.045	480	8345	R. Sahai
Hen 2-142	WFPC2	PC	F656N	6552–6570	0.045	2040	6353	R. Sahai
NGC 6578	WFPC2	PC	F658N	6570–6598	0.045	1200	11122	B. Balick
NGC 6567	NICMOS	NIC	F108N	10797–10836	0.043	384	7837	S. Pottasch
NGC 6629	WFPC2	PC	F555W	4789–6025	0.045	10	6119	H. Bond

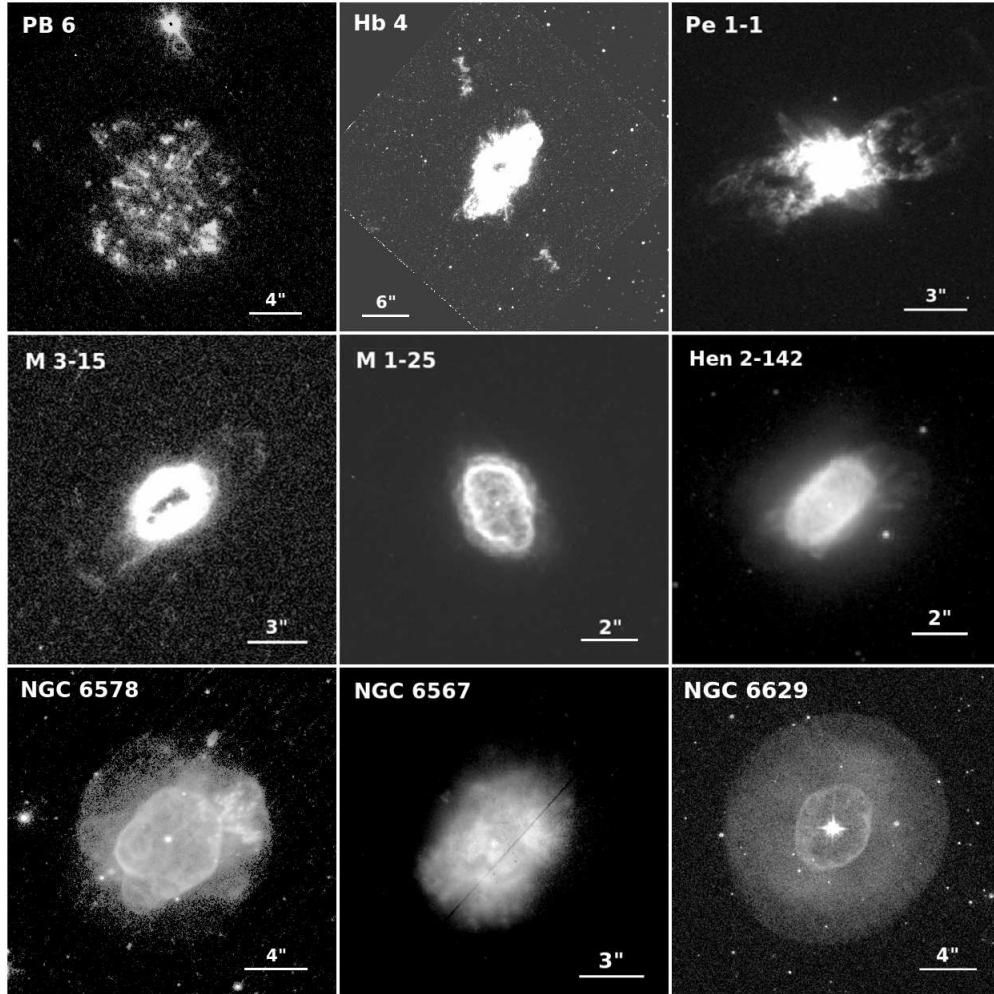


**Figure 8.** The *HST* images of PB 6, Hb 4, Pe 1-1, M 3-15, M 1-25, Hen 2-142, NGC 6578, NGC 6567 and NGC 6629, with the instruments and filters/gratings listed in Table 4; the narrow-band  $H\alpha+[N\ II]$  filter images of M 3-30, IC 1297, M 1-32 and K 2-16 taken with the 3.5-m ESO NTT from Schwarz et al. (1992). The image scales are shown by solid lines. North is up and east is toward the left-hand side.

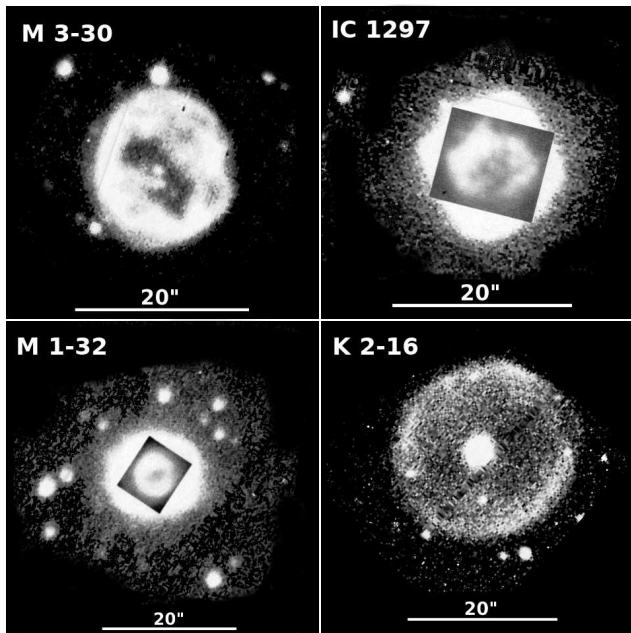


Figure 8. – continued

- Balick, B., Perinotto, M., Maccioni, A., Terzian, Y., & Hajian, A. 1994, *ApJ*, **424**, 800
- Balick, B., Preston, H. L., & Icke, V. 1987, *AJ*, **94**, 1641
- Balick, B., Rugers, M., Terzian, Y., & Chengalur, J. N. 1993, *ApJ*, **411**, 778
- Blöcker, T. 1995, *A&A*, **299**, 755
- Clark, D. M., López, J. A., Steffen, W., & Richer, M. G. 2013, *AJ*, **145**, 57
- Clegg, R. E. S., Miller, S., Storey, P. J., & Kisielius, R. 1999, *A&AS*, **135**, 359
- Corradi, R. L. M., Manso, R., Mampaso, A., & Schwarz, H. E. 1996, *A&A*, **313**, 913
- Corradi, R. L. M. & Schwarz, H. E. 1995, *A&A*, **293**, 871
- Crowther, P. A., De Marco, O., & Barlow, M. J. 1998, *MNRAS*, **296**, 367
- Danehkar, A. 2014, *Evolution of Planetary Nebulae with WR-type Central Stars*, PhD thesis, Macquarie University
- Danehkar, A. 2015, *ApJ*, **815**, 35
- Danehkar, A. 2018, *Publ. Astron. Soc. Australia*, **35**, e005
- Danehkar, A. 2021, *arXiv e-prints*, arXiv:2106.10762
- Danehkar, A., Karovska, M., Maksym, W. P., & Montez, Rodolfo, J. 2018, *ApJ*, **852**, 87
- Danehkar, A. & Parker, Q. A. 2015, *MNRAS*, **449**, L56
- Danehkar, A., Parker, Q. A., & Steffen, W. 2016, *AJ*, **151**, 38
- Danehkar, A., Todt, H., Ercolano, B., & Kniazev, A. Y. 2014, *MNRAS*, **439**, 3605
- De Marco, O. 2009, *PASP*, **121**, 316
- Depew, K., Parker, Q. A., Miszalski, B., et al. 2011, *MNRAS*, **414**, 2812
- Derlopa, S., Akras, S., Boumis, P., & Steffen, W. 2019, *MNRAS*, **484**, 3746
- Devine, D., Bally, J., Reipurth, B., & Heathcote, S. 1997, *AJ*, **114**, 2095
- Dopita, M., Hart, J., McGregor, P., et al. 2007, *Ap&SS*, **310**, 255
- Dopita, M., Rhee, J., Farage, C., et al. 2010, *Ap&SS*, **327**, 245
- Dopita, M. A., Lawrence, C. J., Ford, H. C., & Webster, B. L. 1985, *ApJ*, **296**, 390
- Dopita, M. A. & Meatheringham, S. J. 1991, *ApJ*, **377**, 480
- Dopita, M. A., Meatheringham, S. J., Webster, B. L., & Ford, H. C. 1988, *ApJ*, **327**, 639
- Durand, S., Acker, A., & Zijlstra, A. 1998, *A&AS*, **132**, 13
- Fanning, D. W. 2011, *Coyote's Guide to Traditional IDL Graphics* (Coyote Book Publishing)
- Frank, A. & Blackman, E. G. 2004, *ApJ*, **614**, 737
- García-Díaz, M. T., Clark, D. M., López, J. A., Steffen, W., & Richer, M. G. 2009, *ApJ*, **699**, 1633
- García-Rojas, J., Peña, M., & Peimbert, A. 2009, *A&A*, **496**, 139
- García-Segura, G. 1997, *ApJ*, **489**, L189
- García-Segura, G., Langer, N., Różycka, M., & Franco, J. 1999, *ApJ*, **517**, 767
- García-Segura, G. & López, J. A. 2000, *ApJ*, **544**, 336
- Gesicki, K. & Acker, A. 1996, *Ap&SS*, **238**, 101
- Gesicki, K. & Zijlstra, A. A. 2007, *A&A*, **467**, L29
- Gonçalves, D. R., Corradi, R. L. M., & Mampaso, A. 2001, *ApJ*, **547**, 302
- Gonçalves, D. R., Mampaso, A., Corradi, R. L. M., & Quireza, C. 2009, *MNRAS*, **398**, 2166
- Górny, S. K., Chiappini, C., Stasińska, G., & Cuisinier, F. 2009, *A&A*, **500**, 1089
- Górny, S. K., Stasińska, G., Escudero, A. V., & Costa, R. D. D. 2004, *A&A*, **427**, 231
- Górny, S. K., Stasińska, G., & Tyłenda, R. 1997, *A&A*, **318**, 256
- Huckvale, L., Prouse, B., Jones, D., et al. 2013, *MNRAS*, **434**, 1505
- Jones, D., Lloyd, M., Santander-García, M., et al. 2010, *MNRAS*, **408**, 2312
- Jones, D., Mitchell, D. L., Lloyd, M., et al. 2012, *MNRAS*, **420**, 2271
- Kahn, F. D. & West, K. A. 1985, *MNRAS*, **212**, 837
- Kaler, J. B., Shaw, R. A., Feibelman, W. A., & Imhoff, C. L. 1991, *PASP*, **103**, 67
- Kastner, J. H., Montez, Jr., R., Balick, B., & De Marco, O. 2008, *ApJ*, **672**, 957
- Kastner, J. H., Montez, Jr., R., Balick, B., et al. 2012, *AJ*, **144**, 58
- Koesterke, L. & Hamann, W.-R. 1997, *A&A*, **320**, 91
- Kohoutek, L. 1977, *A&A*, **59**, 137
- Kwok, S. 2010, *Publ. Astron. Soc. Australia*, **27**, 174
- Kwok, S., Purton, C. R., & Fitzgerald, P. M. 1978, *ApJ*, **219**, L125
- Landsman, W. B. 1993, in *ASP Conf. Ser.*, Vol. 52, *Astronomical Data Analysis Software and Systems II*, ed. R. J. Hanisch, R. J. V. Brissenden, & J. Barnes (San Francisco, CA: ASP), 246
- Lasker, B. M., Lattanzi, M. G., McLean, B. J., et al. 2008, *AJ*, **136**, 735
- Leuenhagen, U. & Hamann, W.-R. 1998, *A&A*, **330**, 265
- Leuenhagen, U., Hamann, W.-R., & Jeffery, C. S. 1996, *A&A*, **312**, 167
- López, J. A., García-Díaz, M. T., Steffen, W., Riesgo, H., & Richer, M. G. 2012, *ApJ*, **750**, 131
- López, J. A., Steffen, W., & Meaburn, J. 1997, *ApJ*, **485**, 697
- Markwardt, C. B. 2009, in *Astronomical Society of the Pacific Conference Series*, Vol. 411, *Astronomical Data Analysis Software and Systems XVIII*, ed. D. A. Bohlender, D. Durand, & P. Dowler, 251
- Medina, S., Peña, M., Morisset, C., & Stasińska, G. 2006, *Rev. Mex. Astron. Astrofis.*, **42**, 53
- Miszalski, B., Acker, A., Moffat, A. F. J., Parker, Q. A., & Udalski, A. 2009a, *A&A*, **496**, 813
- Miszalski, B., Acker, A., Parker, Q. A., & Moffat, A. F. J. 2009b, *A&A*, **505**, 249
- Mitchell, D. L., Pollacco, D., O'Brien, T. J., et al. 2007, *MNRAS*, **374**, 1404
- Montez, Jr., R., Kastner, J. H., De Marco, O., & Soker, N. 2005, *ApJ*, **635**, 381
- Nordhaus, J. & Blackman, E. G. 2006, *MNRAS*, **370**, 2004
- Nordhaus, J., Blackman, E. G., & Frank, A. 2007, *MNRAS*, **376**, 599
- Nordhaus, J., Spiegel, D. S., Ibgui, L., Goodman, J., & Burrows, A. 2010, *MNRAS*, **408**, 631
- Nugis, T. & Lamers, H. J. G. L. M. 2000, *A&A*, **360**, 227
- Orosz, G., Gómez, J. F., Imai, H., et al. 2019, *MNRAS*, **482**, L40
- Paczynski, B. 1976, in *IAU Symposium*, Vol. 73, *Structure and Evolution of Close Binary Systems*, ed. P. Eggleton, S. Mitton, & J. Whelan, 75
- Parker, Q. A., Philipps, S., Pierce, M., & et al. 2005, *MNRAS*, **362**, 689
- Pauldrach, A., Puls, J., Kudritzki, R. P., Méndez, R. H., & Heap, S. R. 1988, *A&A*, **207**, 123
- Peña, M., Stasińska, G., Esteban, C., et al. 1998, *A&A*, **337**, 866
- Peña, M., Stasińska, G., & Medina, S. 2001, *A&A*, **367**, 983
- Richer, M. G., Báez, S.-H., López, J. A., Riesgo, H., & García-Díaz, M. T. 2009, *Rev. Mex. Astron. Astrofis.*, **45**, 239
- Sahai, R., Morris, M. R., & Villar, G. G. 2011, *AJ*, **141**, 134
- Schönberner, D., Jacob, R., Sandin, C., & Steffen, M. 2010, *A&A*, **523**, A86
- Schönberner, D., Jacob, R., & Steffen, M. 2005b, *A&A*, **441**, 573
- Schönberner, D., Jacob, R., Steffen, M., et al. 2005a, *A&A*, **431**, 963
- Schwarz, H. E., Corradi, R. L. M., & Melnick, J. 1992, *A&AS*, **96**, 23
- Shaw, R. A. & Kaler, J. B. 1989, *ApJS*, **69**, 495
- Soker, N. 1990, *AJ*, **99**, 1869
- Soker, N. 2006, *PASP*, **118**, 260
- Soker, N. & Harpaz, A. 1992, *PASP*, **104**, 923
- Soker, N. & Livio, M. 1994, *ApJ*, **421**, 219
- Stanghellini, L., Corradi, R. L. M., & Schwarz, H. E. 1993, *A&A*, **279**, 521
- Stanghellini, L. & Haywood, M. 2010, *ApJ*, **714**, 1096
- Steffen, W., García-Segura, G., & Koning, N. 2009, *ApJ*, **691**, 696
- Steffen, W., Koning, N., Wenger, S., Morisset, C., & Magnor, M. 2011, *IEEE Trans. Vis. Comput. Graphics*, **17**, 17
- Steffen, W. & López, J. A. 2006, *Rev. Mex. Astron. Astrofis.*, **42**, 99
- Tyłenda, R., Acker, A., Raytchev, B., Stenholm, B., & Gleizes, F. 1991, *A&AS*, **89**, 77
- Tyłenda, R., Acker, A., & Stenholm, B. 1993, *A&AS*, **102**, 595
- Tyndall, A. A., Jones, D., Lloyd, M., O'Brien, T. J., & Pollacco, D. 2012, *MNRAS*, **422**, 1804
- van der Hucht, K. A. 2001, *New Astro. Rev.*, **45**, 135
- van der Hucht, K. A., Conti, P. S., Lundstrom, I., & Stenholm, B. 1981, *Space Sci. Rev.*, **28**, 227
- van Dokkum, P. G. 2001, *PASP*, **113**, 1420
- Weidmann, W. A., Gamen, R., Díaz, R. J., & Niemela, V. S. 2008, *A&A*, **488**, 245
- Weidmann, W. A., Schmidt, E. O., Vena Valdarenas, R. R., et al. 2016, *A&A*, **592**, A103
- Weinberger, R. 1989, *A&AS*, **78**, 301
- Werner, K. & Herwig, F. 2006, *PASP*, **118**, 183
- Zuckerman, B. & Aller, L. H. 1986, *ApJ*, **301**, 772

## Appendix

### B. Supplementary Data

The following figure sets are available for the electronic edition of this article:

**Fig. Set 1.** From left to right, the spatial distribution maps of logarithmic flux intensity, continuum, LSR velocity, and velocity dispersion of the  $H\alpha$   $\lambda 6563$  and  $[N II]$   $\lambda 6584$  emission lines for: (a) PB 6, (b) M 3-30, (c) Hb 4, (d) IC 1297, (e) Pe 1-1, (f) M 1-32, (g) M 3-15, (h) M 1-25, (i) Hen 2-142, (j) K 2-16, (k) NGC 6578, (l) NGC 6567, (m) NGC 6629, and (n) Sa 3-107. Fluxes are in logarithm of  $10^{-15} \text{ erg s}^{-1} \text{ cm}^{-2} \text{ spaxel}^{-1}$  unit, continua in  $10^{-15} \text{ erg s}^{-1} \text{ cm}^{-2} \text{ \AA}^{-1} \text{ spaxel}^{-1}$ , and LSR velocities and velocity dispersion in  $\text{km s}^{-1}$ . The white/black contour in each panel shows the narrow-band  $H\alpha$  emission in arbitrary unit retrieved from the SHS. North is up and east is toward the left-hand side.

**Fig. Set 2.** Velocity slices along the  $H\alpha$   $\lambda 6563$  and  $[N II]$   $\lambda 6584$  emission-line profiles for: (a) PB 6, (b) M 3-30, (c) Hb 4, (d) IC 1297, (e) Pe 1-1, (f) M 1-32, (g) M 3-15, (h) M 1-25, (i) Hen 2-142, (j) K 2-16, (k) NGC 6578, (l) NGC 6567, (m) NGC 6629, and (n) Sa 3-107. Each slice has a  $\sim 21 \text{ km s}^{-1}$  width, whose central velocity is given in  $\text{km s}^{-1}$  unit at the top of the panel. The LSR systemic velocity ( $v_{\text{sys}}$ ) of each object is given in  $\text{km s}^{-1}$  unit in the right bottom corner. The flux color is in logarithm of  $10^{-15} \text{ erg s}^{-1} \text{ cm}^{-2} \text{ spaxel}^{-1}$  unit. The contour in each panel shows the narrow-band  $H\alpha$  emission in arbitrary unit retrieved from the SHS. North is up and east is toward the left-hand side.

**Fig. Set 3.** P–V arrays in the  $H\alpha$   $\lambda 6563$  and  $[N II]$   $\lambda 6584$  emissions for: (a) PB 6, (b) M 3-30, (c) Hb 4, (d) IC 1297, (e) Pe 1-1, (f) M 1-32, (g) M 3-15, (h) M 1-25, (i) Hen 2-142, (j) K 2-16, (k) NGC 6578, (l) NGC 6567, (m) NGC 6629, and (n) Sa 3-107. Slits oriented with the position angles (PA) along and vertical to the symmetric axis through the central star, respectively. The velocity is with respect to the systemic velocity of the object, given in  $\text{km s}^{-1}$  unit. The angular offset at 0 arcsec is the nebular center.

**Fig. Set 4.** SHAPE mesh models for: (a) M 3-30, (b) Hb 4, (c) IC 1297, (d) Pe 1-1, (e) M 1-32, (f) M 3-15, (g) M 1-25, (h) Hen 2-142, (i) K 2-16, (j) NGC 6578, (k) NGC 6567, and (l) NGC 6629, before rendering at two different inclination angles ( $i = 0^\circ$  and  $90^\circ$ ), the best-fitting inclination and orientation, and the rendered image, respectively. The best-fitting parameters are listed in Table 3.

**Fig. Set 5.** Synthetic velocity-resolved channel maps for: (a) M 3-30, (b) Hb 4, (c) IC 1297, (d) Pe 1-1, (e) M 1-32, (f) M 3-15, (g) M 1-25, (h) Hen 2-142, (i) K 2-16, (j) NGC 6578, (k) NGC 6567, and (l) NGC 6629, produced by the best-fitting morpho-kinematic models for velocity slices along the  $H\alpha$   $\lambda 6563$  or  $[N II]$   $\lambda 6584$  emission (listed in round brackets following the PN name), with the parameters given in Table 3.

**Fig. Set 6.** Synthetic P–V diagrams for (a) M 3-30, (b) Hb 4, (c) IC 1297, (d) Pe 1-1, (e) M 1-32, (f) M 3-15, (g) M 1-25, (h) Hen 2-142, (i) K 2-16, (j) NGC 6578, (k) NGC 6567, and (l) NGC 6629, produced by slits oriented with the position angles (PA) along and vertical to the symmetric axis through the nebular center for the best-fitting morpho-kinematic models reproducing the P–V arrays in the  $H\alpha$   $\lambda 6563$  or  $[N II]$   $\lambda 6584$  emission (listed in round brackets following the PN name), with the parameters given in Table 3.

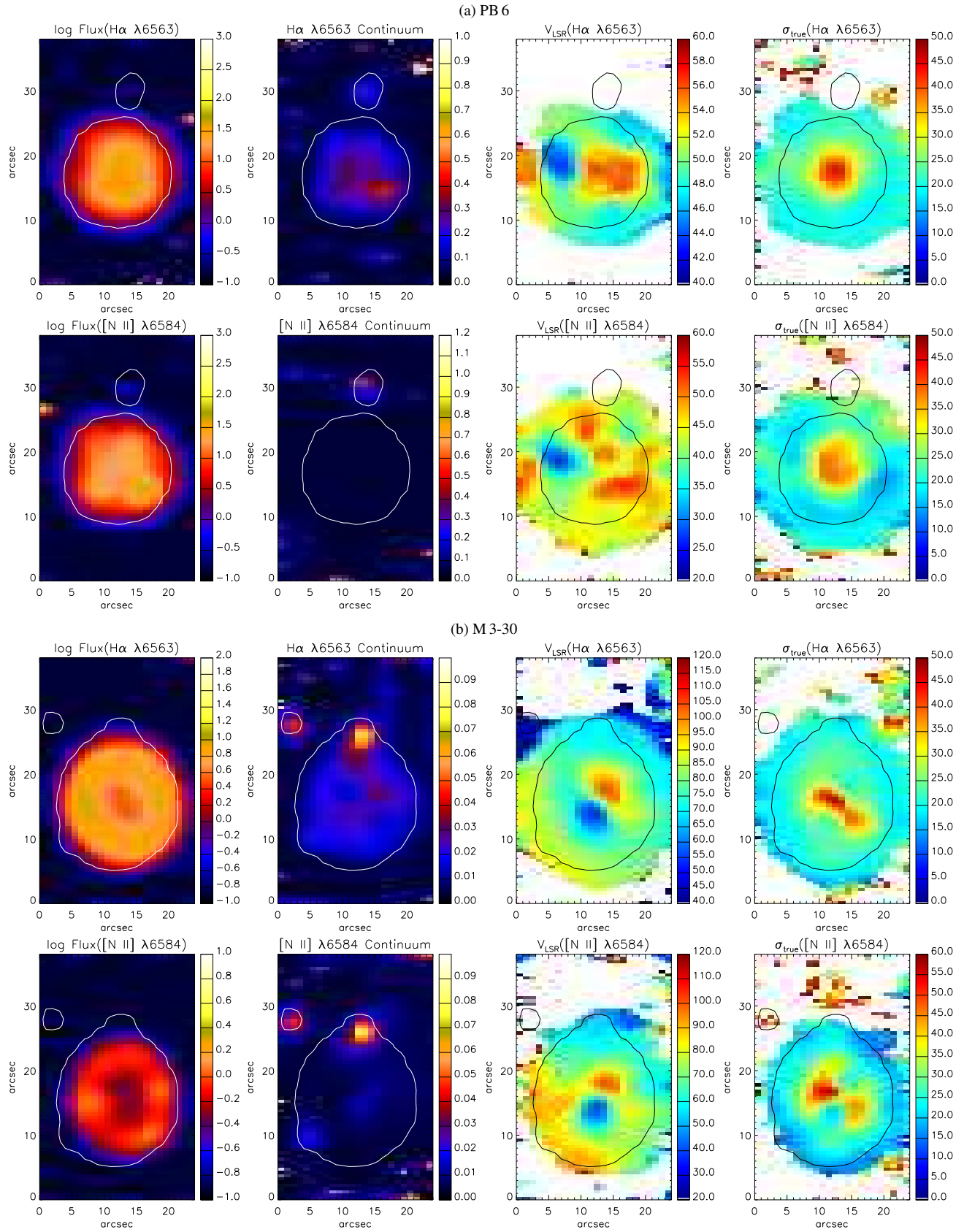


**Figure 1.** From left to right, the spatial distribution maps of logarithmic flux intensity, continuum, LSR velocity, and velocity dispersion of the  $H\alpha$   $\lambda 6563$  and  $[N II]$   $\lambda 6584$  emission lines for: (a) PB 6, (b) M 3-30, (c) Hb 4, (d) IC 1297, (e) Pe 1-1, (f) M 1-32, (g) M 3-15, (h) M 1-25, (i) Hen 2-142, (j) K 2-16, (k) NGC 6578, (l) NGC 6567, (m) NGC 6629, and (n) Sa 3-107. Fluxes are in logarithm of  $10^{-15} \text{ erg s}^{-1} \text{ cm}^{-2} \text{ spaxel}^{-1}$  unit, continua in  $10^{-15} \text{ erg s}^{-1} \text{ cm}^{-2} \text{ \AA}^{-1} \text{ spaxel}^{-1}$ , and LSR velocities and velocity dispersion in  $\text{km s}^{-1}$ . The white/black contour in each panel shows the narrow-band  $H\alpha$  emission in arbitrary unit retrieved from the SHS. North is up and east is toward the left-hand side.

Morpho-kinematic properties of WR planetary nebulae

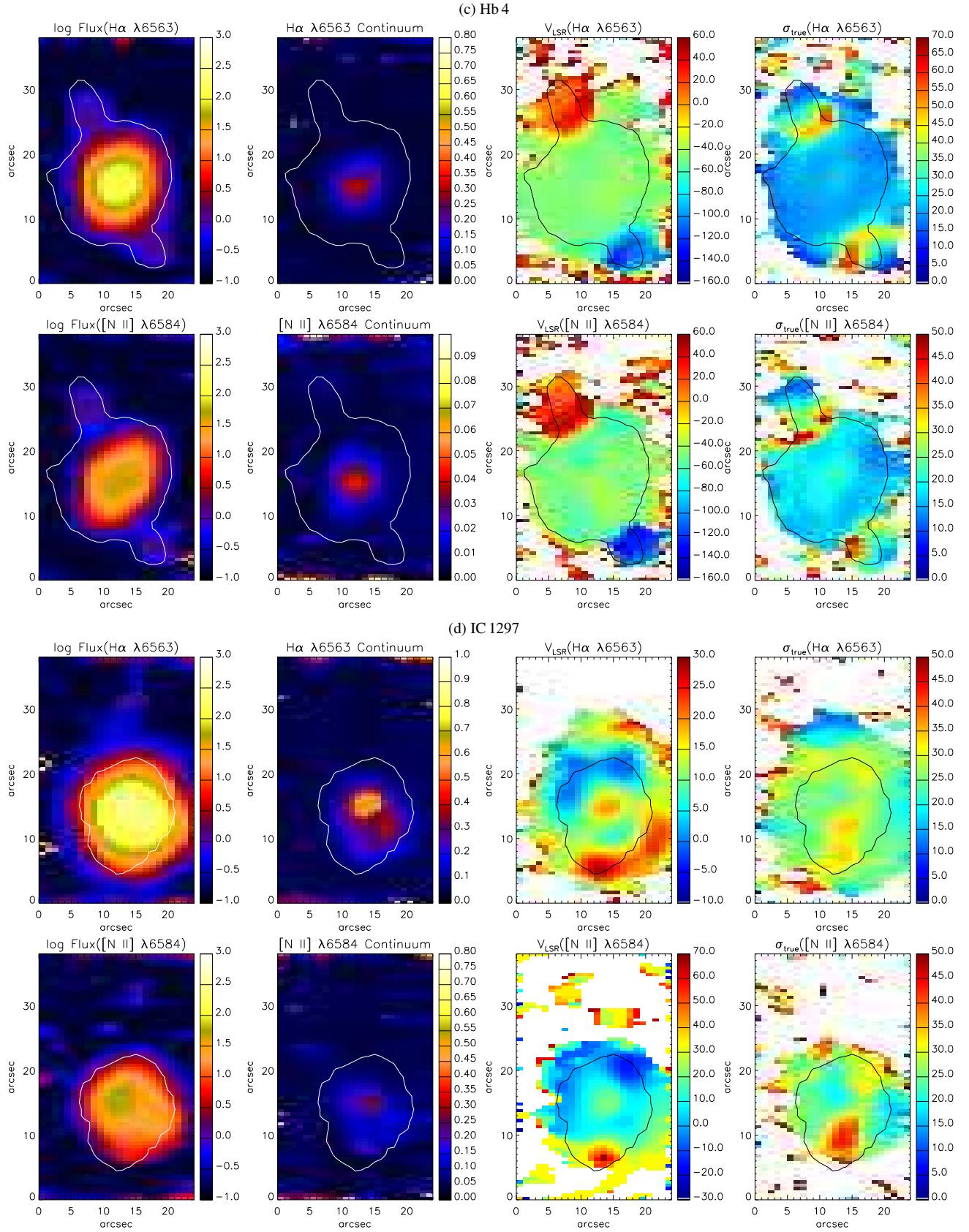
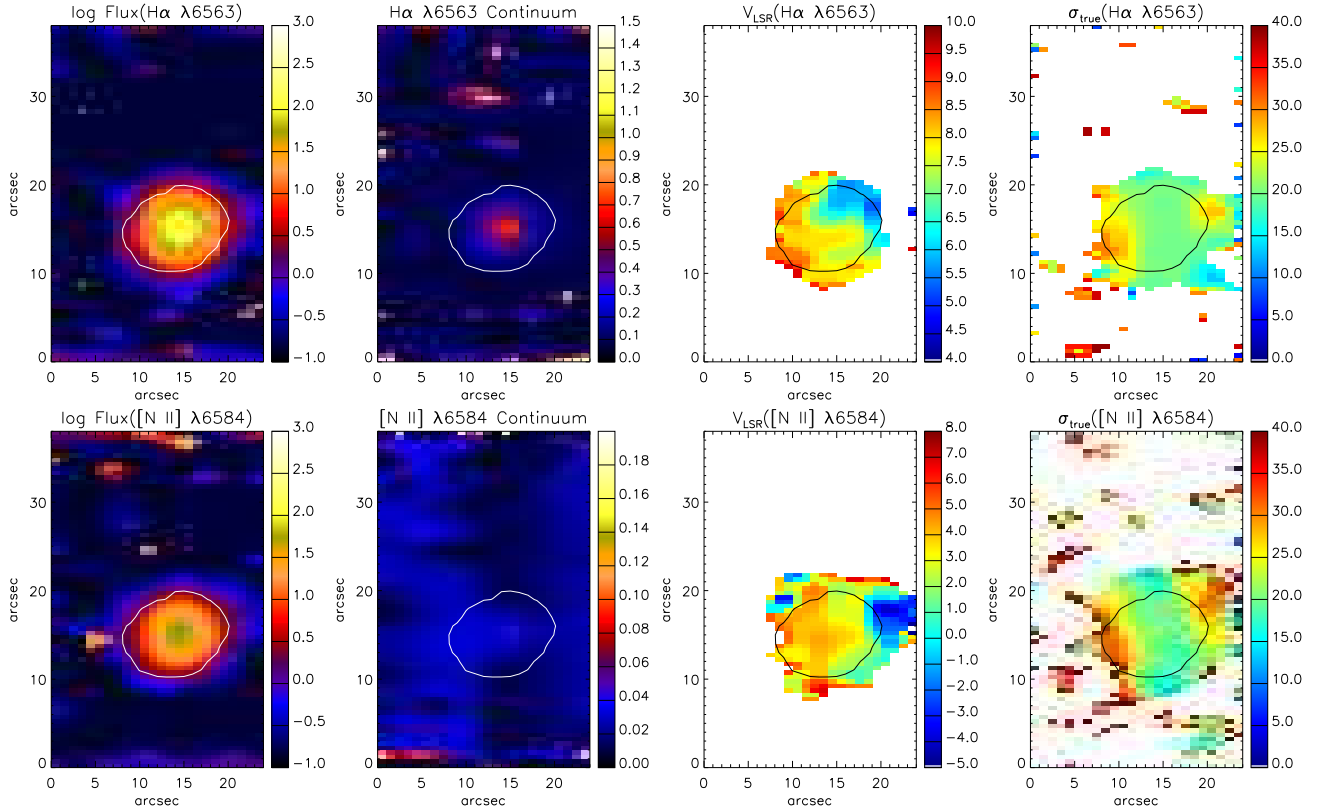


Figure 1. – continued

(e) Pe 1-1



(f) M 1-32

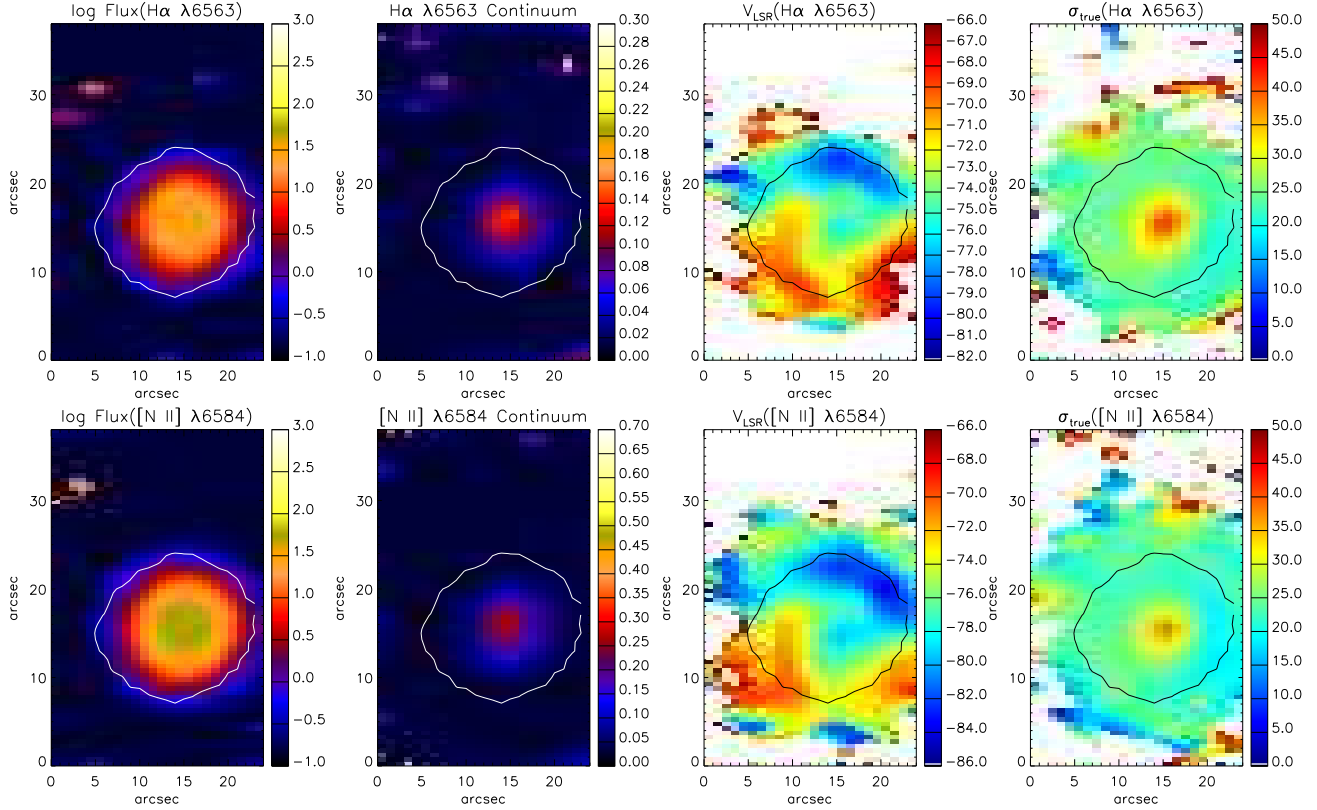


Figure 1. – continued

Morpho-kinematic properties of WR planetary nebulae

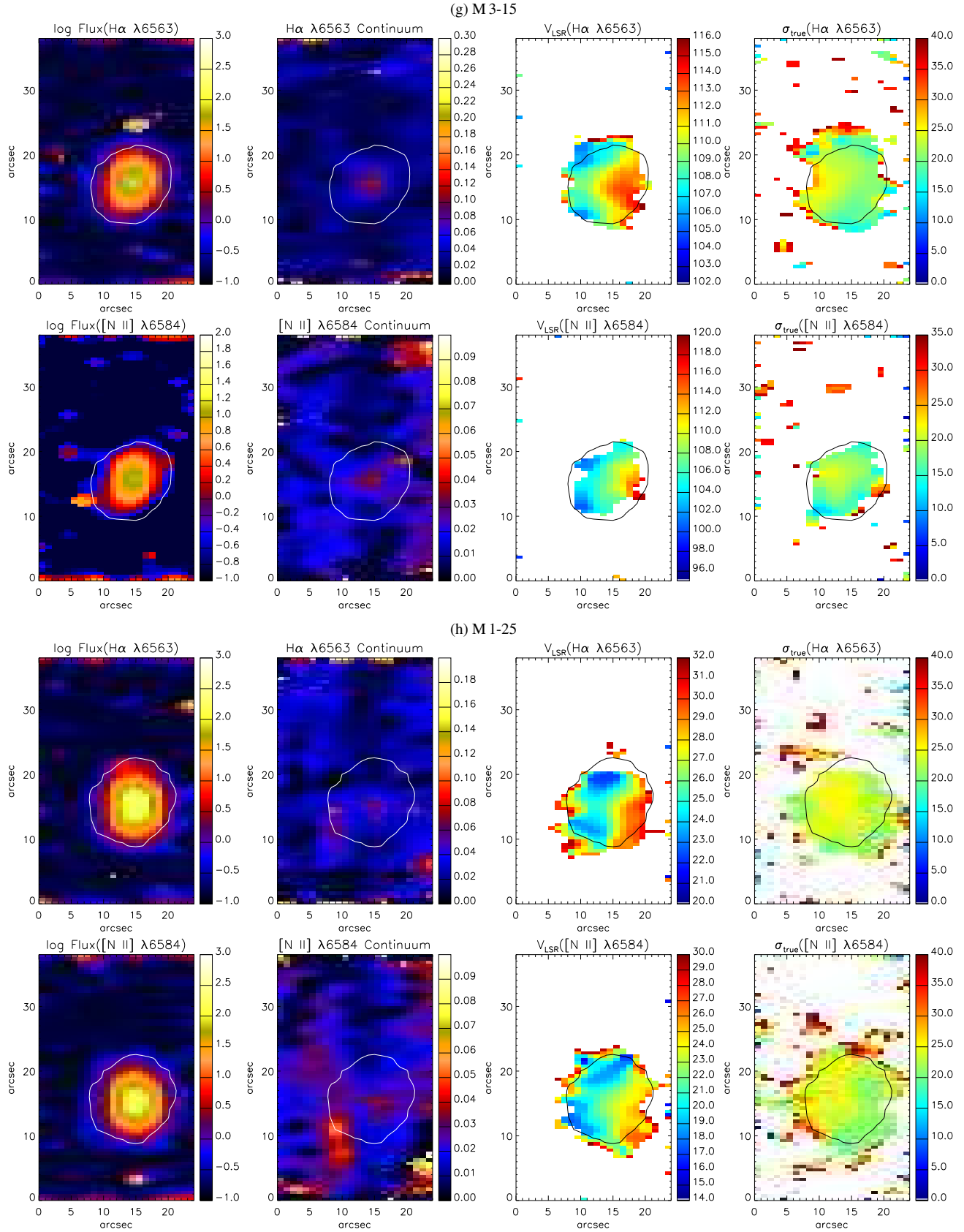
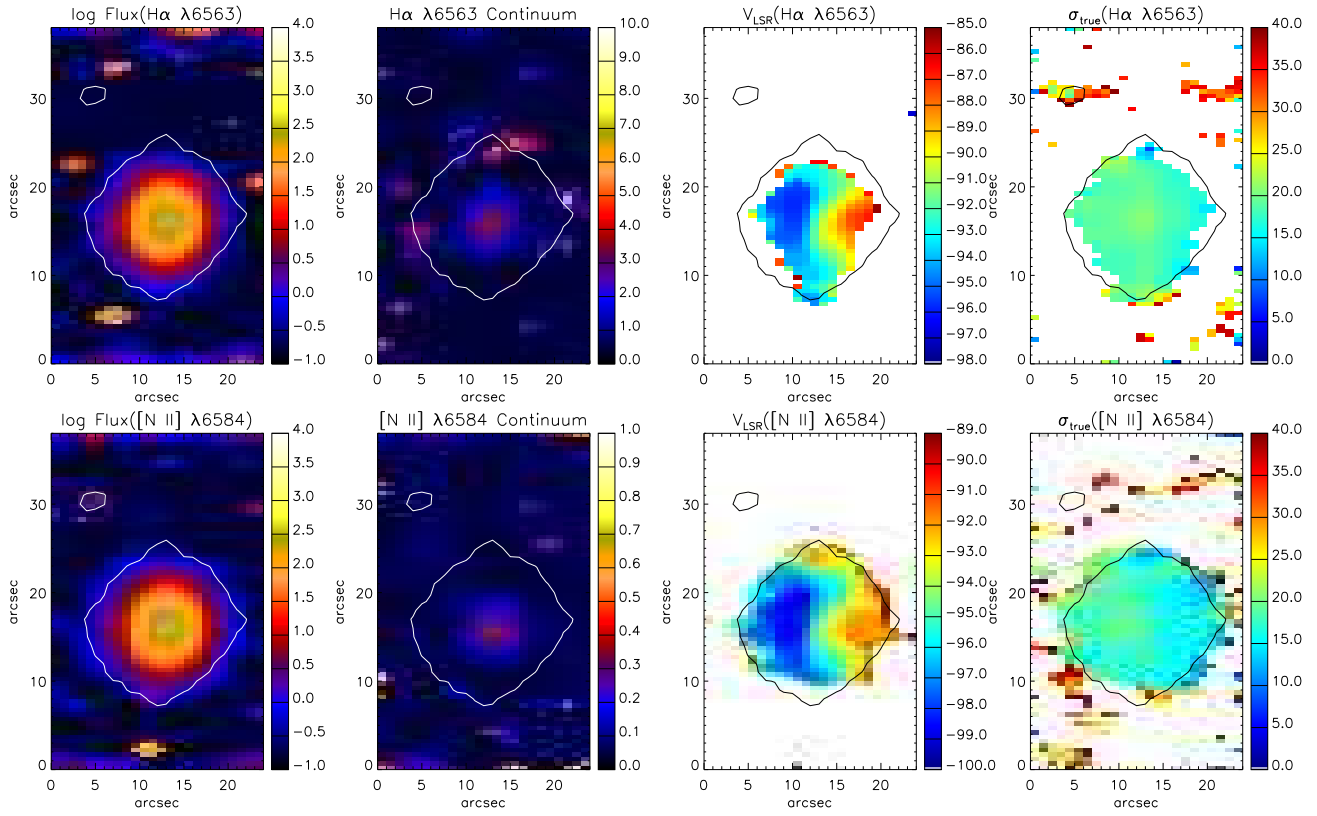


Figure 1. – continued

(i) Hen 2-142



(j) K 2-16

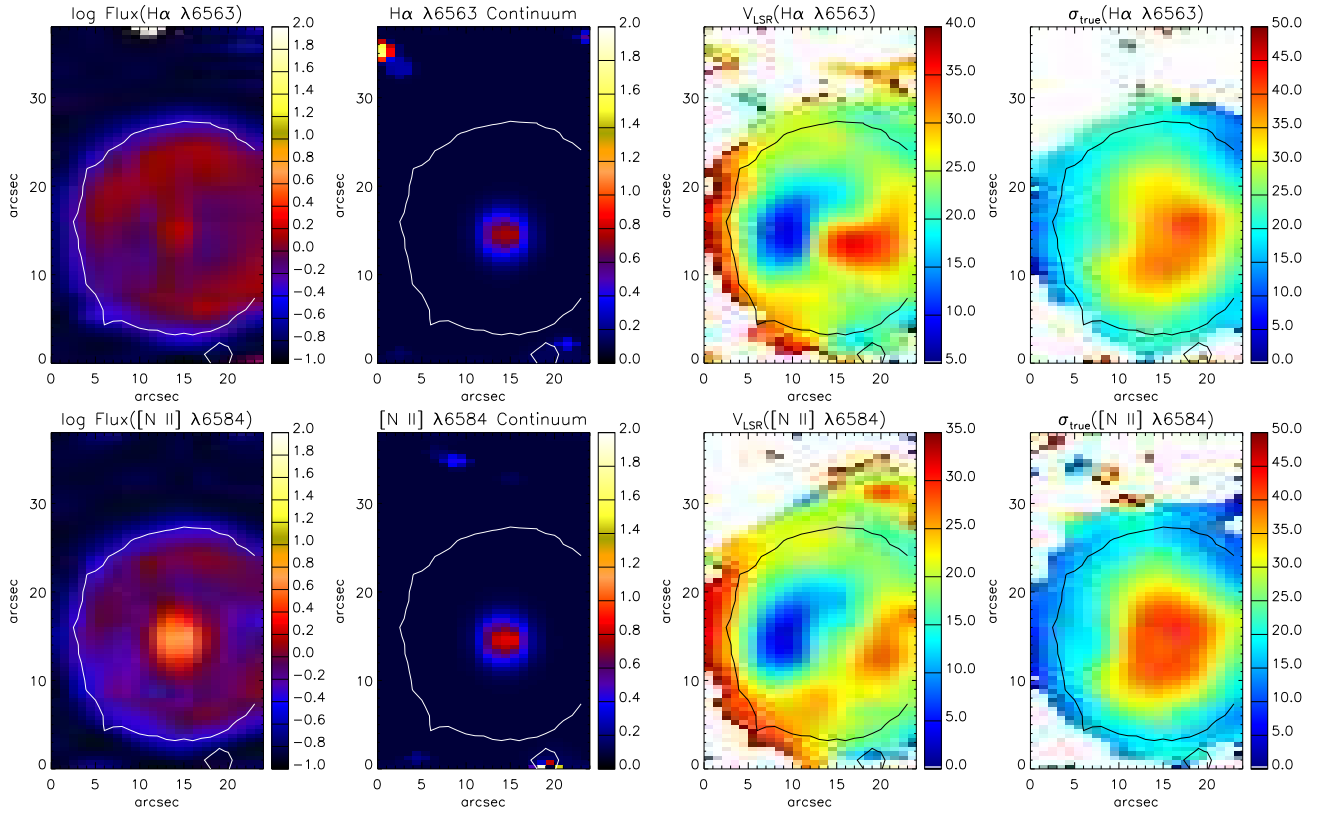


Figure 1. – continued

Morpho-kinematic properties of WR planetary nebulae

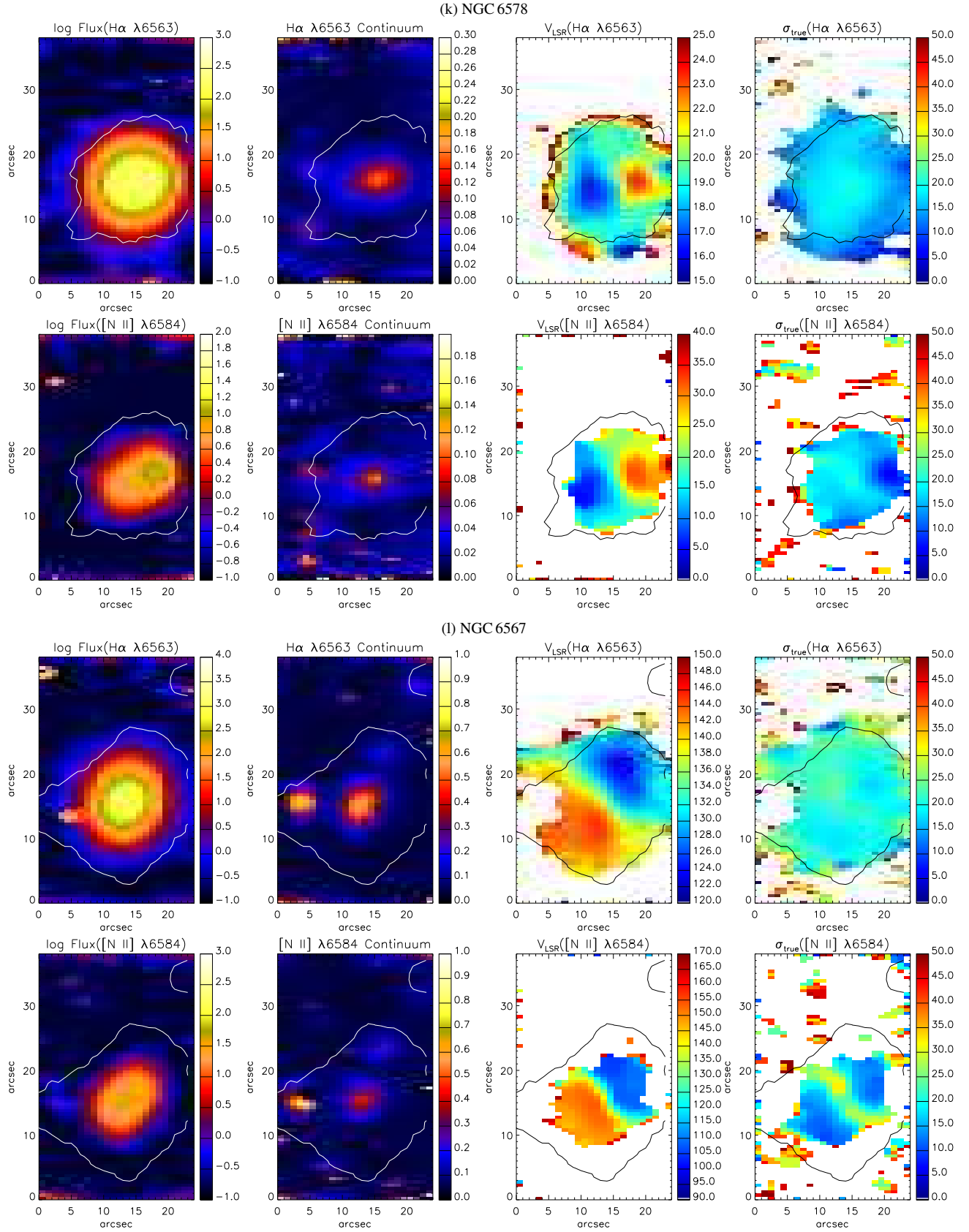
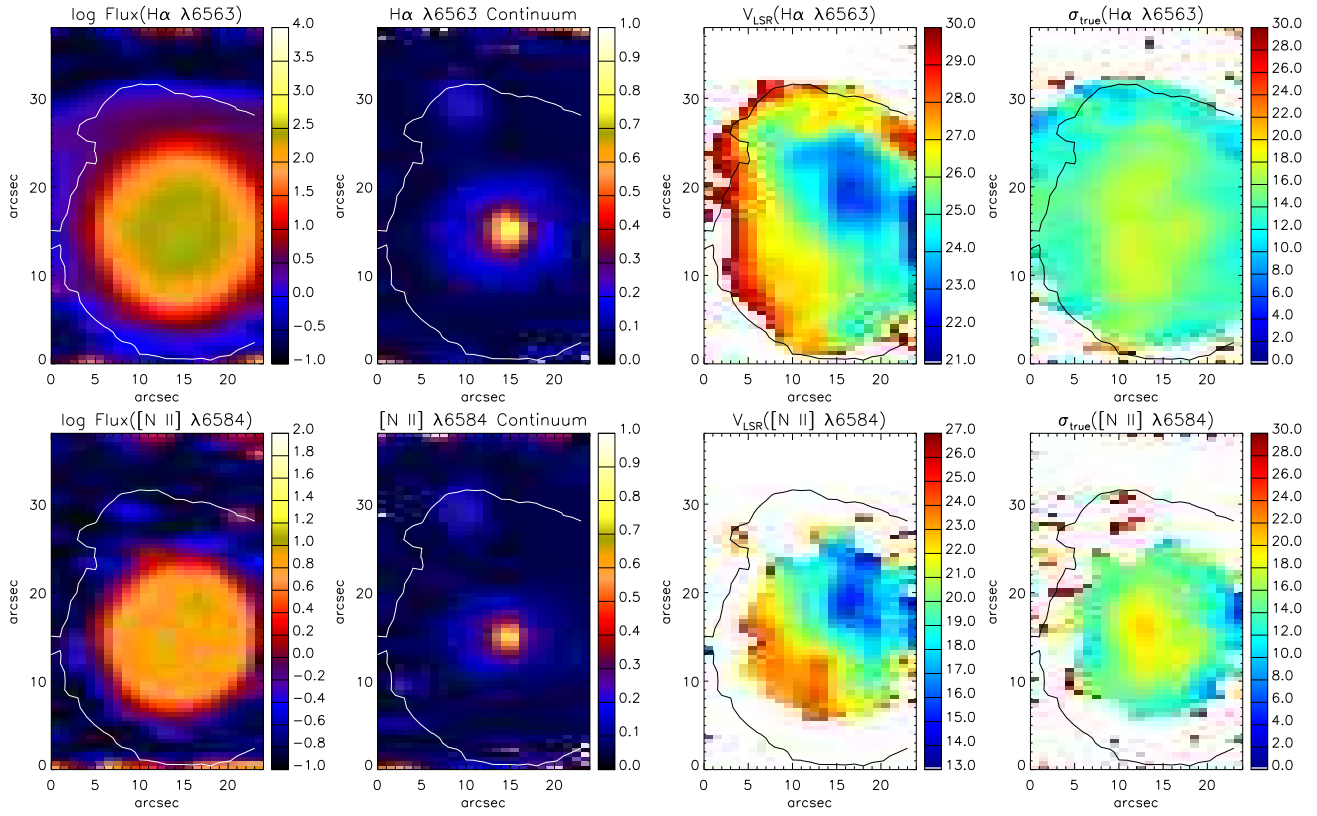


Figure 1. – continued

(m) NGC 6629



(n) Sa3-107

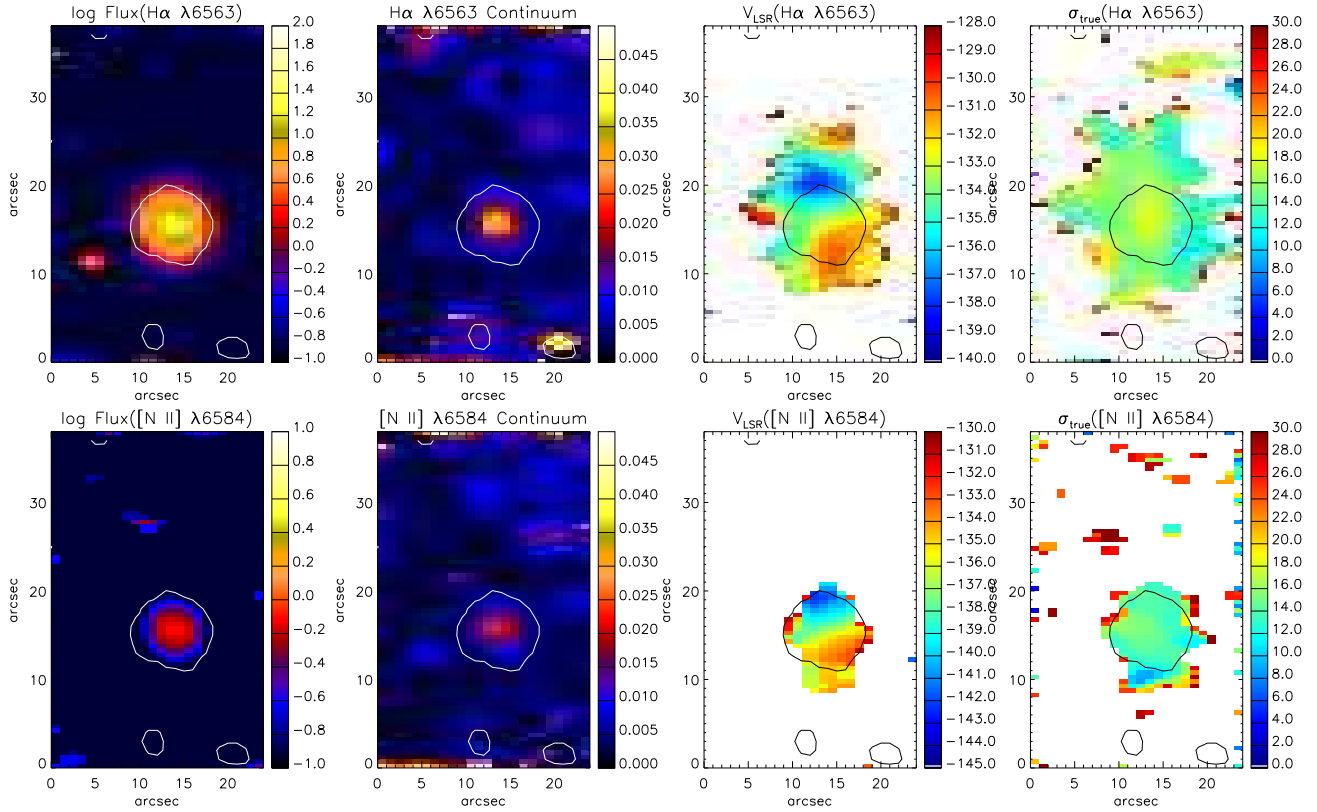
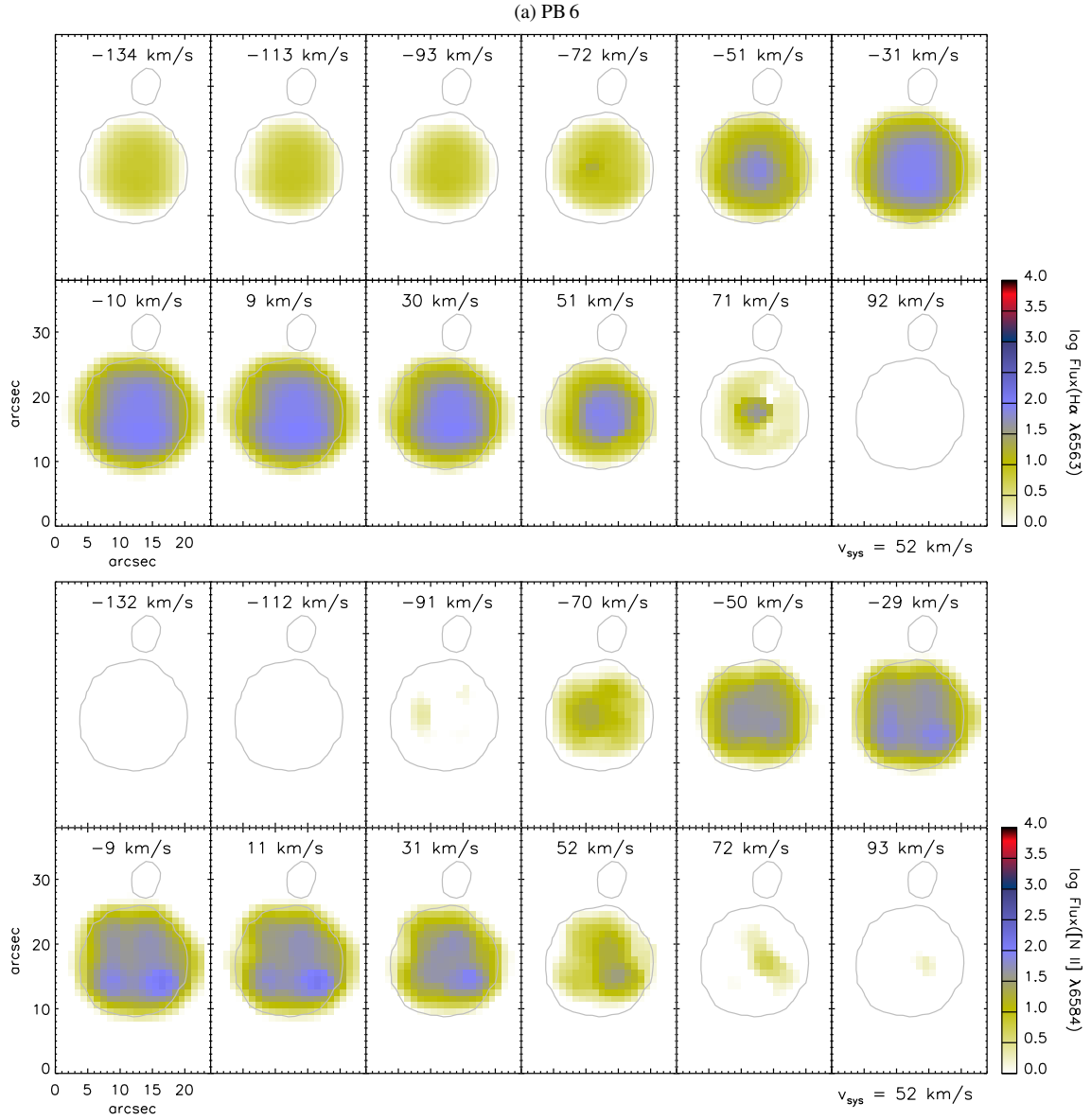


Figure 1. – continued



**Figure 2.** Velocity slices along the  $\text{H}\alpha$   $\lambda 6563$  and  $[\text{N II}]$   $\lambda 6584$  emission-line profiles for: (a) PB 6, (b) M 3-30, (c) Hb 4, (d) IC 1297, (e) Pe 1-1, (f) M 1-32, (g) M 3-15, (h) M 1-25, (i) Hen 2-142, (j) K 2-16, (k) NGC 6578, (l) NGC 6567, (m) NGC 6629, and (n) Sa 3-107. Each slice has a  $\sim 21 \text{ km s}^{-1}$  width, whose central velocity is given in  $\text{km s}^{-1}$  unit at the top of the panel. The LSR systemic velocity ( $v_{\text{sys}}$ ) of each object is given in  $\text{km s}^{-1}$  unit in the right bottom corner. The flux color is in logarithm of  $10^{-15} \text{ erg s}^{-1} \text{ cm}^{-2} \text{ spaxel}^{-1}$  unit. The contour in each panel shows the narrow-band  $\text{H}\alpha$  emission in arbitrary unit retrieved from the SHS. North is up and east is toward the left-hand side.

(b) M 3-30

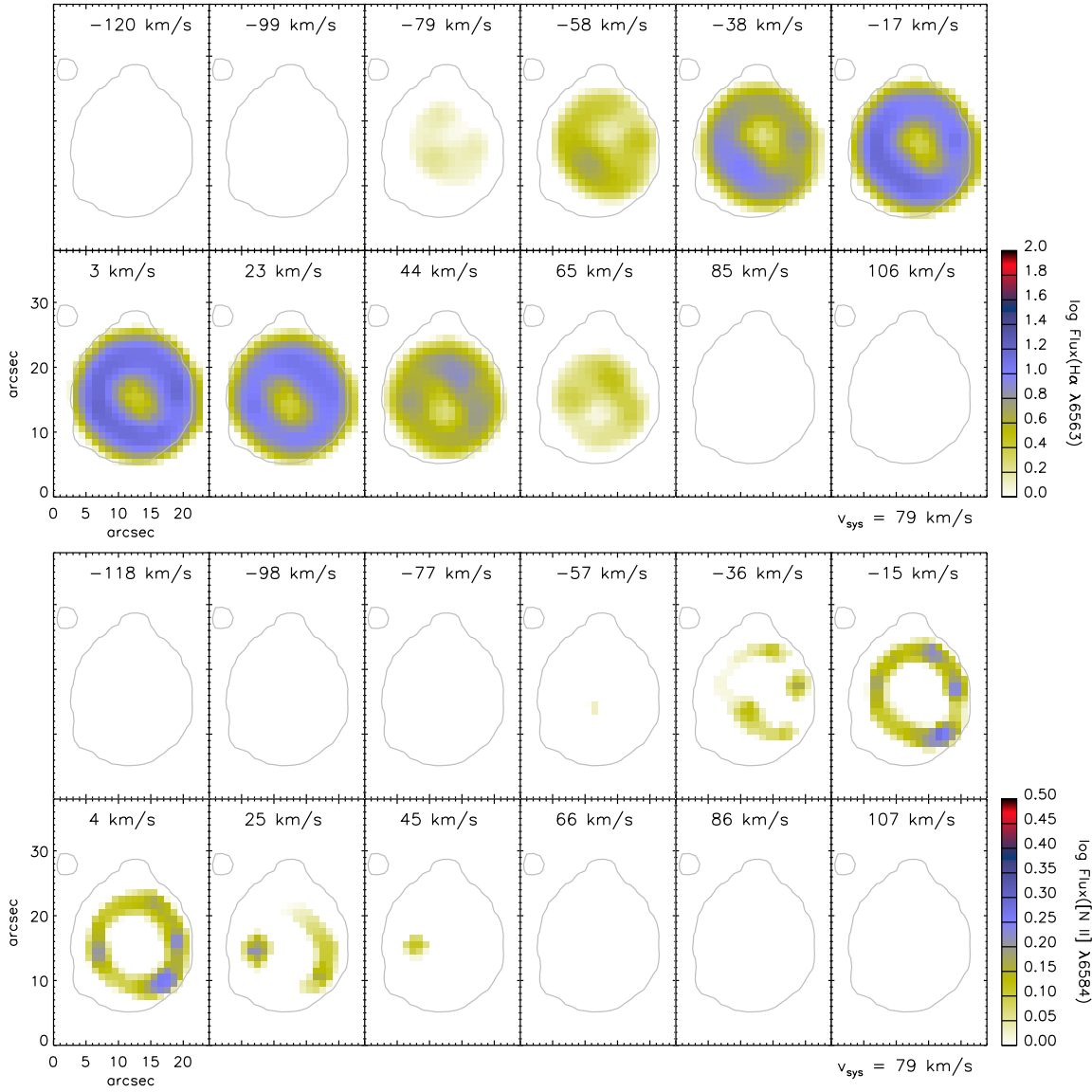


Figure 2. – continued

Morpho-kinematic properties of WR planetary nebulae

(c) Hb 4

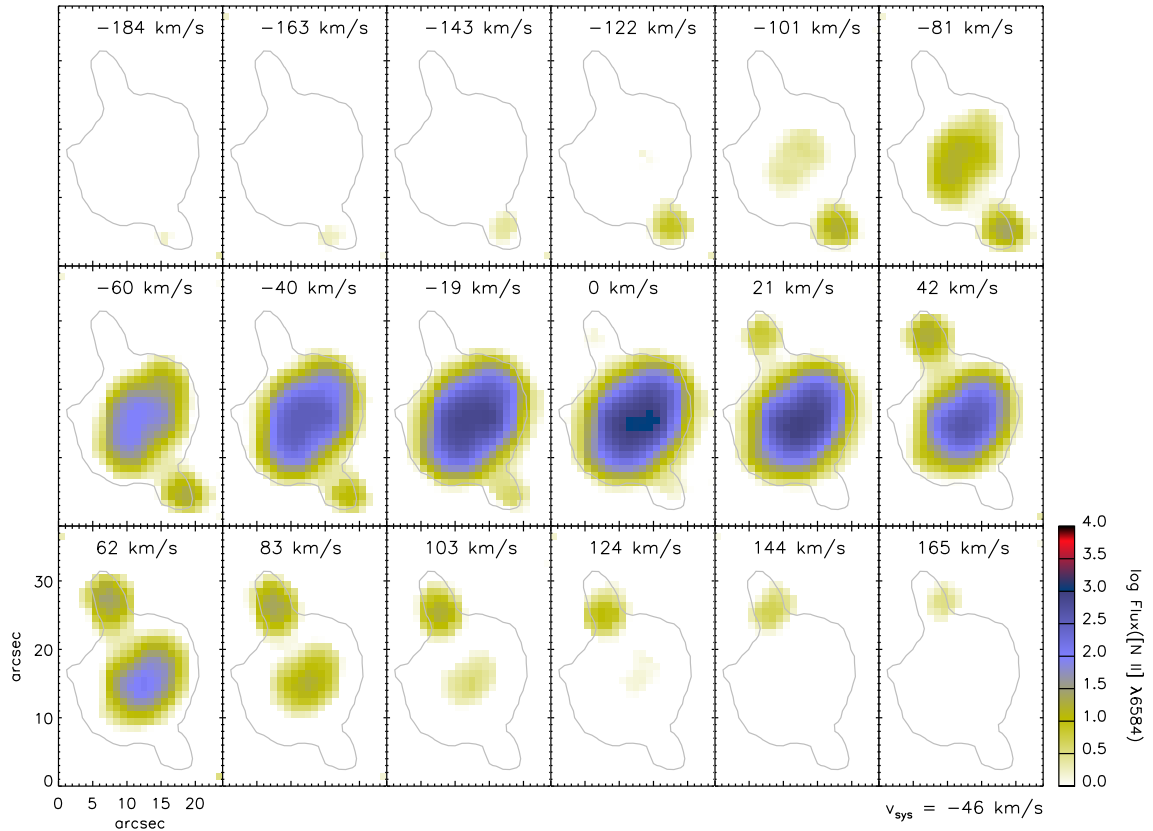
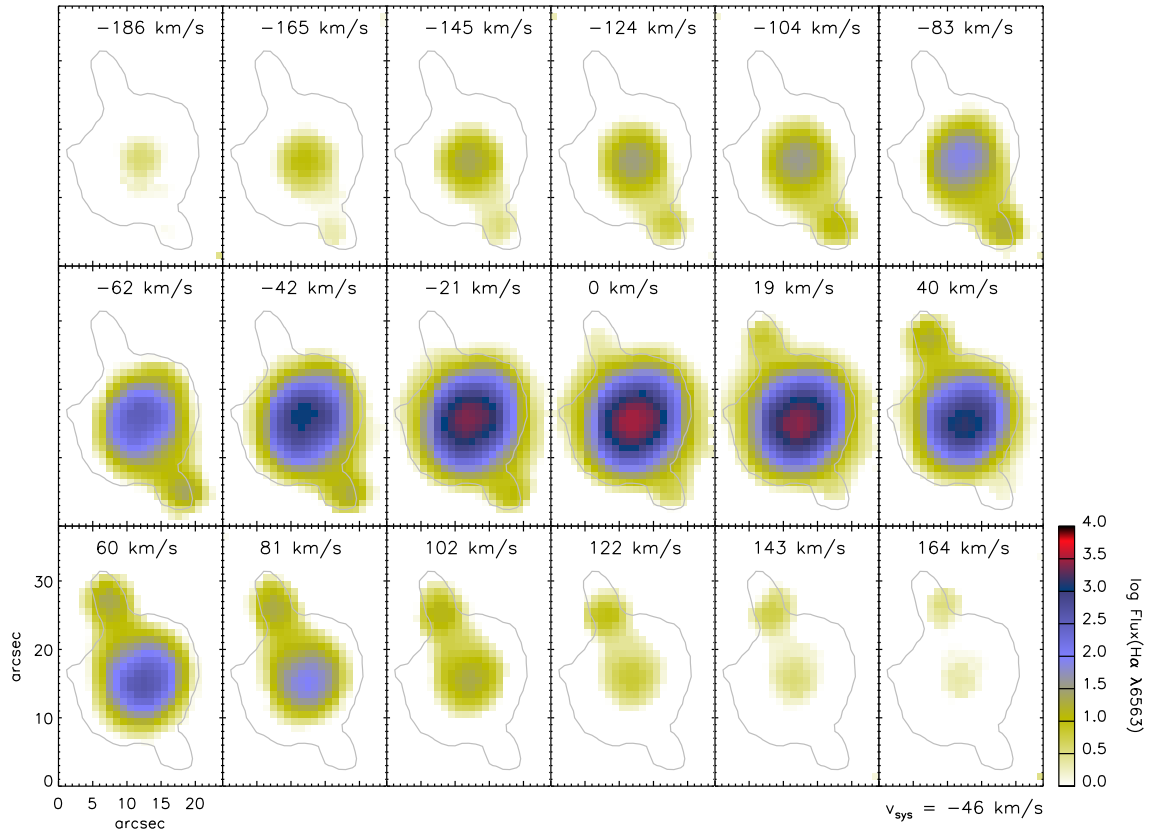


Figure 2. – continued

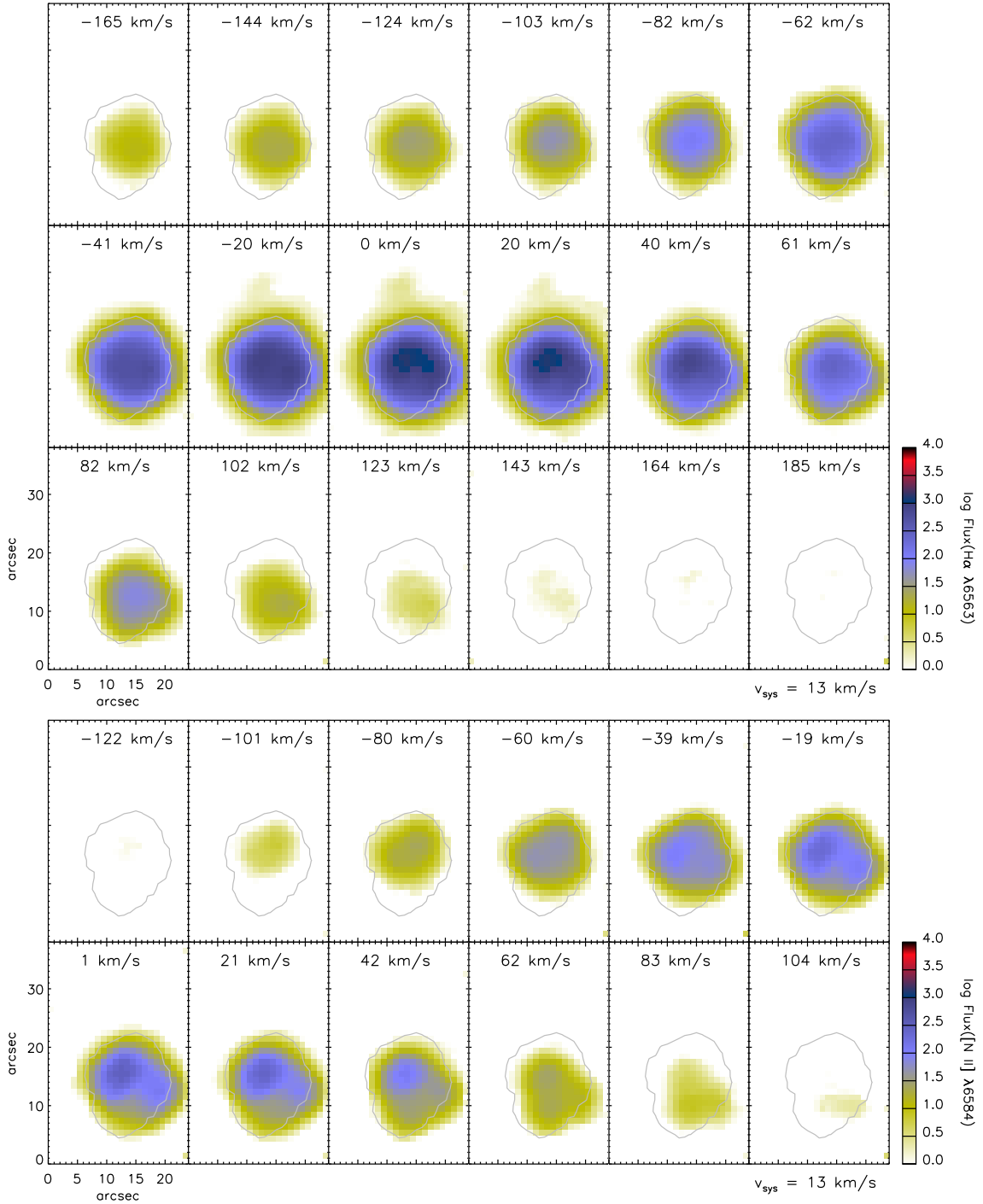


Figure 2. – continued

Morpho-kinematic properties of WR planetary nebulae

(e) Pe 1-1

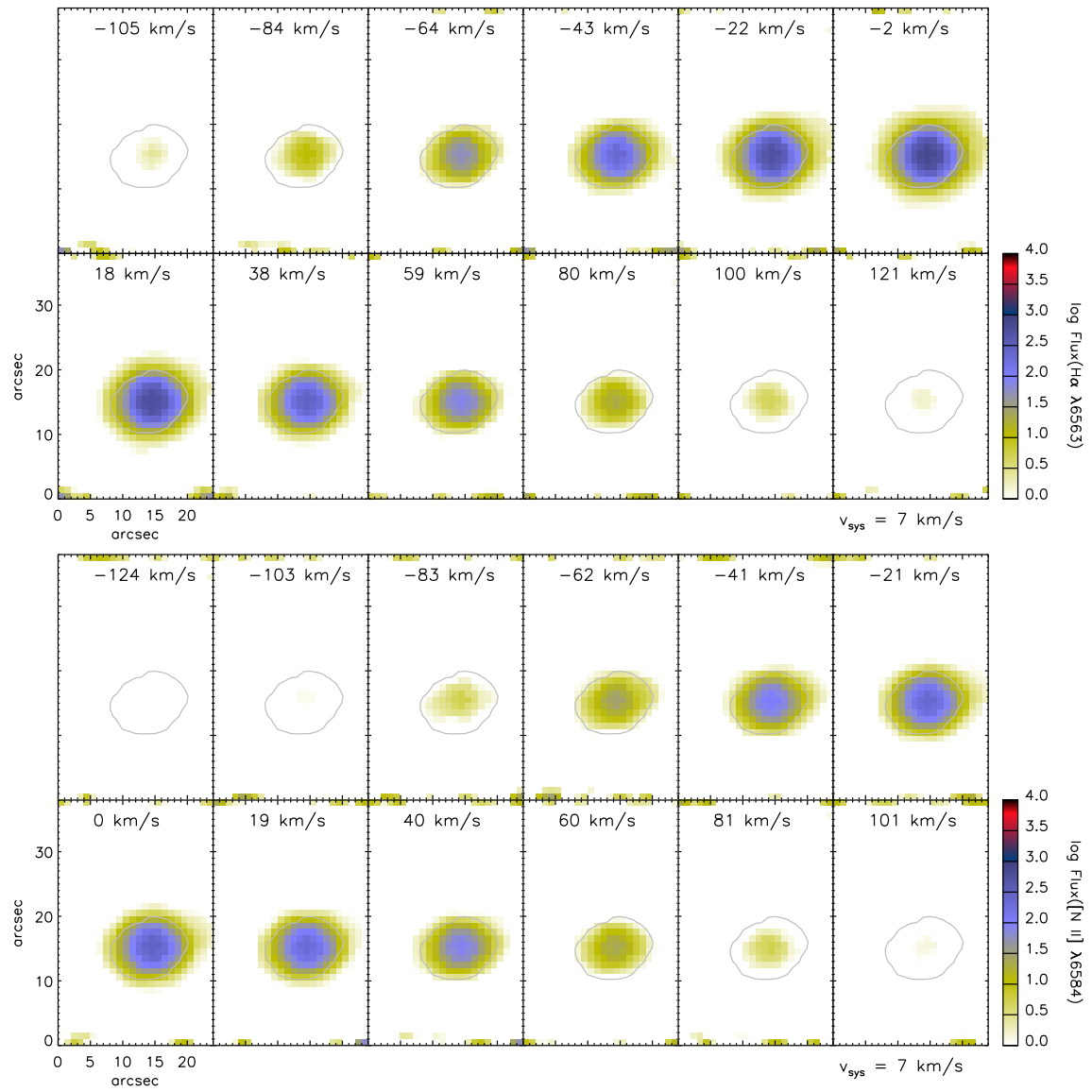
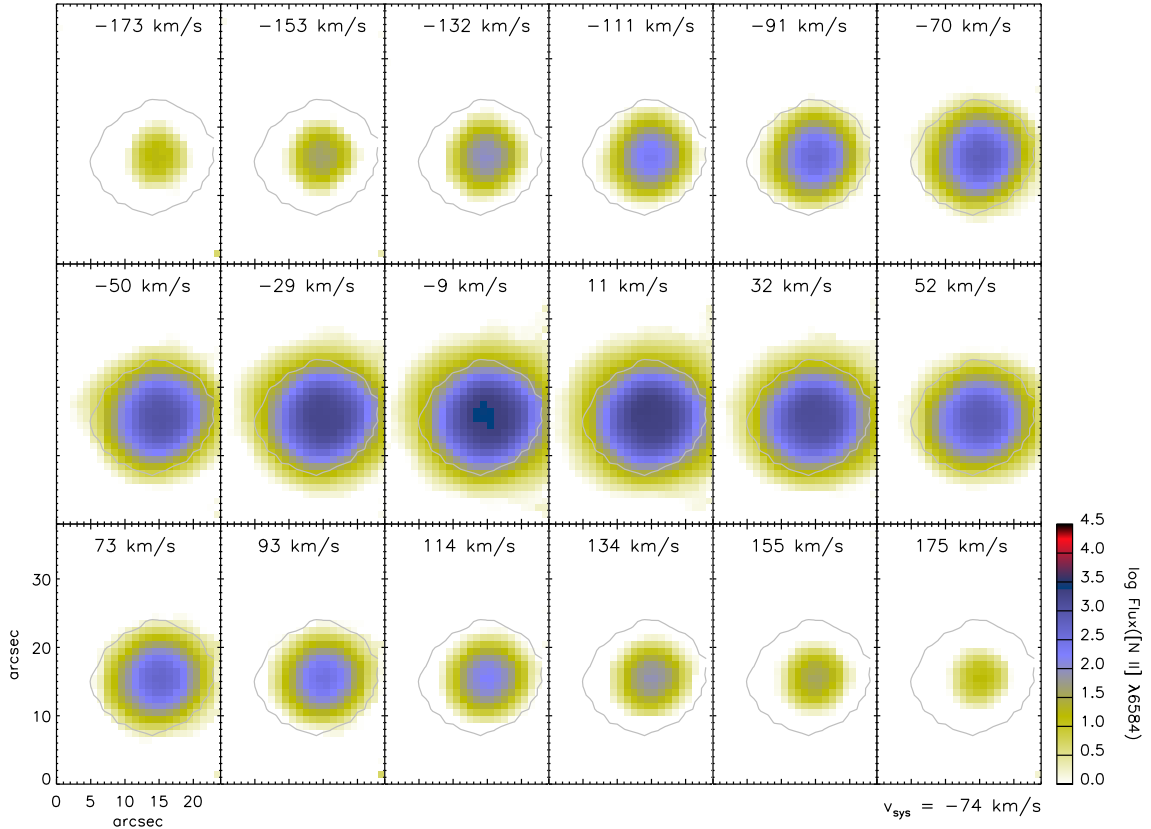
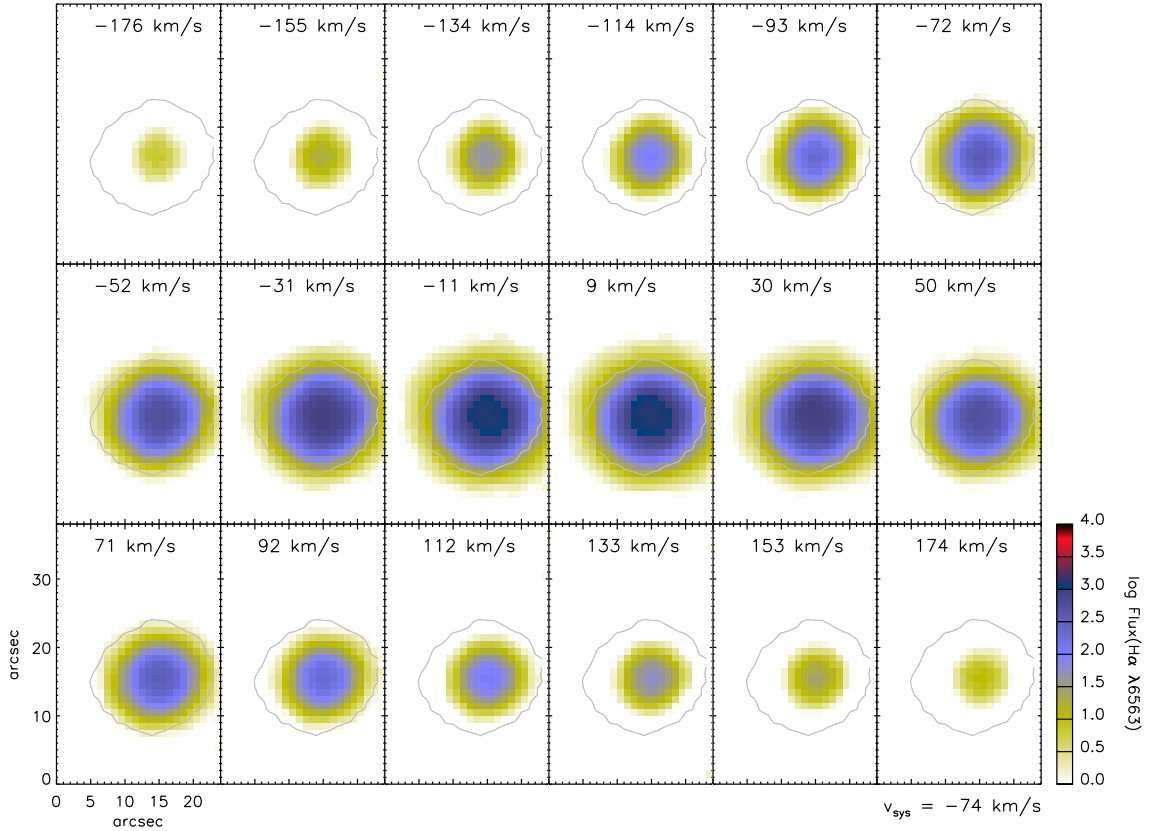


Figure 2. – continued

(f) M 1-32



Morpho-kinematic properties of WR planetary nebulae

(g) M 3-15

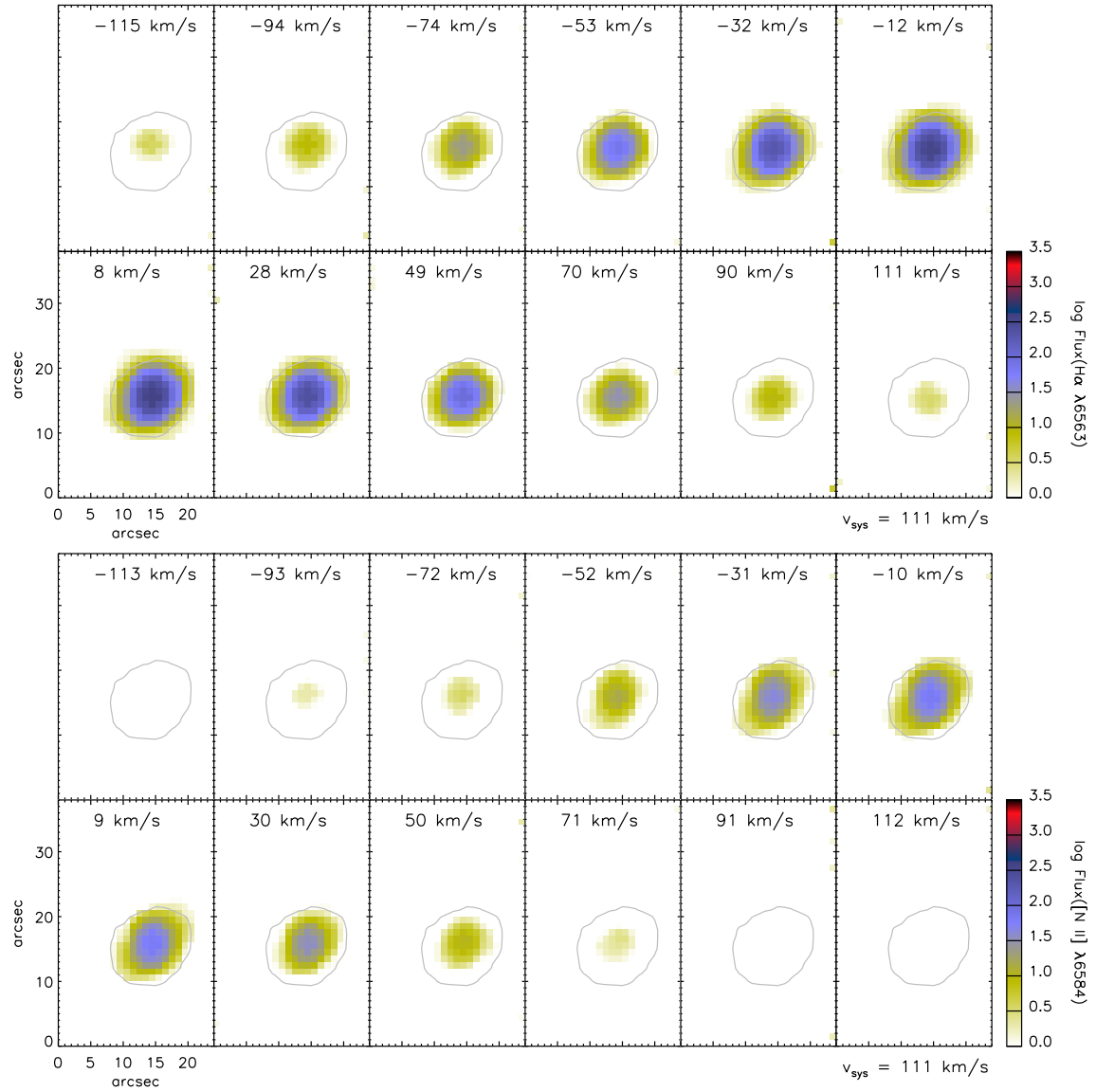
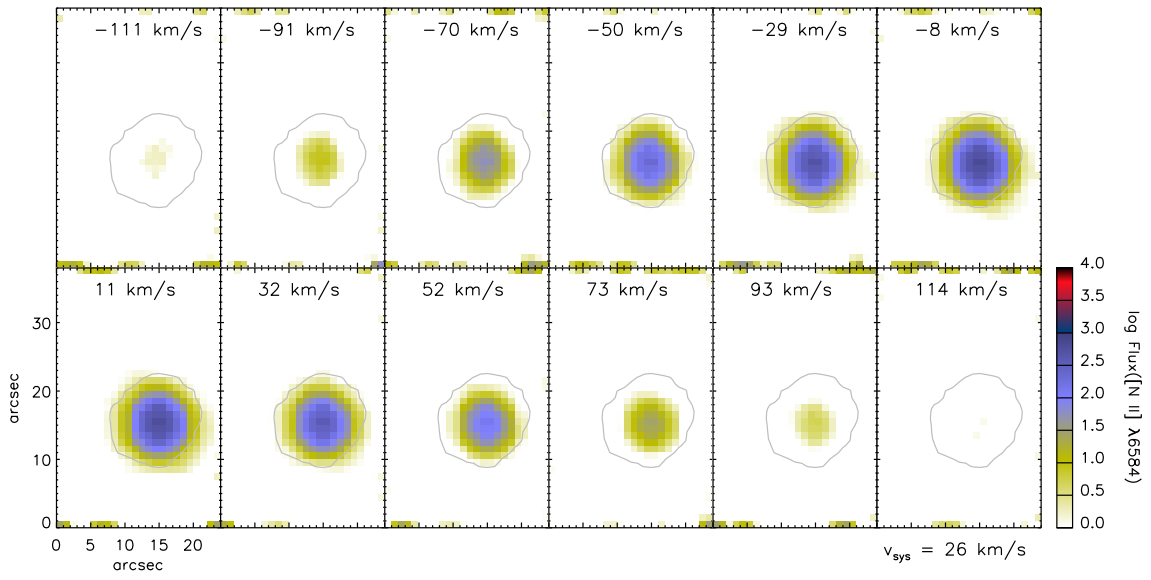
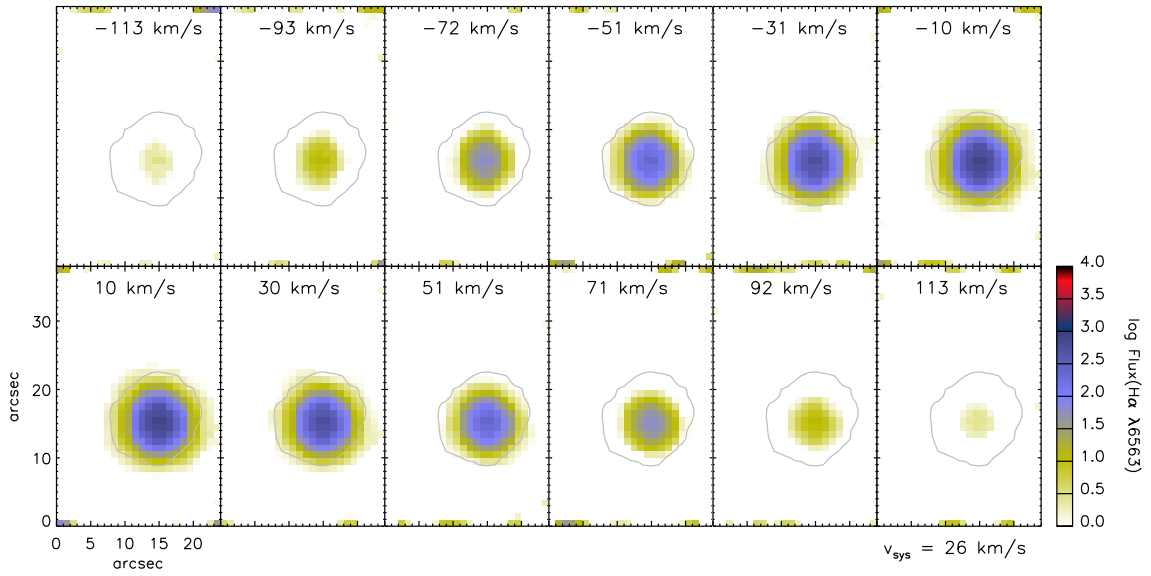


Figure 2. – continued



(i) Hen 2-142

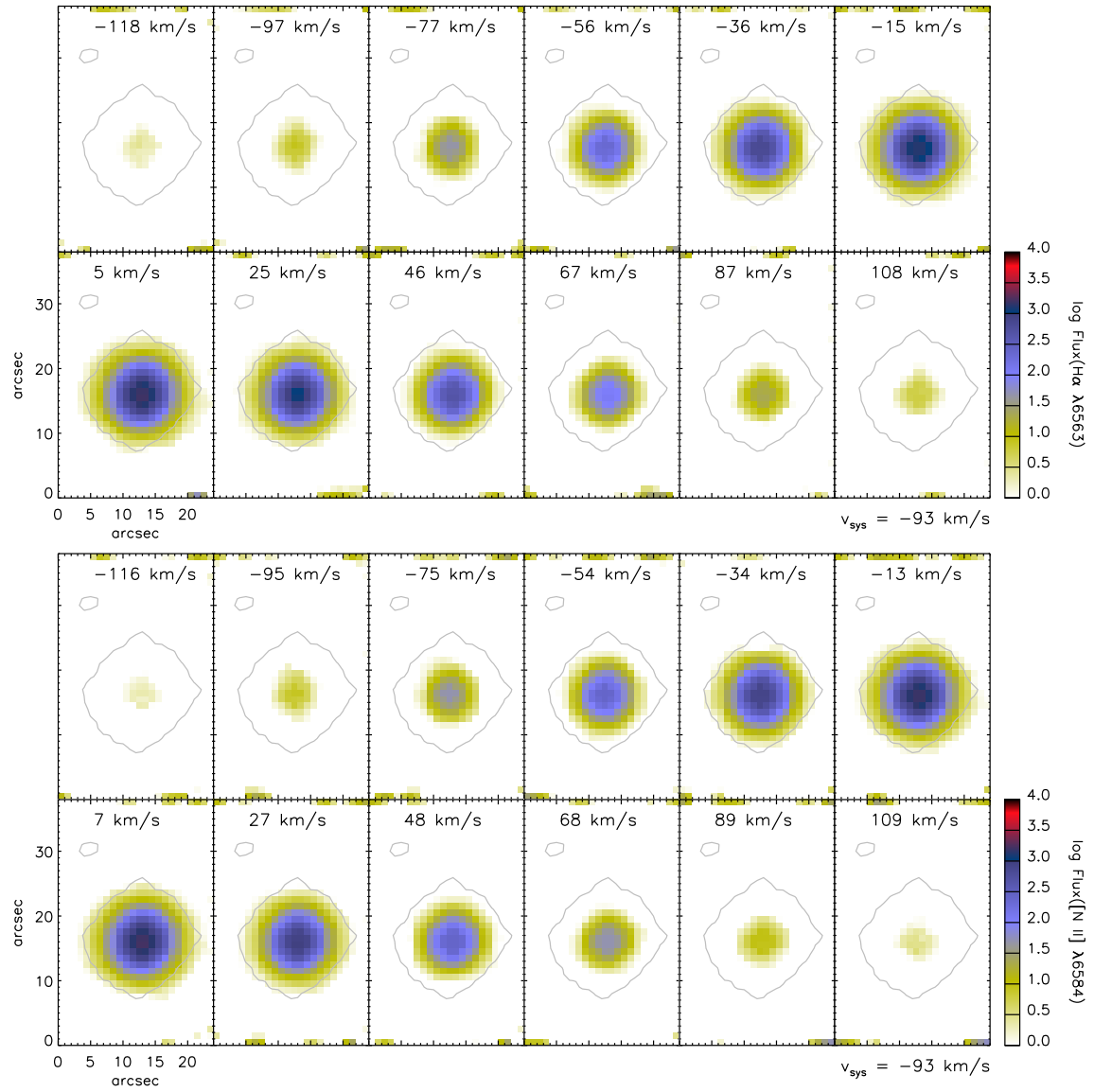


Figure 2. – continued

(j) K2-16

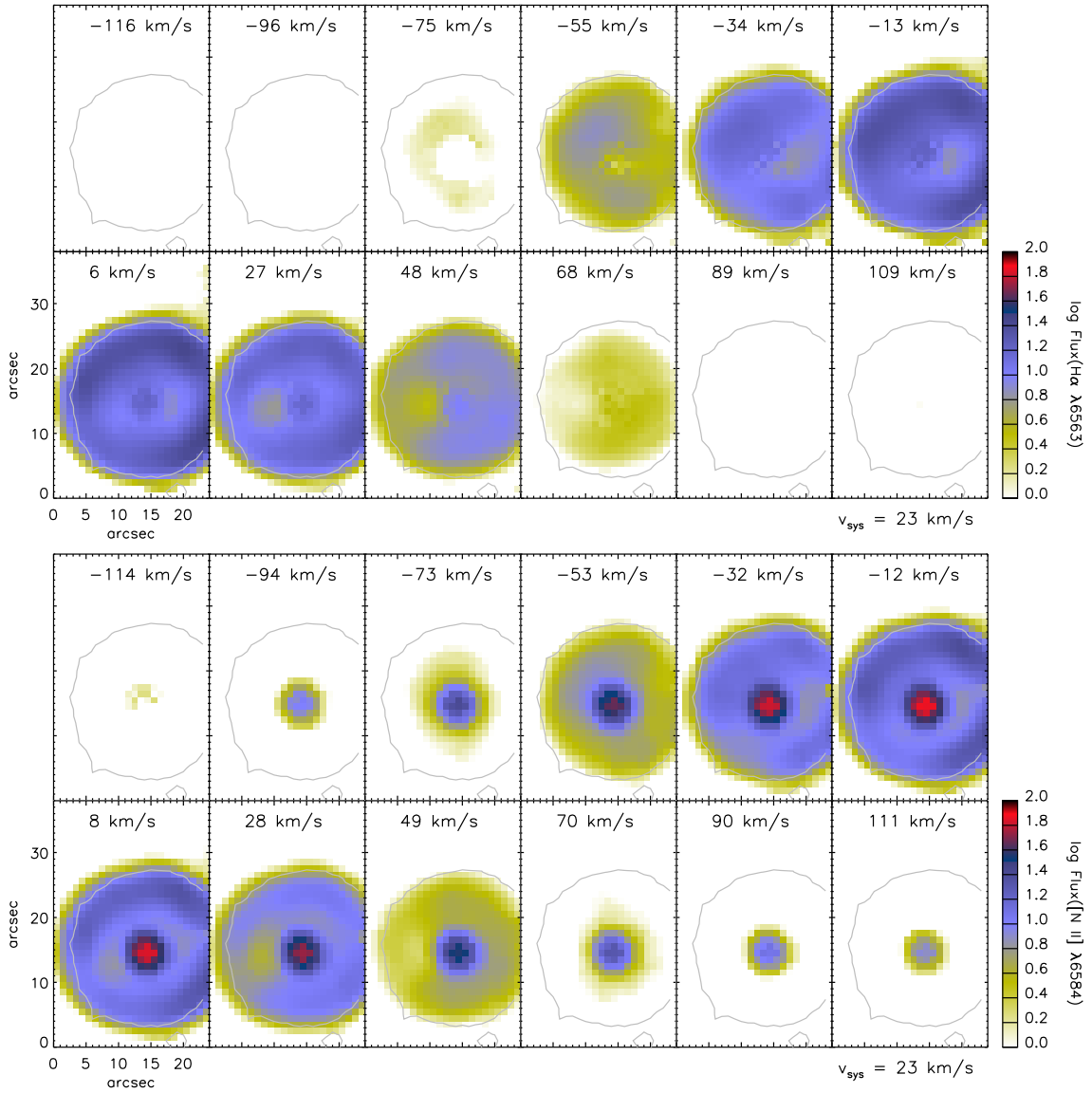


Figure 2. – continued

(k) NGC 6578

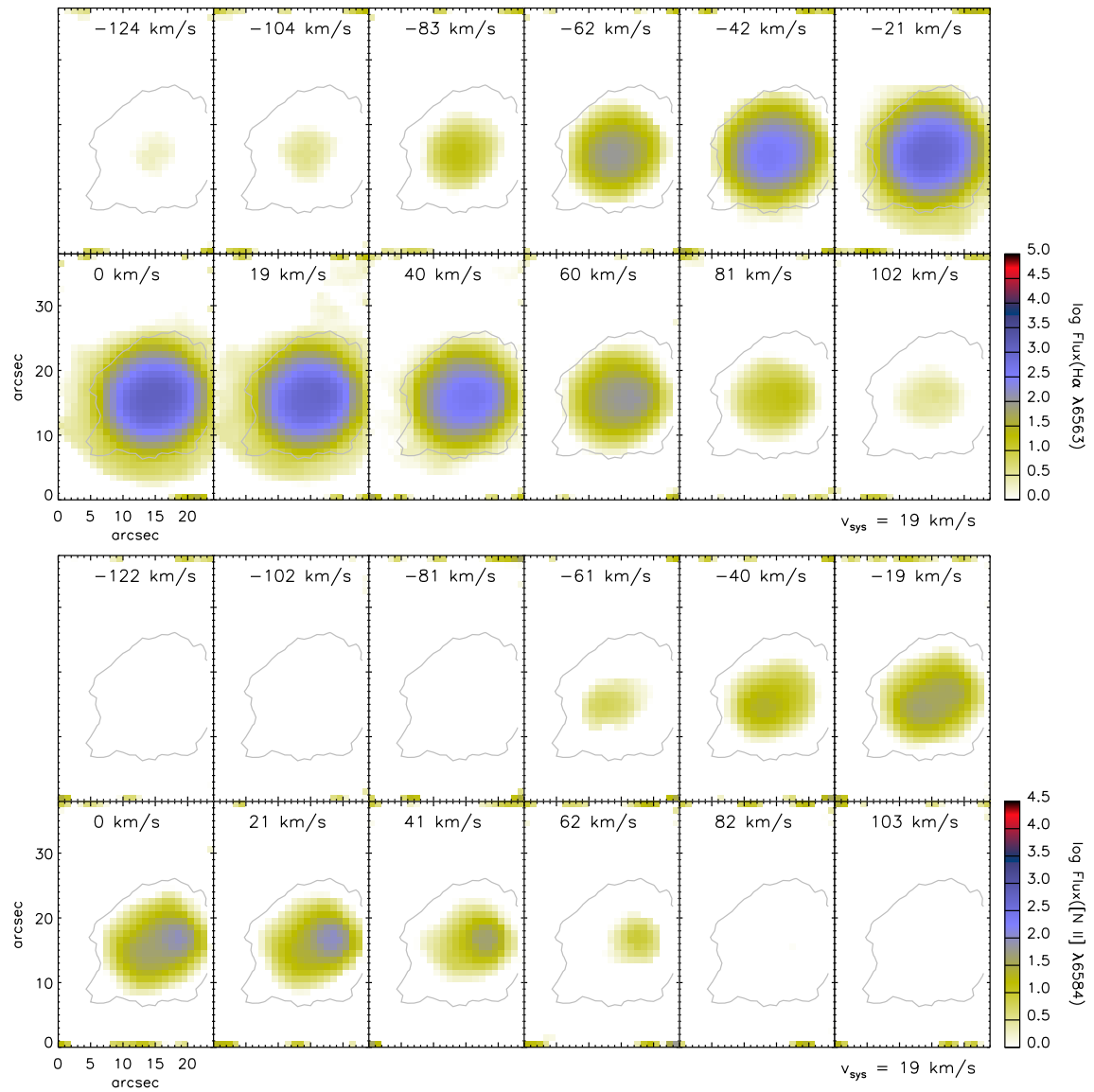


Figure 2. – continued

(l) NGC 6567

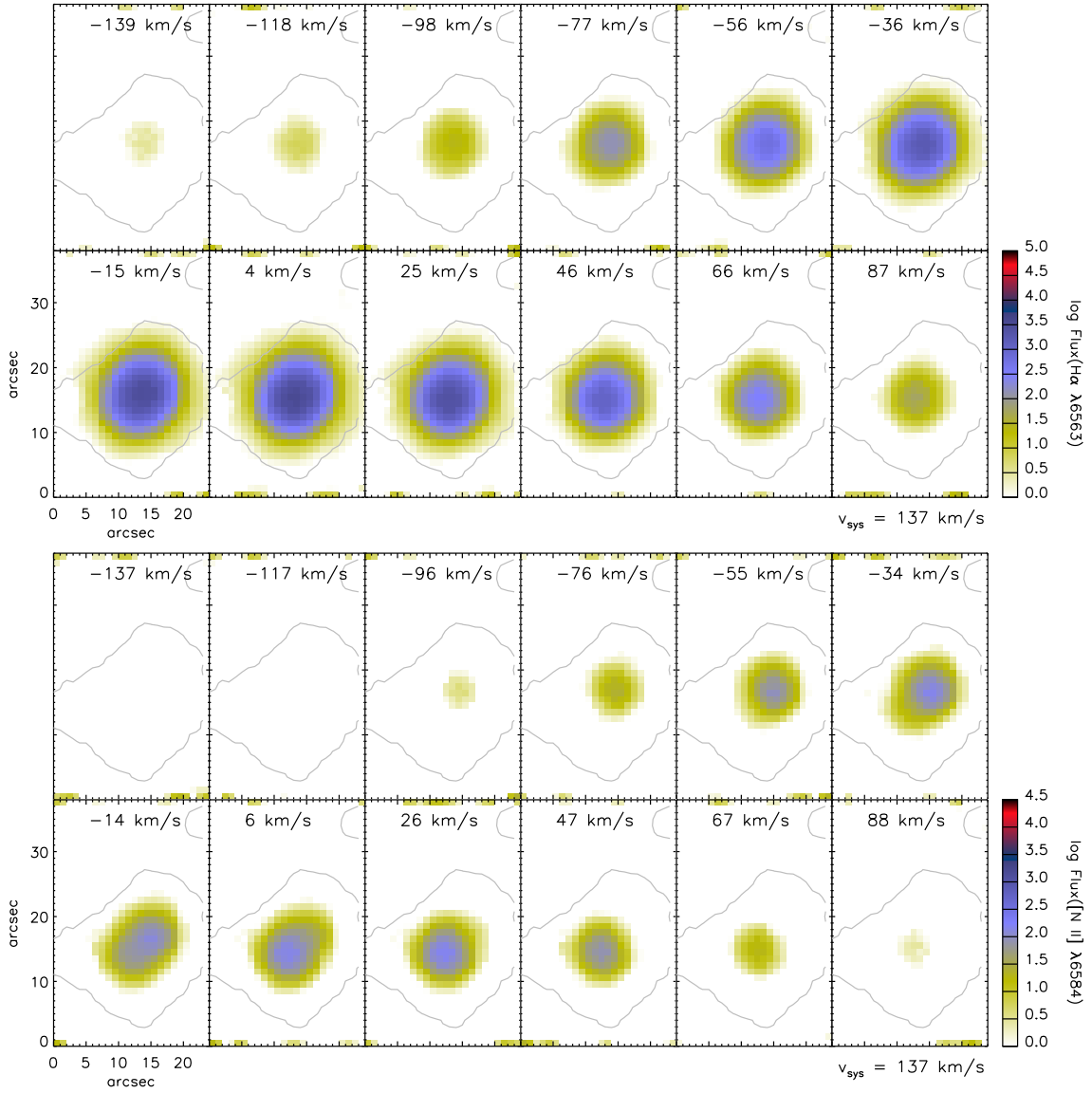


Figure 2. – continued

(m) NGC 6629

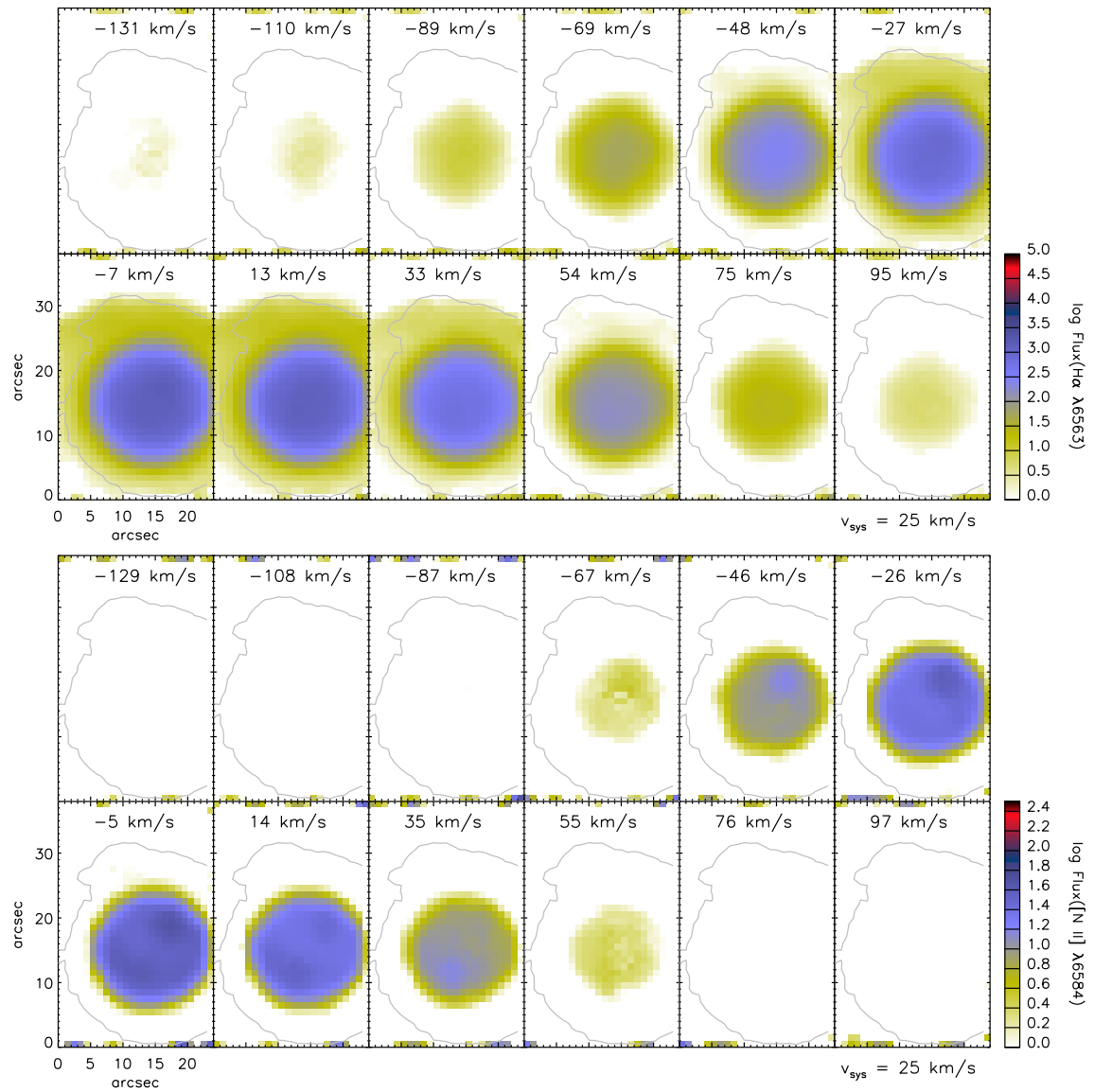


Figure 2. – continued

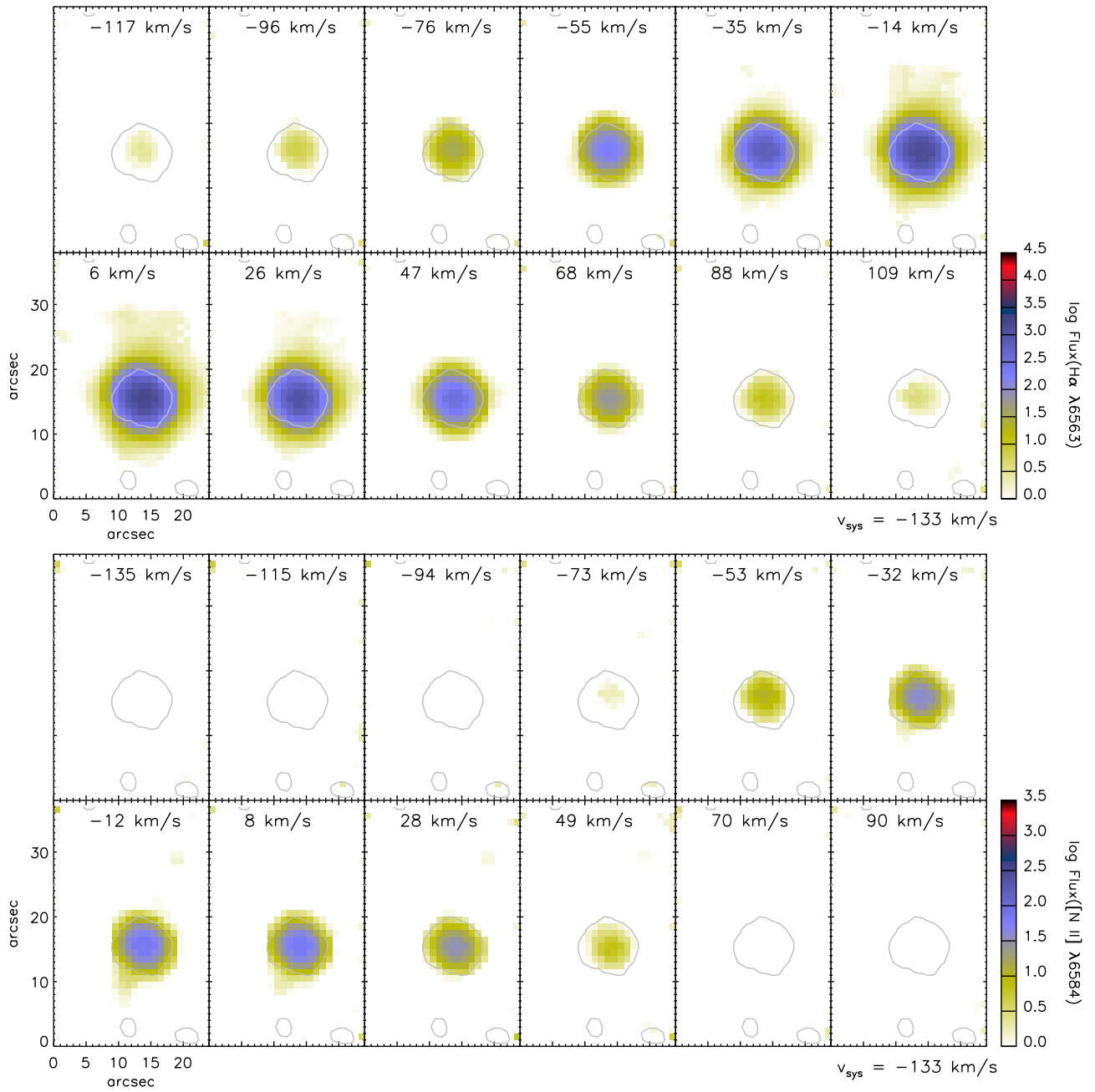
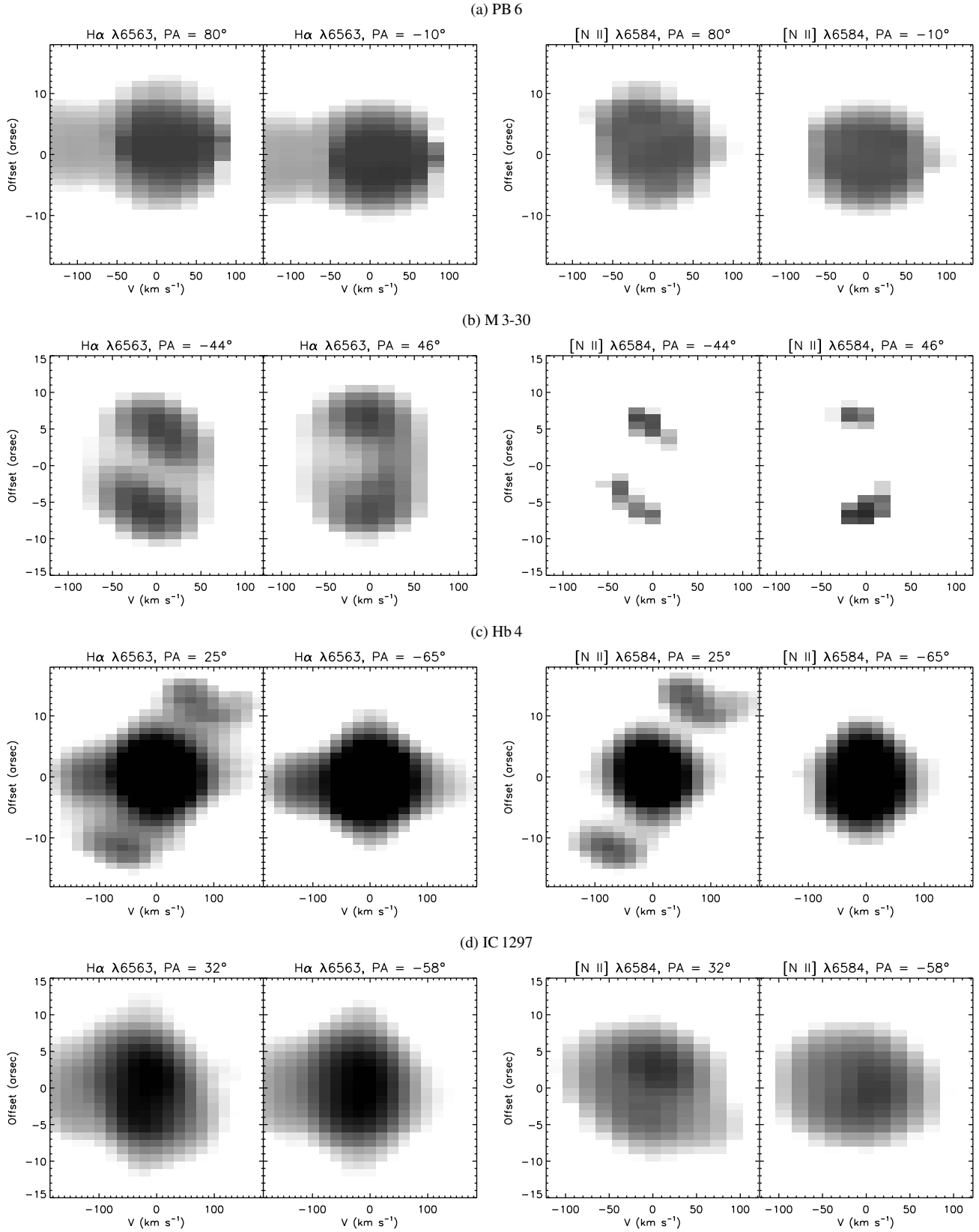


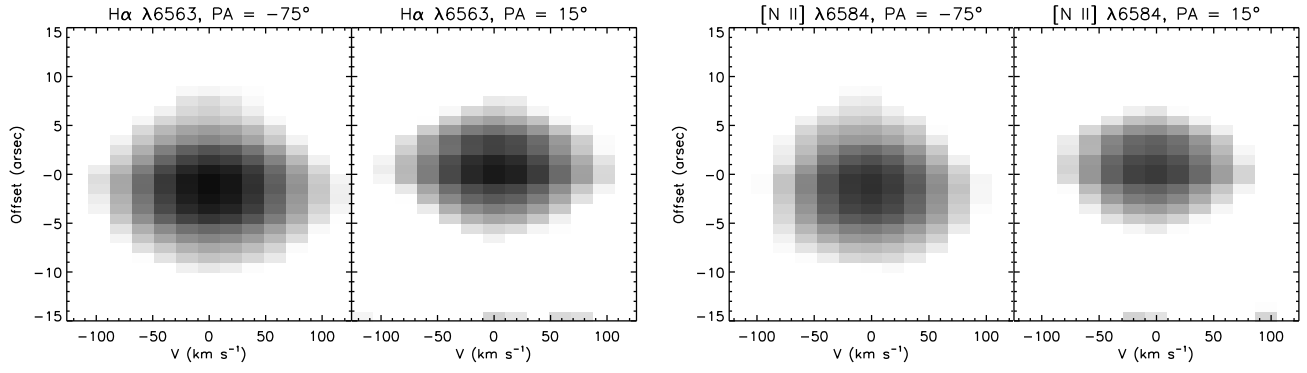
Figure 2. – continued

Morpho-kinematic properties of WR planetary nebulae

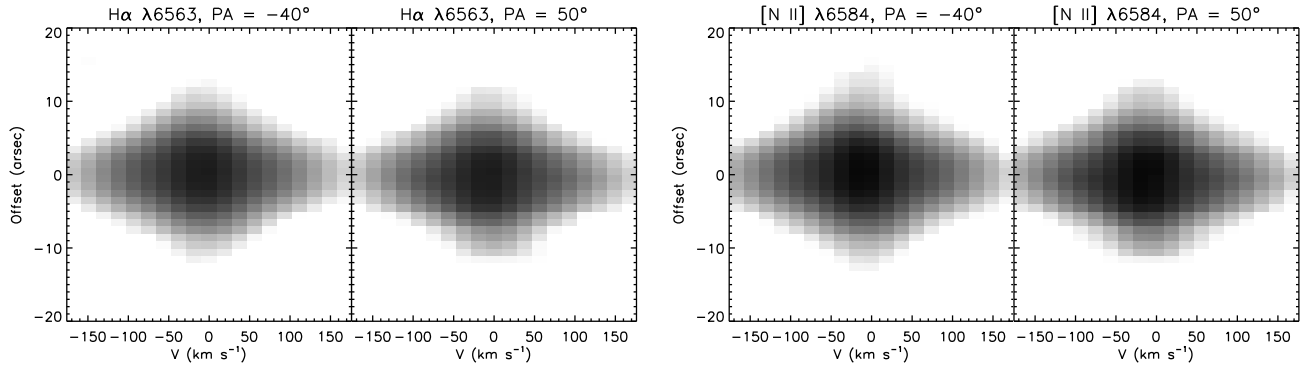


**Figure 3.** P–V arrays in the H $\alpha$   $\lambda$ 6563 and [N II]  $\lambda$ 6584 emissions for: (a) PB 6, (b) M 3-30, (c) Hb 4, (d) IC 1297, (e) Pe 1-1, (f) M 1-32, (g) M 3-15, (h) M 1-25, (i) Hen 2-142, (j) K 2-16, (k) NGC 6578, (l) NGC 6567, (m) NGC 6629, and (n) Sa 3-107. Slits oriented with the position angles (PA) along and vertical to the symmetric axis through the central star, respectively. The velocity is with respect to the systemic velocity of the object, given in km s<sup>-1</sup> unit. The angular offset at 0 arcsec is the nebular center.

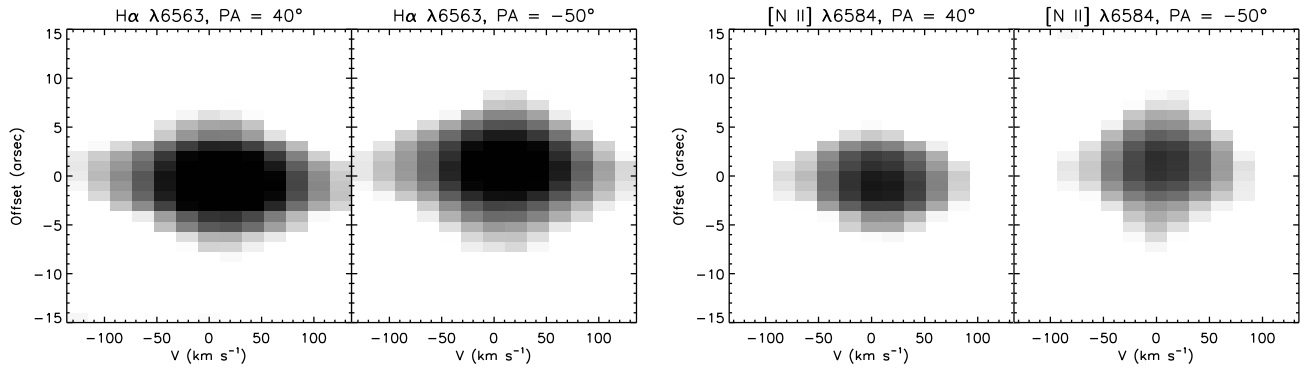
(e) Pe 1-1



(f) M 1-32



(g) M 3-15



(h) M 1-25

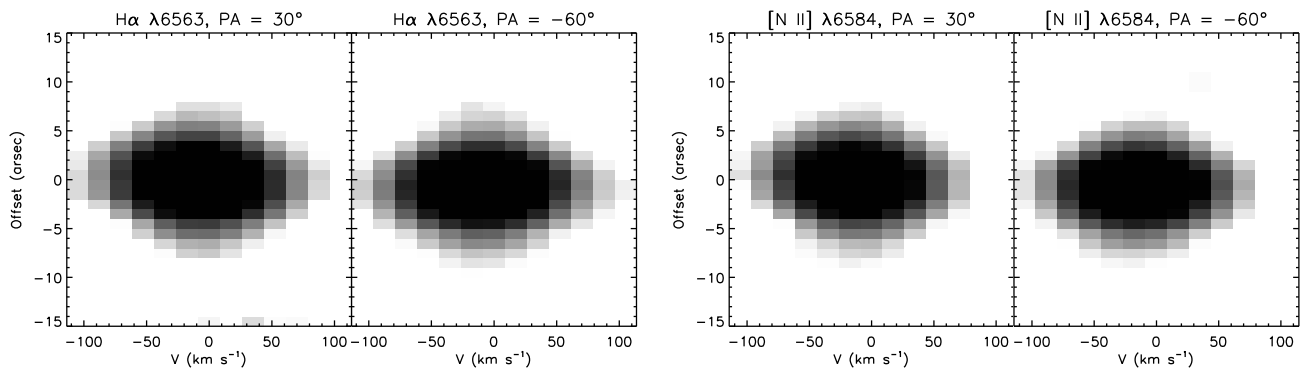
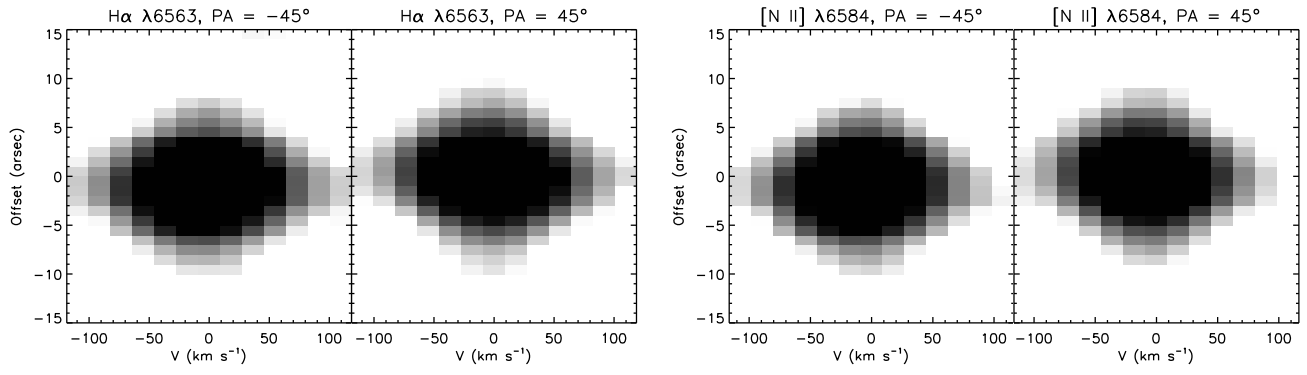


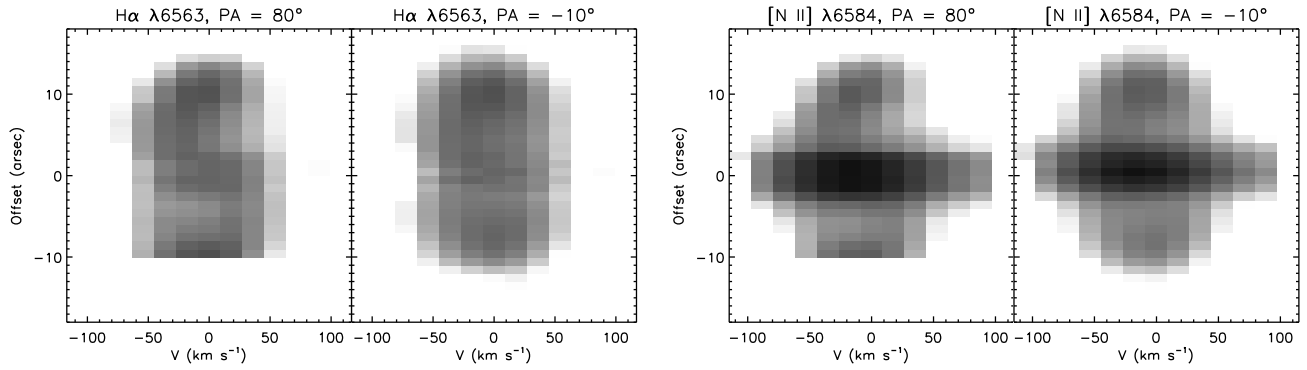
Figure 3. – continued

Morpho-kinematic properties of WR planetary nebulae

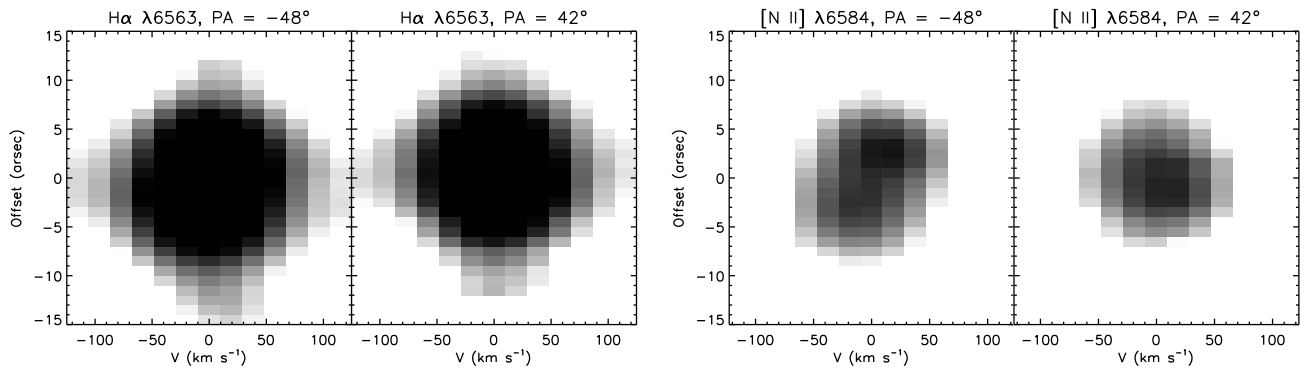
(i) Hen 2-142



(j) K 2-16



(k) NGC 6578



(l) NGC 6567

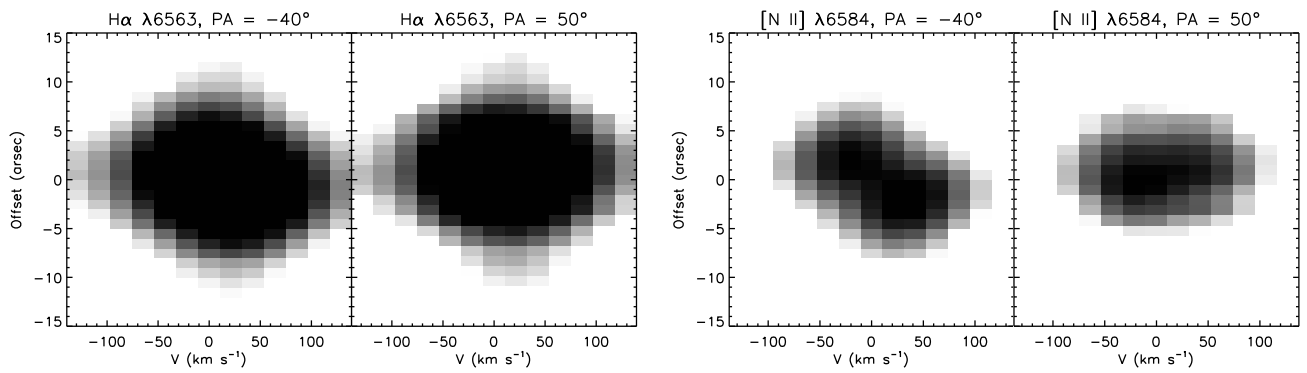
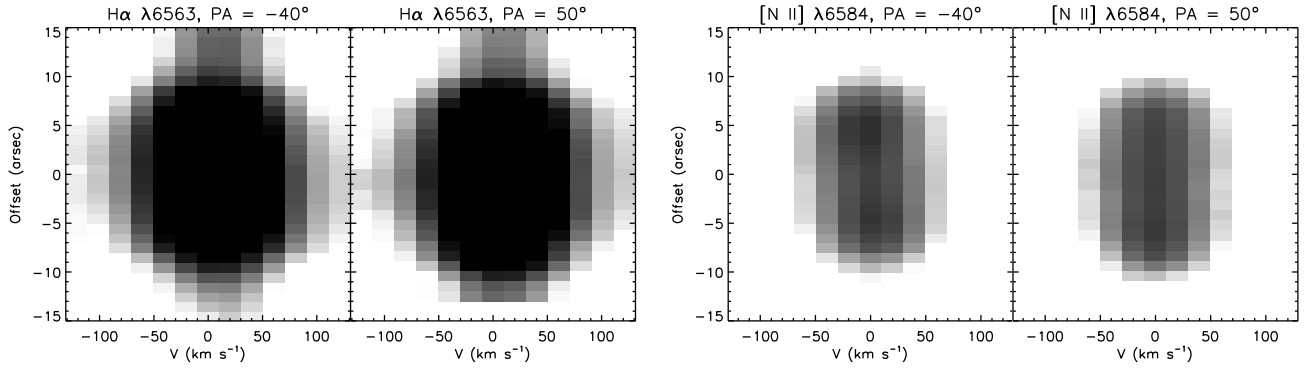


Figure 3. – continued

(m) NGC 6629



(n) Sa3-107

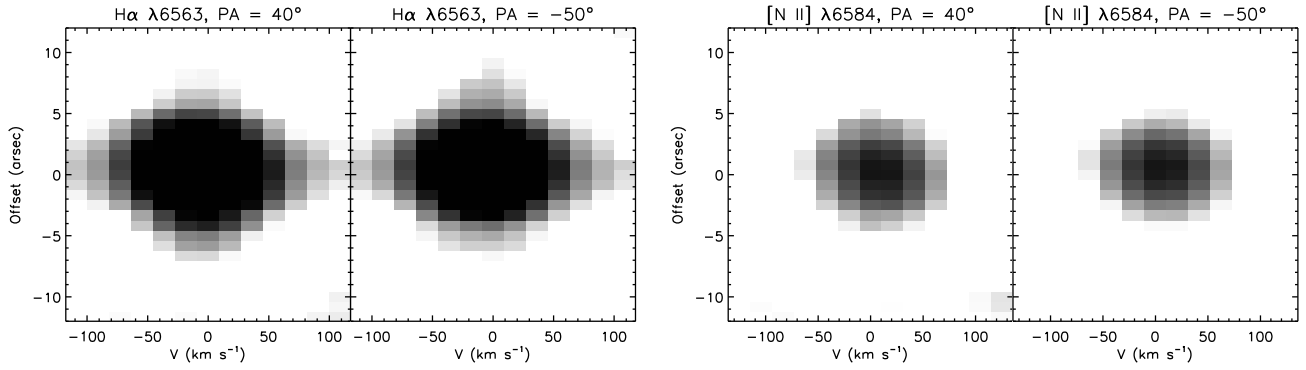
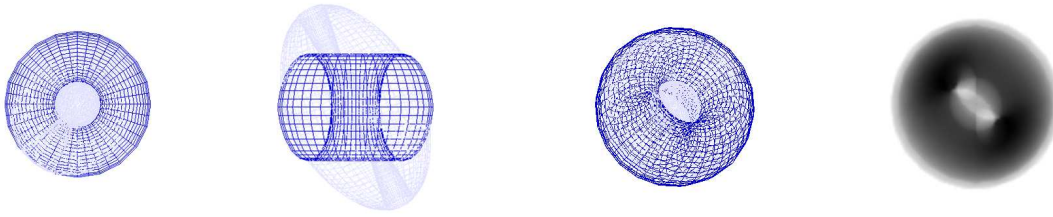
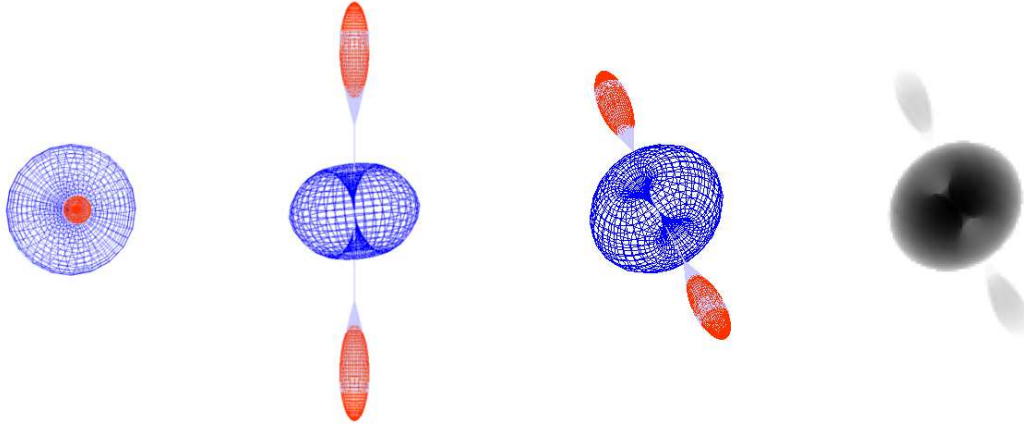


Figure 3. – continued

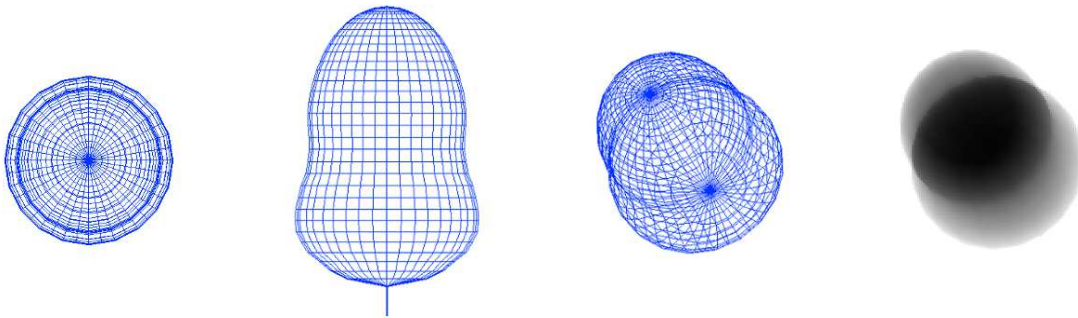
(a) M 3-30



(b) Hb 4



(c) IC 1297



(d) Pe 1-1

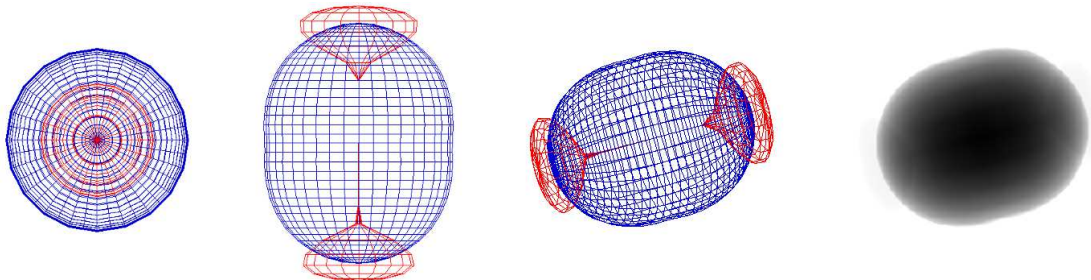
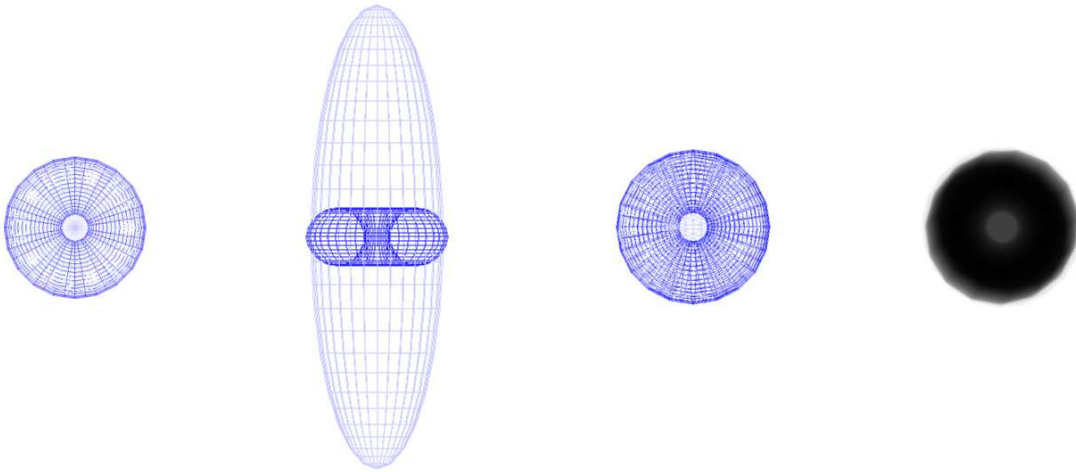
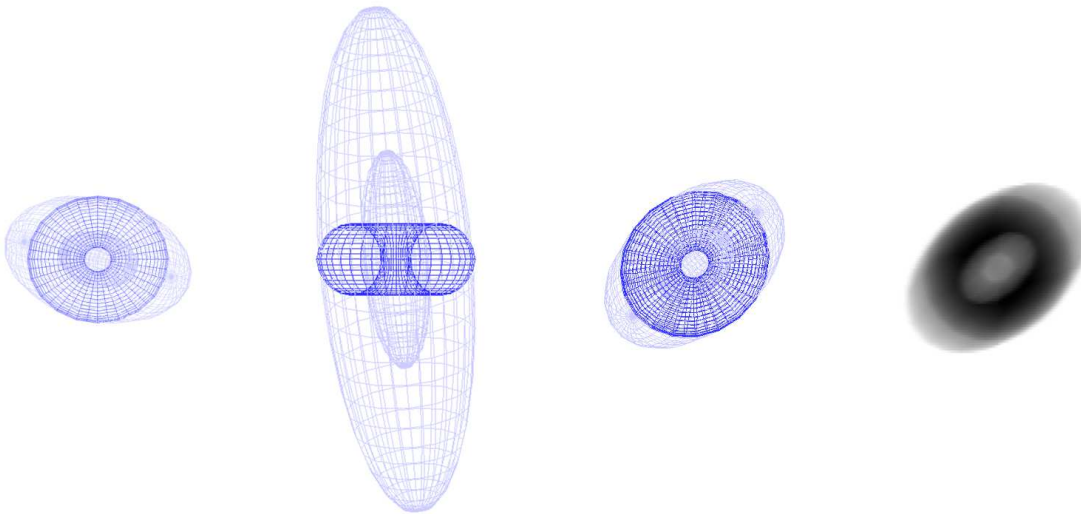


**Figure 4.** SHAPE mesh models for: (a) M 3-30, (b) Hb 4, (c) IC 1297, (d) Pe 1-1, (e) M 1-32, (f) M 3-15, (g) M 1-25, (h) Hen 2-142, (i) K 2-16, (j) NGC 6578, (k) NGC 6567, and (l) NGC 6629, before rendering at two different inclination angles ( $i = 0^\circ$  and  $90^\circ$ ), the best-fitting inclination and orientation, and the rendered image, respectively. The best-fitting parameters are listed in Table 3.

Danehkar  
(e) M 1-32



(f) M3-15



(g) M 1-25

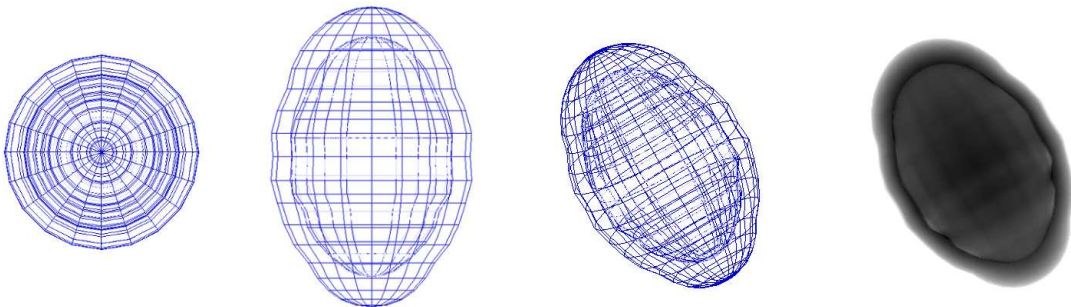
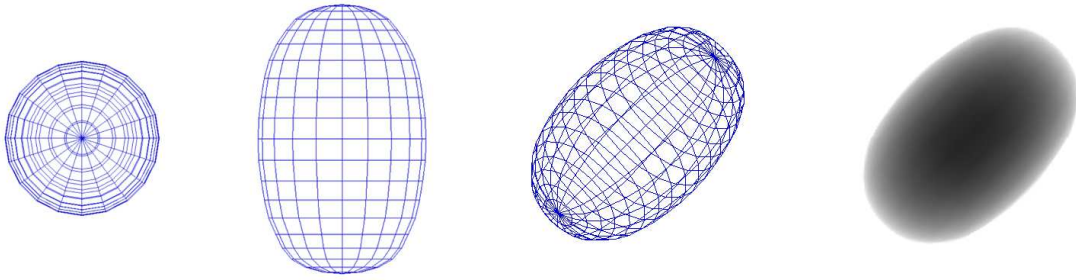
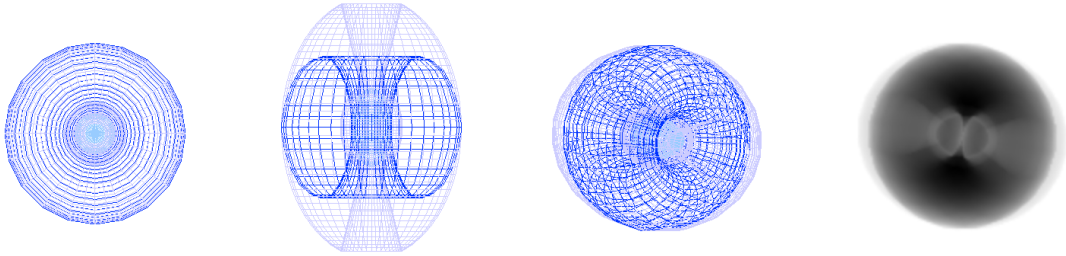


**Figure 4.** – *continued*

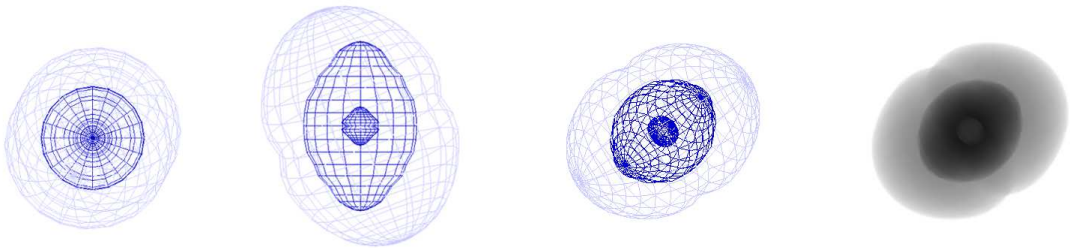
(h) Hen 2-142



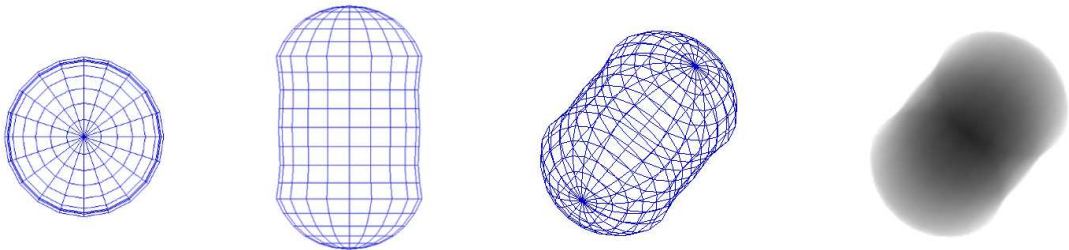
(i) K 2-16



(j) NGC 6578



(k) NGC 6567



(l) NGC 6629

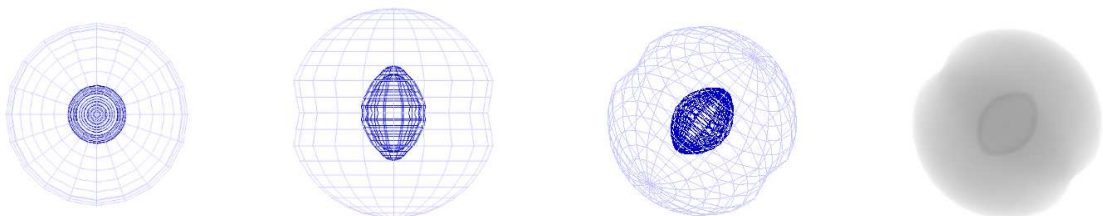
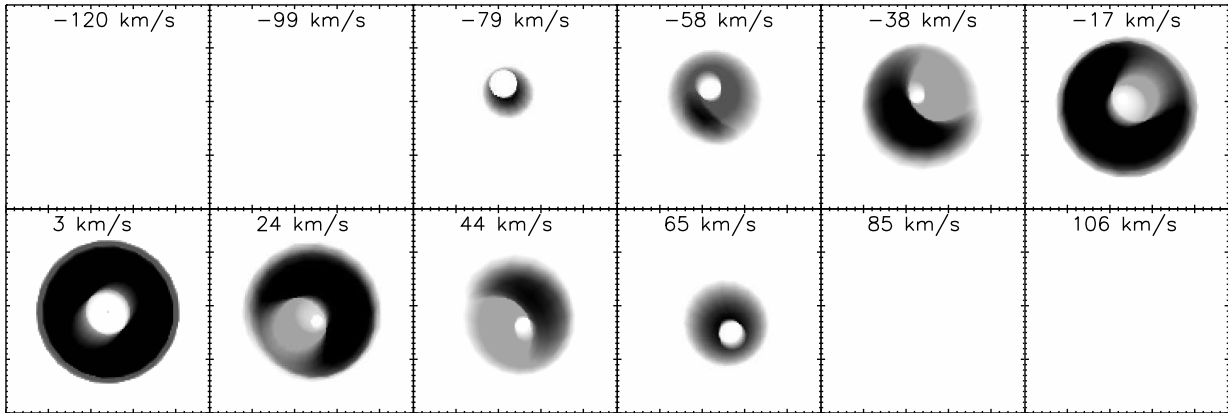
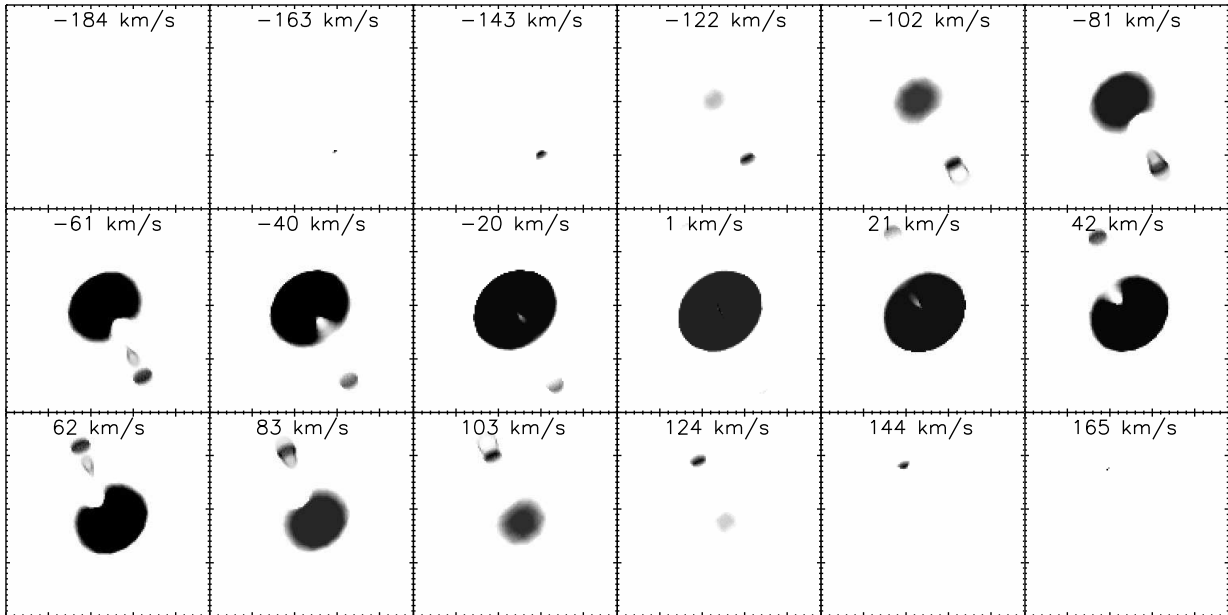


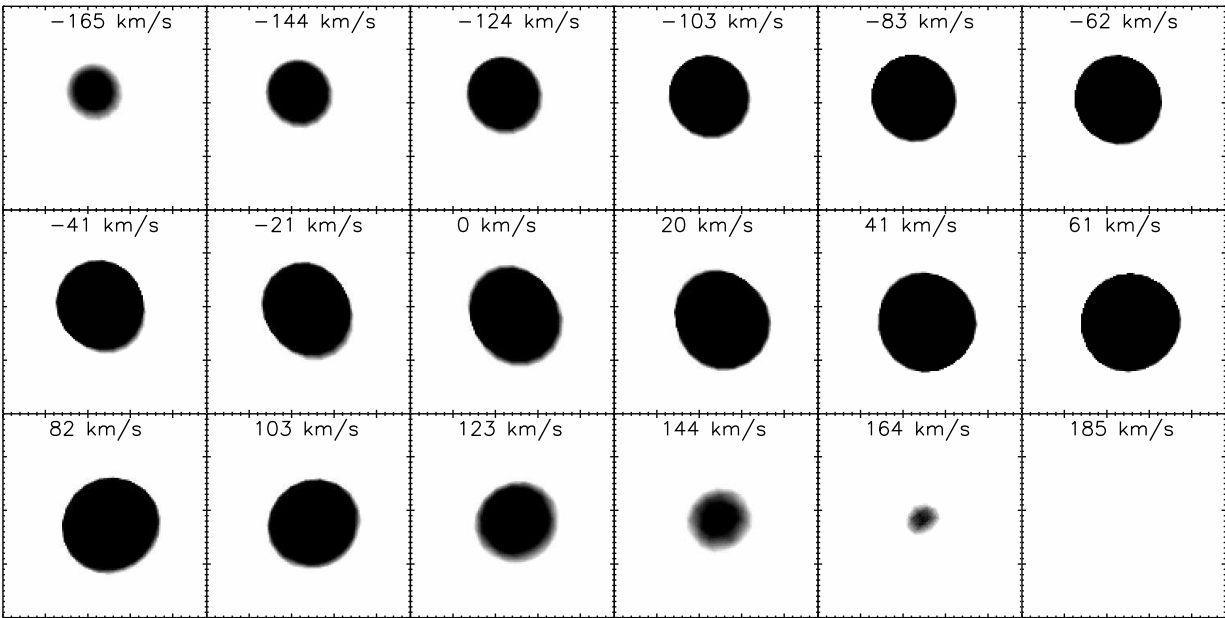
Figure 4. – continued

(a) M3-30 ( $H\alpha$   $\lambda 6563$ )(b) Hb4 ([N II]  $\lambda 6584$ )

**Figure 5.** Synthetic velocity-resolved channel maps for: (a) M 3-30, (b) Hb 4, (c) IC 1297, (d) Pe 1-1, (e) M 1-32, (f) M 3-15, (g) M 1-25, (h) Hen 2-142, (i) K 2-16, (j) NGC 6578, (k) NGC 6567, and (l) NGC 6629, produced by the best-fitting morpho-kinematic models for velocity slices along the  $H\alpha$   $\lambda 6563$  or  $[N II]$   $\lambda 6584$  emission (listed in round brackets following the PN name), with the parameters given in Table 3.

Morpho-kinematic properties of WR planetary nebulae

(c) IC 1297 ( $H\alpha$   $\lambda$ 6563)



(d) Pe 1-1 ( $H\alpha$   $\lambda$ 6563)

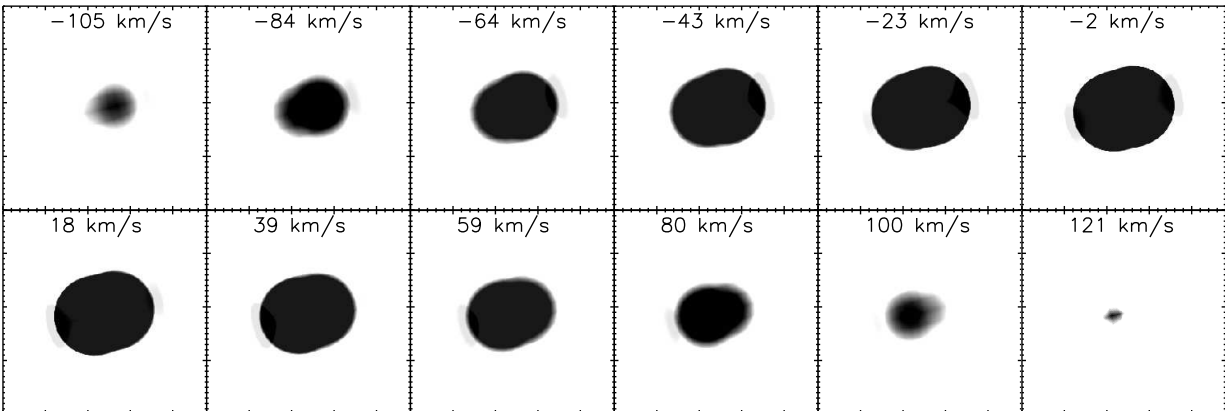
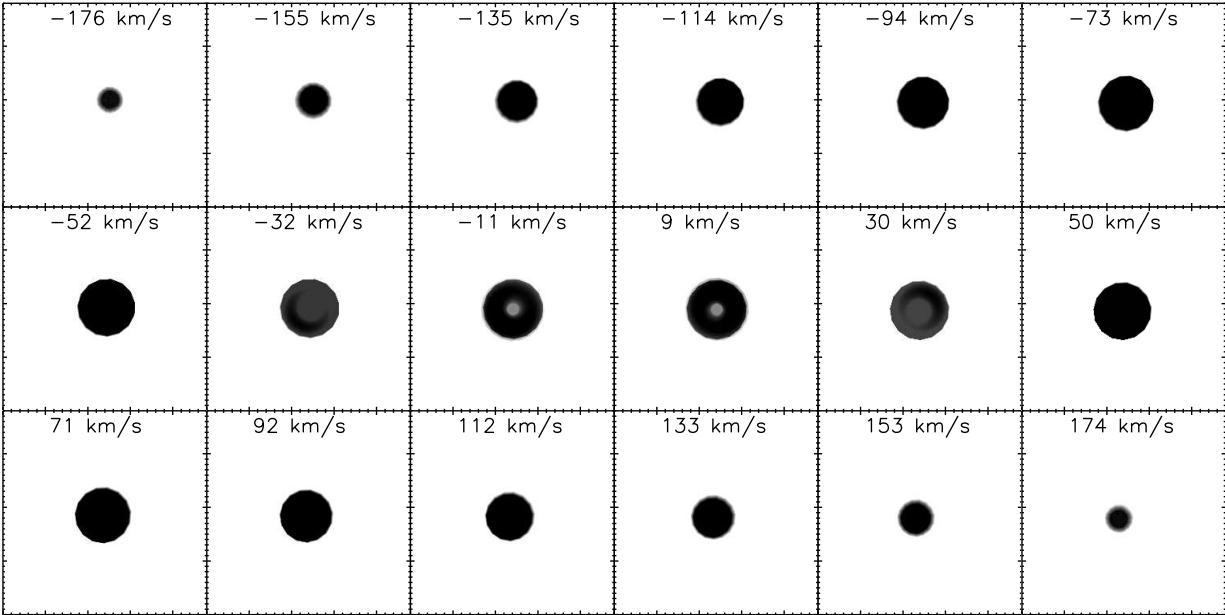


Figure 5. – continued

(e) M 1-32 ( $H\alpha$   $\lambda 6563$ )



(f) M 3-15 ( $H\alpha$   $\lambda 6563$ )

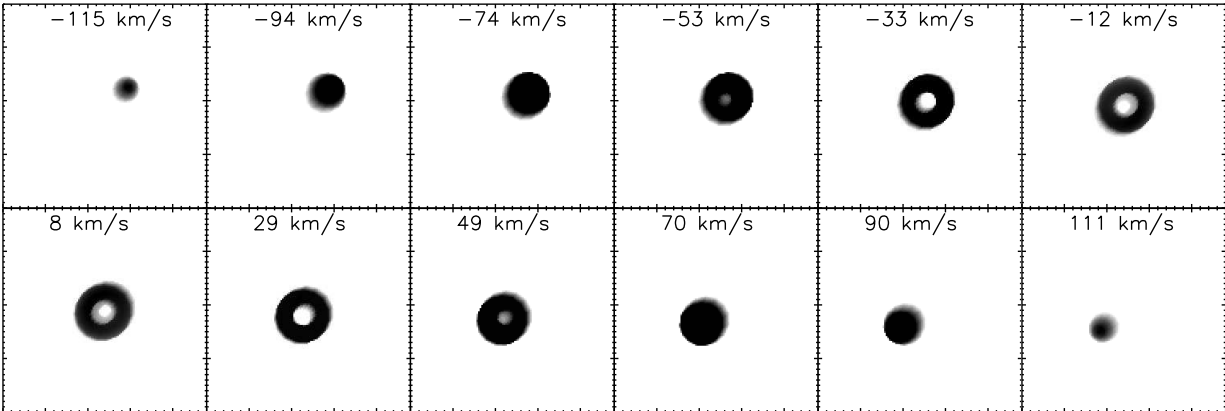
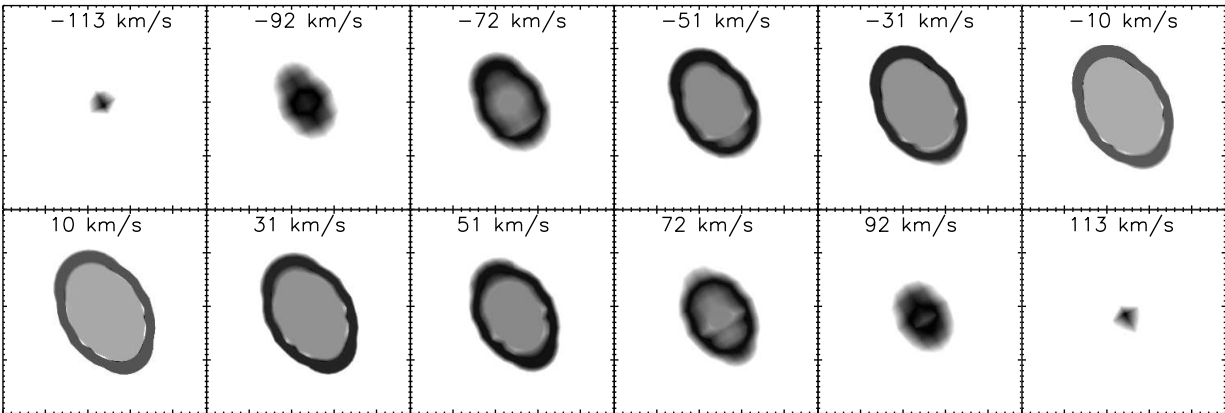


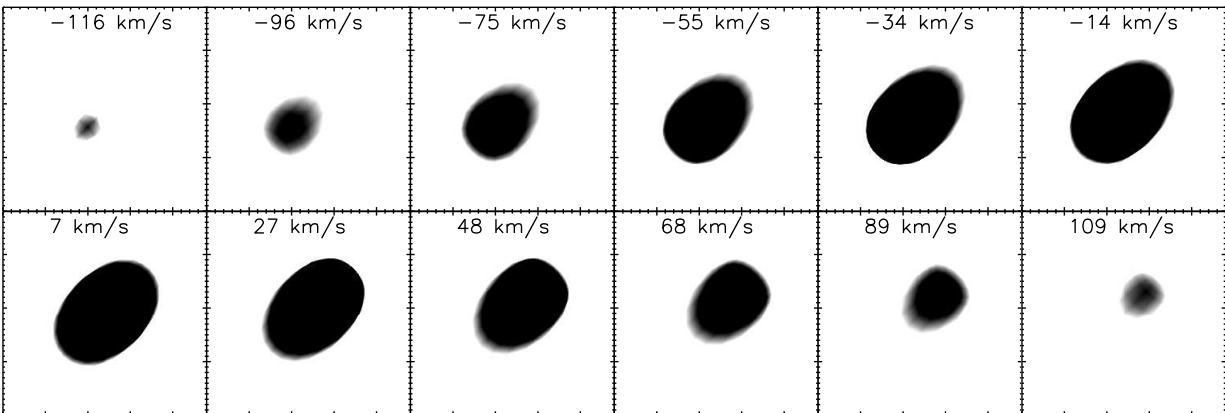
Figure 5. - continued

Morpho-kinematic properties of WR planetary nebulae

(g) M 1-25 ( $H\alpha$   $\lambda$ 6563)



(h) Hen 2-142 ( $[N II]$   $\lambda$ 6584)



(i) K 2-16 ( $H\alpha$   $\lambda$ 6563)

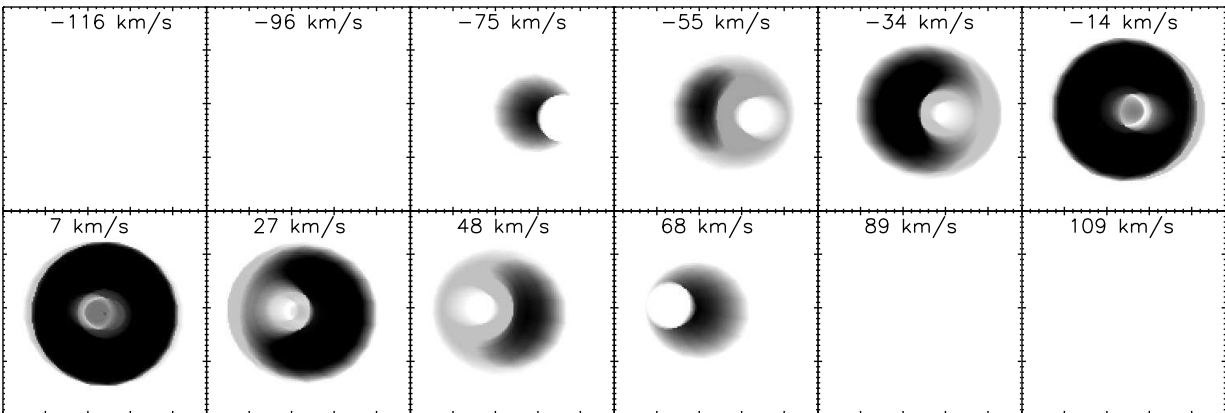
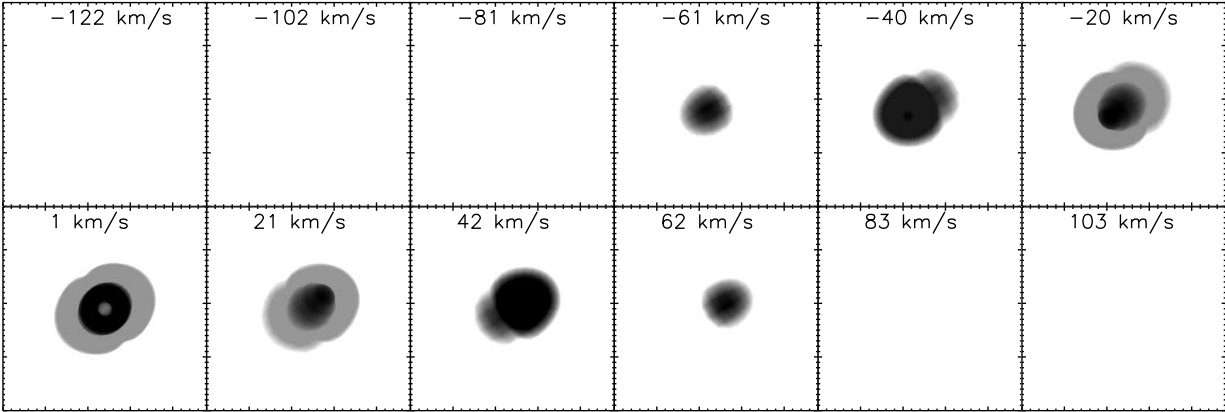


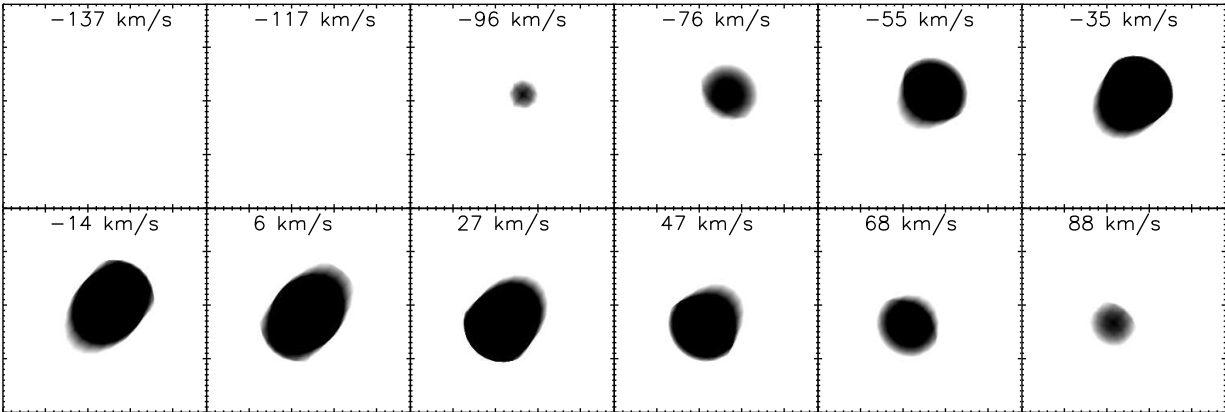
Figure 5. – continued

Danehkar

(j) NGC 6578 ([N II]  $\lambda$ 6584)



(k) NGC 6567 ([N II]  $\lambda$ 6584)



(l) NGC 6629 ([N II]  $\lambda$ 6584)

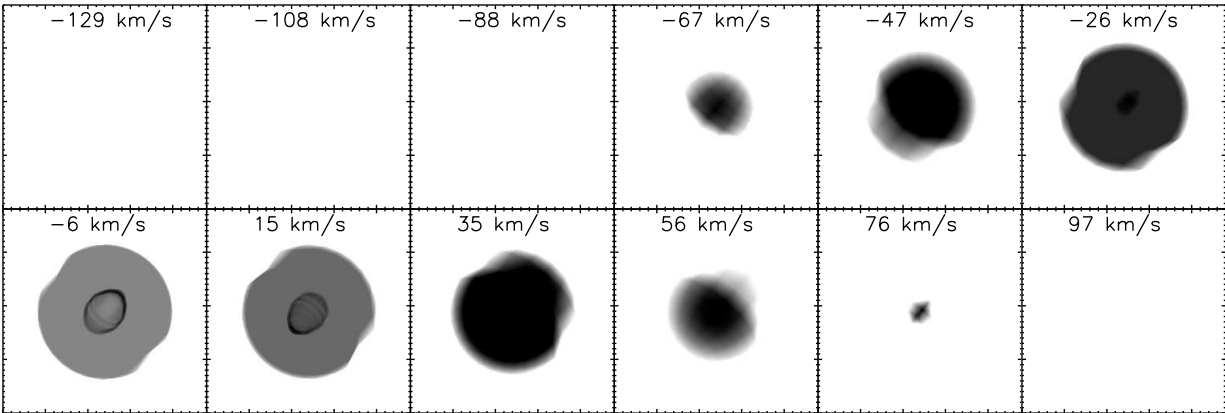
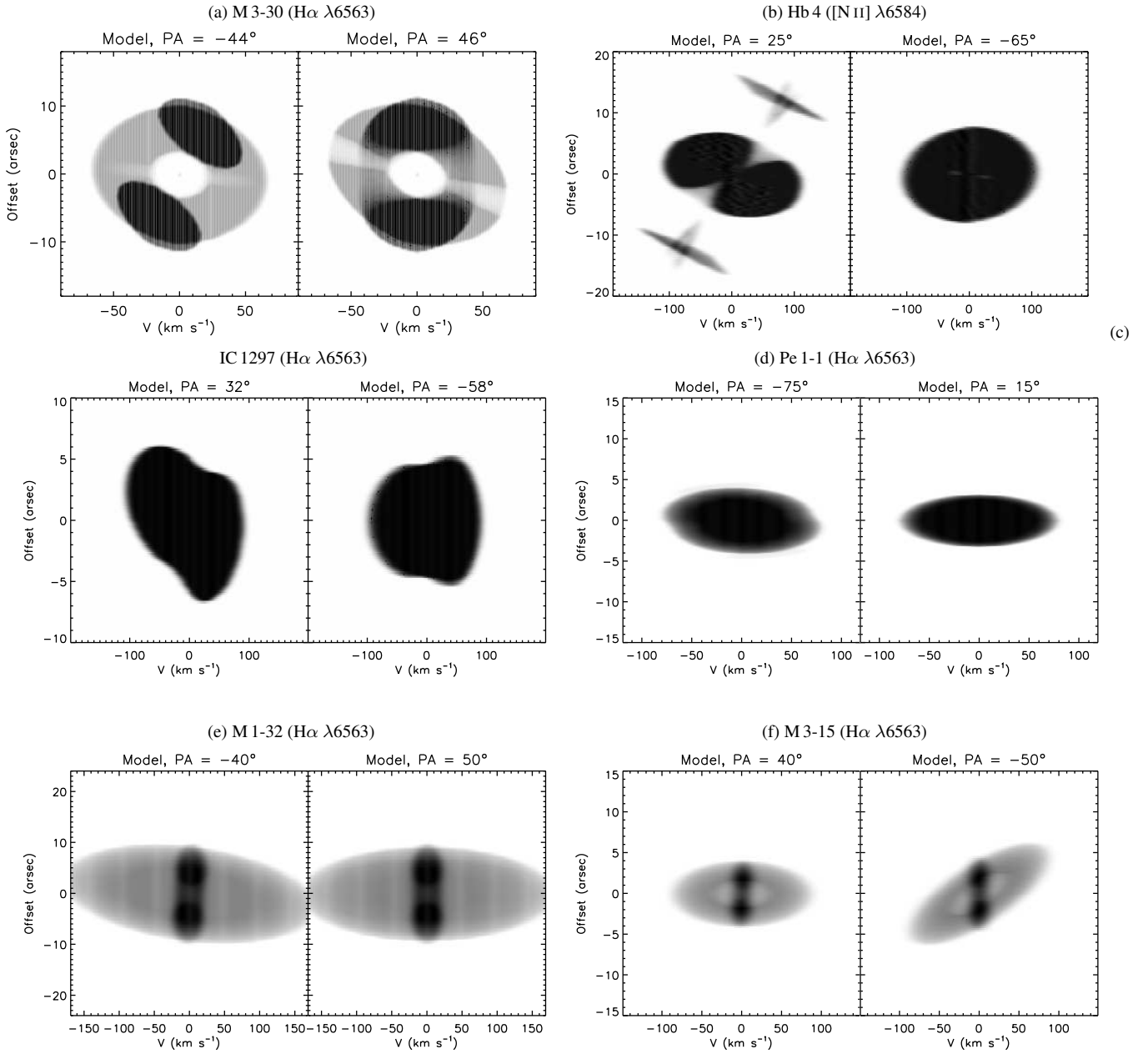


Figure 5. – continued

Morpho-kinematic properties of WR planetary nebulae



**Figure 6.** Synthetic P-V diagrams for (a) M3-30, (b) Hb4, (c) IC 1297, (d) Pe 1-1, (e) M1-32, (f) M3-15, (g) M1-25, (h) Hen 2-142, (i) K 2-16, (j) NGC 6578, (k) NGC 6567, and (l) NGC 6629, produced by slits oriented with the position angles (PA) along and vertical to the symmetric axis through the nebular center for the best-fitting morpho-kinematic models reproducing the P-V arrays in the  $H\alpha$   $\lambda 6563$  or  $[N II] \lambda 6584$  emission (listed in round brackets following the PN name), with the parameters given in Table 3.

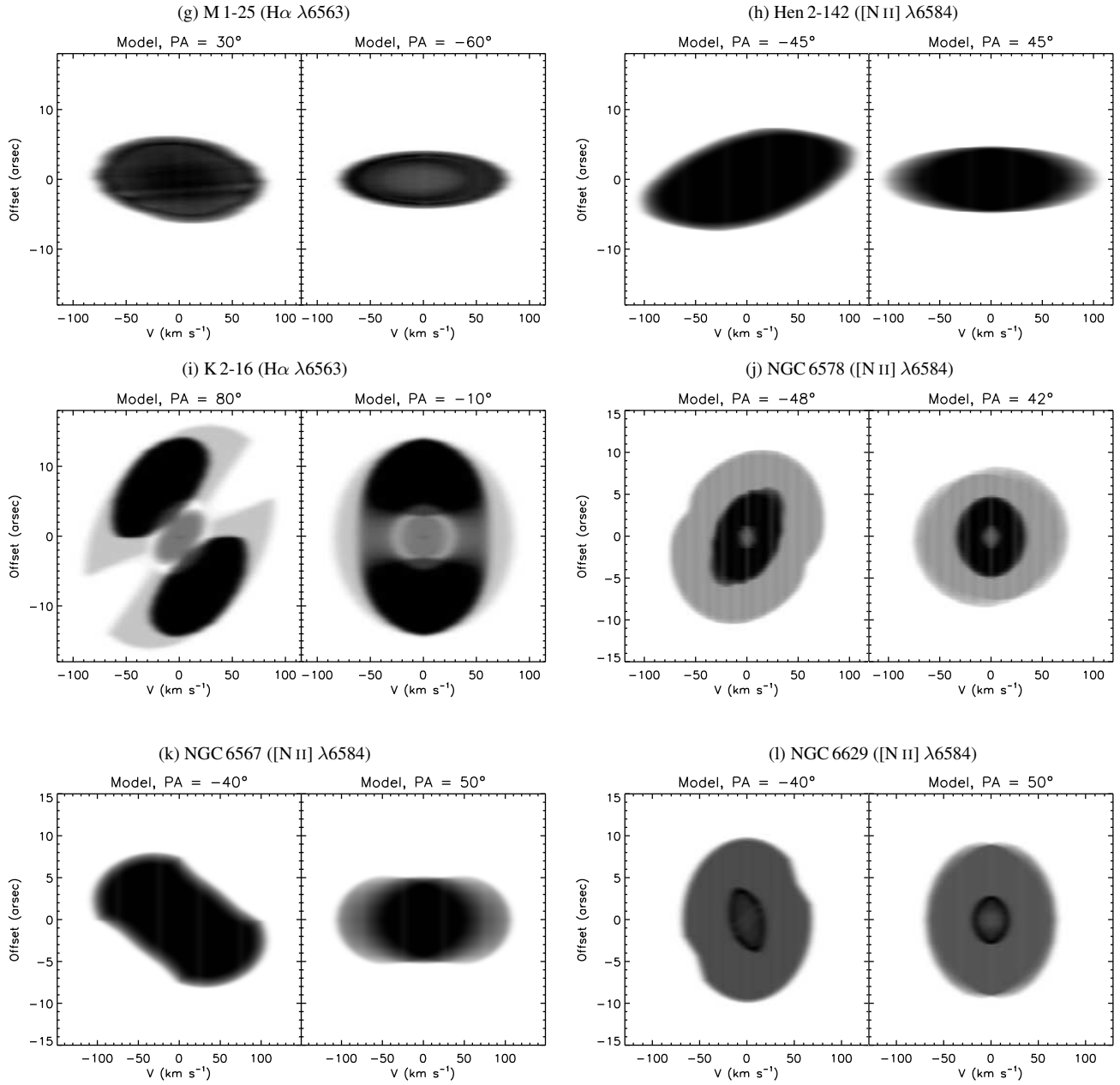


Figure 6. – continued